



Universidad de Concepción
Dirección de Postgrado
Facultad de Ciencias Químicas
Programa Doctorado en Ciencias Geológicas

**Rebote elástico de la corteza superior debido a deflexión durante
desglaciación: un mecanismo de primer orden en la descompresión y
activación de sistemas volcánicos superficiales**

(**Elastic rebound of the upper crust due flexural unbending during
deglaciation: a first order mechanism in decompression and activation of
shallow volcanics systems**)

Tesis para optar al grado de Doctor en Ciencias Geológicas

DAVID RODRIGO MORA COFRÉ
CONCEPCIÓN-CHILE
2019

Profesor Guía: Andrés Tassara Oddo
Dpto. de Ciencias de la Tierra
Facultad de Ciencias Químicas
Universidad de Concepción

A mi familia ...



Agradecimientos

Agradezco a mi familia por el apoyo moral y económico proporcionado.

Agradezco a los profesores del programa de Doctorado en Ciencias Geológicas de la Universidad de Concepción, quienes han contribuido en distintas etapas de mi formación científica.

Agradezco al Dr. Andrés Tassara, quien ha guiado la presente tesis con importantes aportes.

Agradezco el financiamiento parcial aportado por los proyectos Fondecyt 1151175 “Active Tectonics and Volcanism at the Southern Andes” (ACT&VO) y Núcleo Milenio NC160025 “Seismic Cycle at Subduction Zones” (CYCLO), en cuyos marco de investigación se incerta la presente tesis. Agradezco a la Dirección de Postgrado de la Universidad de Concepción por el apoyo económico proporcionado a través de becas de estipendio y arancel.



RESUMEN

La descompresión inducida por grandes desglaciaciones sobre sistemas volcánicos son comúnmente estudiadas utilizando modelos de cargas superficiales sobre la corteza terrestre, representándola como un semi-espacio elástico o capa con espesor infinito. Investigamos el rebote post-glacial debido a la deflexión de una placa elástica de espesor finito como un mecanismo de primer orden en la descompresión y fracturamiento de reservorios magmáticos superficiales durante la desglaciación. Implementamos dos modelos analíticos para investigar la magnitud de la descompresión de la corteza causada por la desglaciación en reservorios magmáticos de la corteza superior: el primero está basado en la deflexión eje-simétrica de un disco delgado simplemente soportado, mientras que el segundo considera una placa elástica delgada de longitud infinita con recuperación hidrostática de la corteza media-inferior o manto astenosférico. Considerando un modelo numérico climático publicado, describiendo la evolución espacial-temporal de la desglaciación después del Último Máximo Glacial (UMG) a través de la Zona Volcánica Sur (ZVS) de los Andes, demostramos que los cambios en presión en niveles de la corteza superior (< 10 km en profundidad) en la escala de varios cientos de años son del orden de 10 a >100 MPa. La descompresión total y las tasas de descompresión son entonces 1-3 órdenes de magnitud mayor que los valores estimados por autores anteriores, quienes asumen que las cargas glaciares están soportadas por un semi-espacio elástico. La gran descompresión causada por la deflexión de las placas elásticas de espesor finito estimadas por nosotros puede fácilmente sobrepasar la resistencia a la tensión de las rocas, creando condiciones adecuadas para la ruptura de las paredes de los reservorios, propagación de diques hacia adentro y fuera del reservorio y el colapso eventual del reservorio acompañado por una erupción explosiva. Aplicamos nuestros resultados al análisis de erupciones post-glaciales de volcanes en la ZVS, los cuales erupcionaron grandes volúmenes ($> 10 \text{ km}^3$) de ignimbritas y tobas maficas, cientos a mil años después del inicio de la desglaciación. Mostramos que este tiempo de retardo es necesario para alcanzar una descompresión de decenas de mega-pascales a profundidades de algunos kilómetros, consistente con la ubicación de reservorios magmáticos estimada por estudios petrográficos, sísmicos y/o geodésicos independientes. Además, el incremento hacia el norte del tiempo de retardo está en acuerdo con el menor tamaño de la capa de hielo Andina en el norte respecto a la del sur durante el UMG. El mecanismo propuesto podría promover grandes erupciones explosivas de magmas rico en volátiles en zonas de subducción, tanto para desglaciaciones pasadas y para el actual retiro de los hielos causado por el cambio climático sobre arcos relacionados a subducción en áreas de elevada latitud.

ABSTRACT

Decompression induced by large deglaciations on volcanic systems are commonly studied using models of surface loads on the Earth's crust, representing its like an elastic half-space or layer with infinite elastic thickness. We investigated the postglacial rebound due to flexural unbending of an elastic plate of finite thickness as a first-order mechanism in the decompression and fracturing of shallow magmatic reservoirs during deglaciation. We implement two analytical models to investigate the magnitude of crustal decompression caused by deglaciation at upper crustal magmatic reservoirs: the first one is based on axisymmetric deflection of simply supported thin elastic disc, whereas the second one considers an infinite-length thin elastic plate with hydrostatic recovering of the middle-lower crust or mantle. Considering a published numerical climate model, describing the space-time evolution of deglaciation after the Last Glacial Maximum (LGM) along the Southern Volcanic Zone (SVZ) of the Andes, we demonstrate that changes in pressure at upper crustal levels (< 10 km depth) at the scale of several hundred years are of the order of 10 to >100 MPa. Total decompression and decompression rate are therefore 1-3 orders of magnitude larger than values estimated by previous authors, who assumed glacial loads are supported by an elastic half space. The large decompression caused by flexural unbending of an elastic plate of finite thickness estimated by us can easily surpass the tensile strength of rocks, creating adequate conditions for failure of the reservoir walls, dike propagation inside and outside the reservoir and the eventual collapse of the reservoir accompanying an explosive eruption. We apply our results to the analysis of postglacial eruptions of SVZ volcanoes, which erupted large volume (>10 km 3) mafic ignimbrites and tobes, hundreds to one thousand years after deglaciation onset. We show that this time lag is necessary to achieve a decompression of several tens of megapascals at depths of some kilometers, consistent with the location of magmatic reservoirs as estimated by independent petrologic, seismic and/or geodetic studies. Moreover, the northward increase of this time lag is in agreement with a smaller size of the Andean ice cap in the north than in the south during the LGM. The proposed mechanism could promote large explosive eruptions of volatile-rich magmas in subduction zones, both for past deglaciations and for current accelerated ice retreat caused by climate change over subduction-related arcs in high latitudes.

Índice de contenidos

RESUMEN.....	4
ABSTRACT.....	5
CAPÍTULO I: INTRODUCCIÓN GENERAL	10
1.1 Planteamiento del problema	10
1.2 Hipótesis	11
1.3 Objetivos	12
1.3.1 Objetivo general.....	12
1.3.2 Objetivos específicos	12
1.4 Metodología	12
1.4.1 Último máximo glacial en los Andes del sur.....	13
1.4.2 Relaciones entre evidencias empíricas y el modelo climático.....	13
1.4.3 Desglaciación	17
1.4.4 Erupciones explosivas postglaciares en la ZVS de los Andes.....	23
1.4.5 Modelos de flexura de placas delgadas.....	28
1.5 Conceptos básicos de esfuerzos, elasticidad y flexura de placas delgadas	28
1.5.1 Esfuerzos, Esfuerzos normales, Presión y deformación	28
1.5.2 Elasticidad lineal	28
1.5.3 Estado de esfuerzo plano o biaxial	30
1.5.4 Flexura de placas delgadas: Comportamiento General	31
CAPÍTULO II: UPPER CRUSTAL DECOMPRESSION DUE TO DEGLACIATION-INDUCED FLEXURAL UNBENDING AND ITS ROLE ON POSTGLACIAL VOLCANISM AT THE SOUTHERN ANDES.....	34
2.1 Abstract.....	35
2.2 Introduction.....	35
2.3 Analytical approximation and method.....	40
2.3.1 Derivation of the equation for flexural deflection of a thin elastic disk loaded at its surface.....	40
2.3.2 Limitations of the model.....	42

2.3.3 Comparison against the elastic half-space model	42
2.3.4 Incorporating the temporal evolution of deglaciation for the Southern Andes	43
2.4 Application to the Southern Andes	45
2.5 Discussion.....	49
2.5.1 Implications of finite versus infinite thickness of the elastic media on deglaciation-induced decompression	49
2.5.2 The case of the Southern Andes for understanding the role of postglacial flexural unbending.....	49
2.5.3 Postglacial mafic ignimbrites and the role of upper crustal decompression.....	51
2.6 Concluding remarks.....	52
CAPÍTULO III: COMBINING FLEXURAL UNBENDING AND ISOSTATIC ADJUSTMENT TO UNDERSTAND POSTGLACIAL DECOMPRESSION OF UPPER CRUSTAL RESERVOIRS AT THE SOUTHERN ANDES.....	54
3.1 Abstract.....	55
3.2 Introduction.....	55
3.3 Analytical approximation and method.....	57
3.3.1 Derivation of the equation for flexural deflection of a two-dimensional thin-elastic plate of infinite-length loaded on its surface.....	57
3.3.2 Limitations of the model.....	59
3.4 Result	60
3.4.1 The Young's modulus (E) as a function of the density contrast ($\Delta\rho$)	60
3.4.2 Model sensitivity to Young's modulus (E) and the density contrasts ($\Delta\rho$)	61
3.4.3 Decrease in pressure (P) and model restrictions.....	63
3.4.4 Increase in pressure change (ΔP) during deglaciation in the Southern Andes.....	64
3.4.5 Depth of decompression $Z\Delta P$ as a function of the deglaciation factor Q (t) in the Southern Andes.....	65
3.5 Discussion.....	68
3.5.1 Rheological implications.....	69
3.5.2 Implications in the estimation of the depth of shallow magmatic chambers	69
3.6 Conclusions	70
CAPÍTULO IV: SÍNTESIS Y DISCUSIÓN	71

CAPÍTULO V: CONCLUSIONES.....	74
ANEXOS	76
ANEXO 1: Derivation of the equation for flexure of a cylindrical thin elastic plate under uniform load (Appendix A)	76
ANEXO 2: Flexure and flexural stresses developed in thin elastic-plate of infinite-length on a Winkler foundation and with uniform load on its surface (Appendix B)	80
REFERENCIAS.....	83

Índice de Figuras

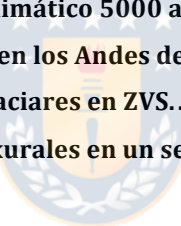
Figura 1.1: Representación del modelo climático y evidencias empíricas del UMG en los Andes del Sur.	15
Figura 1.2: Representación del modelo climático 300 años siguiendo la desglaciación y evidencias empíricas del primer calentamiento en los Andes del Sur.	18
Figura 1.3: Representación del modelo climático 5000 años siguiendo la desglaciación y evidencias empíricas del tercer calentamiento en los Andes del Sur.	22
Figura 1.4: Erupciones explosivas postglaciares en ZVS.	24
Figura 1.5: Distribución de esfuerzos flexurales en un segmento de placa.	32
	
Figure 2.1: Extent of ice cover during the Last Glacial Maximum (LGM) and distribution of Quaternary volcanoes at global scale (A) and for the Southern Andes (B).	37
Figure 2.2: Basics of the physical model for flexure of a thin elastic disk loaded by the weight of an ice sheet.	41
Figure 2.3: Evolution of Deglaciation Factor Q(t).	44
Figure 2.4: Depth profile of pressure P (left) and pressure change ΔP (right).	45
Figure 2.5: Depth $Z_{\Delta P}$ at which a certain decompression ΔP occur as a function of the deglaciation factor $Q(t)$ (or time in thousand of years after deglaciation onset) for a range of ΔP, elastic thickness d and Poisson's ratio ν.	47
Figure 2.6: Depth $Z_{\Delta P}$ at which a certain decompression ΔP occur as a function of the deglaciation factor $Q(t)=V(t)/V_0$, as is Fig. 2.5 but analyzing the effect of changing geometry of glacier cap thickness and radio at deglaciation onset h_0 and R_0.	48

Figure 3.1: Basics of the physical model for flexure of a thin elastic-plate of infinite-length on a Winkler foundation and loaded by the weight of an ice sheet.....	59
Figure 3.2: Dependence of the Young's modulus (E) as a function of the density contrast ($\Delta\rho$) of thin elastic-plate of infinite-length considering a constant pressure at a certain depth.	61
Figure 3.3: Comparisons of pressures (A, B and C) calculated with the models of thin-elastic disc simply supported (orange line; Mora & Tassara, 2019) and a thin elastic-plate of infinite-length (blue lines).....	62
Figure 3.4: Decrease in pressure during deglaciation in the Southern Andes.....	64
Figure 3.5: Increase in pressure change during deglaciation in the Southern Andes.....	65
Figure 3.6: Depth of decompression as a function of the deglaciation factor in the Southern Andes. (A: E= 2×10^{10} Pa; B: E= 7×10^{10} Pa).....	66
Figure 3.7: Glacier with smaller R_0 and h_0 (respect figure 3.6B).....	67
Figure 3.8: Effect of a higher density contrast (respect figure 3.6B)	68
Figure 3.9: Effect of a greater elastic thickness (respect Figure 3.6B).	68

Índice de Tablas

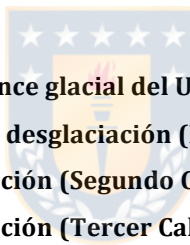
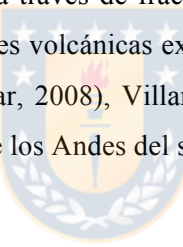


Tabla 1.1: Dataciones ^{14}C del último avance glacial del UMG.	16
Tabla 1.2: Dataciones ^{14}C del inicio de la desglaciación (Primer Calentamiento).....	19
Tabla 1.3: Dataciones ^{14}C de la desglaciación (Segundo Calentamiento).....	20
Tabla 1.4: Dataciones ^{14}C de la desglaciación (Tercer Calentamiento).....	21

Table 3.1: Range of validity parameters of the thin elastic plate model of infinite length for glaciers with initial width 50, 100 and 150 km; satisfying the constraint of the model $dP/dQ(t) < 0$63

CAPÍTULO I: INTRODUCCIÓN GENERAL

La presente tesis contiene dos trabajos de investigación para explicar a través de modelos físicos el impacto de la desglaciación en la descompresión y activación de sistemas volcánicos superficiales. Los modelos implementados utilizan como principios básicos la elasticidad lineal de los materiales de la corteza superior, el estado de esfuerzo plano y el mecanismo de flexura de placas delgadas (Turcotte & Schubert, 2014; Watts, 2001). Ambos trabajos consideran que la corteza superior, previamente flexionada hacia abajo por el peso de los glaciares del UMG (ej., Denton et al., 1999) en los Andes del Sur, comienza a revertir su flexión (deflexión) por la liberación de carga sobre ella debido al adelgazamiento y retroceso de la capa de hielo glaciar durante la desglaciación (ej., McCulloch et al., 2000). Se propone que el proceso de deflexión de la corteza superior durante una desglaciación es un mecanismo de primer orden que ocasiona la descompresión y fracturamiento de los reservorios magmáticos superficiales localizados bajo las masas glaciares. Tal descompresión es suficiente para sobrepasar el límite de resistencia a la tensión de las rocas en las paredes de los reservorios (ej., Rubin, 1995) y permitir la inyección de diques a través de fracturas de tensión (ej., Pinel & Jaupart, 2003), promoviendo en muchos casos erupciones volcánicas explosivas como las ocurridas en tiempos post-glaciares en los volcanes Llaima (Lohmar, 2008), Villarrica (Lohmar, 2008; Lohmar et al., 2012) y Hudson (Weller et al., 2014) en la ZVS de los Andes del sur.

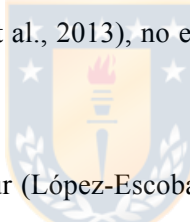


1.1 Planteamiento del problema

En áreas volcánicas activas, la modificación del estado de esfuerzos por procesos externos puede afectar la actividad volcánica e incluso iniciar una erupción (ej.: Cañón-Tapia, 2013; Manga & Brodsky, 2006). En los períodos de glaciación, las enormes cargas de hielo desarrollan una flexura en la corteza terrestre y fuerzan a las rocas del manto a fluir lateralmente (Turcotte & Schubert, 2014; Watts, 2001). Debido a los esfuerzos flexurales, se generan condiciones favorables para la acumulación de magma en la corteza superior en áreas volcánicas (ej., Rawson et al., 2016), junto con impedir la inyección de diques y retardar la ocurrencia de erupciones (Jellinek et al., 2004; Sigvaldason et al., 1992; Violette et al., 2001). La disminución de las cargas glaciares y esfuerzos flexurales durante una desglaciación, causan una deflexión (Walcott, 1970; Watts, 2001) de la corteza superior y liberación del magma atrapado en esta (ej., Rawson et al., 2016). Además, la descompresión por disminución de los esfuerzos flexurales es transmitida a las paredes de cámaras magmáticas poco profundas. Esta

alteración del campo de esfuerzos, proporciona condiciones inestables que permiten formar fracturas tensionales, promover la inyección de diques a través de las paredes de los reservorios (Jellinek et al., 2004; Violette et al., 2001) y ocasionar una erupción volcánica explosiva (ej., Sulpizio et al., 2017) en sistemas volcánicos con elevado contenido de gases.

La descompresión ocasionada por una desglaciación, puede desde decenas a miles de años, incrementar los volúmenes erupcionados en las zonas volcánicas que fueron cubiertas por glaciares (Hooper et al., 2011), debido a descompresión del manto astenosférico que aumentaría la productividad de fundido y una tasa de descompresión máxima en la litosfera (Schmidt et al., 2013) que proporciona condiciones inestables en los reservorios poco profundos. Esto puede estar reflejado por el incremento de la actividad volcánica global en un factor de 2 a 6 durante el período postglacial entre 12 y 7 ka en regiones anteriormente afectadas por glaciares (Huybers y Langmuir, 2009). En el caso de Islandia, el volumen de lava emitido durante 2000 años después (~12 ka AP) de finalizar la última glaciación, fue hasta 100 veces superior al generado en períodos más recientes hace ~5 ka AP (MacLennan et al., 2002). Si es cierto que el impacto de la desglaciación en ambientes de arcos fue mucho menor que lo observado en rift y en intraplaca (Watt et al., 2013), no es bien entendido la magnitud de este impacto en las zonas volcánicas del sur de Chile.



La ZVS (33°- 46°S) en los Andes del Sur (López-Escobar et al., 1995), durante el UMG (~18 ka) fue cubierta al sur de los 38°S por extensos glaciares con espesores mayores a 1000 m y más de 300 km de ancho (E-W) en la Patagonia (Andersen et al., 1999; McCulloch et al., 2000). La desglaciación fue rápida, con disminución de espesores de hasta 1000 m dentro de los primeros 1000 años posteriores al UMG (Boex et al., 2013). En la ZVS, la frecuencia eruptiva a principios del período postglacial fue aproximadamente el doble que la media de todo el período postglacial. Además, en la ZVS el período postglacial temprano también coincide con un pequeño número de grandes erupciones explosivas de los volcanes más activos, consistente con una mayor acumulación de magma durante la glaciación y liberación de magma durante la desglaciación (Watt et al., 2013).

1.2 Hipótesis

El rebote elástico de la corteza superior debido a deflexión durante desglaciación es un mecanismo de primer orden en la descompresión y activación de sistemas volcánicos superficiales.

1.3 Objetivos

1.3.1 Objetivo general

La presente tesis tiene por objetivo general determinar las variaciones espacio-temporales del campo de esfuerzos y presiones debido a la deflexión ocasionada por el rebote elástico de la corteza superior durante una desglaciación sobre arcos volcánicos en zonas de subducción de latitudes altas y su impacto en cámaras magmáticas superficiales.

1.3.2 Objetivos específicos

A continuación se presentan los tres objetivos específicos de esta tesis:

- Estudiar la historia de desglaciación de los Andes del Sur, junto con comprender las relaciones espacio-temporales entre desglaciación y ocurrencia de erupciones explosivas.
- Analizar el efecto de los patrones elásticos (espesor elástico d , razón de Poisson ν , módulo de Young E), contraste de densidad $\Delta\rho$ (fundación placa elástica - hielo glaciar) y dimensiones de la carga (radio R y espesor glaciar h) en las variaciones espacio-temporales del campo de esfuerzo y presiones resultantes de la deflexión de la corteza superior.
- Estimar el tiempo de retardo entre el inicio de la desglaciación y la descompresión de reservorios magmáticos superficiales, asociada a erupciones explosivas postglaciares.

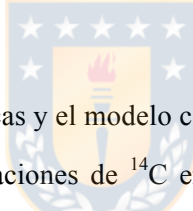
1.4 Metodología

Las dos principales metodologías utilizadas son: a) recopilación de información y creación de bases de datos con mapas de la extensión de los glaciares y tablas con edades del UMG, la desglaciación en los Andes del sur y erupciones explosivas postglaciares; b) programación de ecuaciones de flexura de placas delgadas elásticas en lenguaje python.

1.4.1 Último máximo glacial en los Andes del sur

El último máximo glacial (UMG) fue un fenómeno climático que afectó a ambos hemisferios (Denton et al., 2010) iniciando hace 33-26.5 ka AP y alcanzando una máxima extensión de los hielos hace 26.5-19 ka AP (Clark et al. 2009; Fogwill et al. 2015), donde grandes masas glaciares cubrieron principalmente América del Norte, Groenlandia, Europa y el sur de Sudamérica.

Durante el UMG en el sur de Sudamérica (Figura 1.1) la gran masa glaciar probablemente estuvo conformada por varios glaciares de montaña que descendieron hacia ambos lados de la cordillera, coalescendo y terminando en lóbulos glaciares de pie de monte que construyeron muchas de las actuales cuencas lacustres de elongación este-oeste en el sur de Chile y Argentina (Laugéne, 1971; Laugéne, 1982; Clapperton et al., 1994; Denton et al., 1999). Esta gran masa de hielo se extendió ~2000 km (~38-56°S) y con hasta ~300 km de ancho desde el borde costero oeste hasta más allá de la cordillera Patagónica (Caldenius, 1932; Hollín & Schilling, 1981; Singer et al., 2004), generando un volumen de hielo estimado en ~500 x 10³ km³ (Hulton et al., 2002). Hacia el norte de los ~38°S las masas glaciares se habrían relegado a zonas cordilleranas altas como glaciares de montaña menores hasta ~30°S (Clapperton et al., 1994).



1.4.2 Relaciones entre evidencias empíricas y el modelo climático

Las evidencias empíricas en base a dataciones de ¹⁴C en clastos con materia orgánica contenida en depósitos glacilacustres, morrenas y niveles piroclásticos indican que el UMG en el sur de Sudamérica se inició hace 33-30 ka cal AP (Lowell et al., 1995; Denton et al., 1999; Heusser et al., 1999), finalizando hace 18.9-15.6 ka cal AP (Heusser & Flint 1977; Mercer, 1983; Denton et al., 1999; McCulloch et al., 2000; Kaplan et al., 2004; Moreno & Clavero, 2006).

El último avance glaciar del UMG habría sido casi sincrónico en todas las latitudes (Figura 1.1; Tabla 1.1), ocurriendo en el lago Villarrica (~39°S) antes de la depositación de la ignimbrita Licán de edad 17.4-16.9 a 16.8-16.1 ka cal AP (Clavero & Moreno, 1994; Clayton et al., 1997; Moreno & Clavero, 2006; Lohmar et al., 2007; Lohmar, 2008), en las proximidades de la Isla Grande de Chiloé (~41-42°S) a los 18.8 – 17.4 ka cal AP (Heusser & Flint 1977; Mercer, 1983; Denton et al., 1999), en el Lago Buenos Aires- General Carrera (~46°S) a los 17.3-15.6 ka cal AP (Kaplan et al., 2004) y en las proximidades de Punta Arenas y el Estrecho de Magallanes (~53°S) a los 18.9-17.5 ka cal AP (McCulloch et al., 2000). Estos datos empíricos permiten establecer zonas con diferentes rangos de tiempo (relativamente sincrónicos) para el último máximo glaciar, es decir, el máximo límite de tiempo

de los avances glaciares antes del inicio de la desglaciación: 1) 39°- 41°S (17.4 – 16.9 ka cal AP); 2) 41°- 45°S (18.8-17.4 ka cal AP); 3) 45° - 50°S (17.3 -15.6 ka cal AP); 4) 50°-56° (18.9-17.5 ka cal AP).

El límite del UMG (Figura 1.1) está bien definido en estudios de geomorfología y de los depósitos glaciares en el sur de Chile y Argentina (Caldenius, 1932; Laugénie, 1971; Laugénie, 1982; Clapperton et al., 1994; Denton et al., 1999; Singer et al., 2004), donde los glaciares habrían cubierto un área $\sim 453 \times 10^3 \text{ km}^2$. En contraste a lo anterior, de acuerdo a los modelos climáticos que simulan la masa de hielo del UMG (Hulton et al., 2002; Sudgen et al., 2002), estos habrían cubierto un área $\sim 531 \times 10^3 \text{ km}^2$, excediendo en $\sim 18\%$ el área estimada por los registros empíricos. Si bien, los modelos climáticos exageran el área y el volumen de la masa glaciar y no reproducen la extensión de los hielos sobre la Isla Glande de Chiloé; la extensión general de los glaciares, el volumen y principalmente, el espesor estimado del hielo son aproximadamente válidos y pueden ser utilizados en el experimento de modelación numérica del presente trabajo.



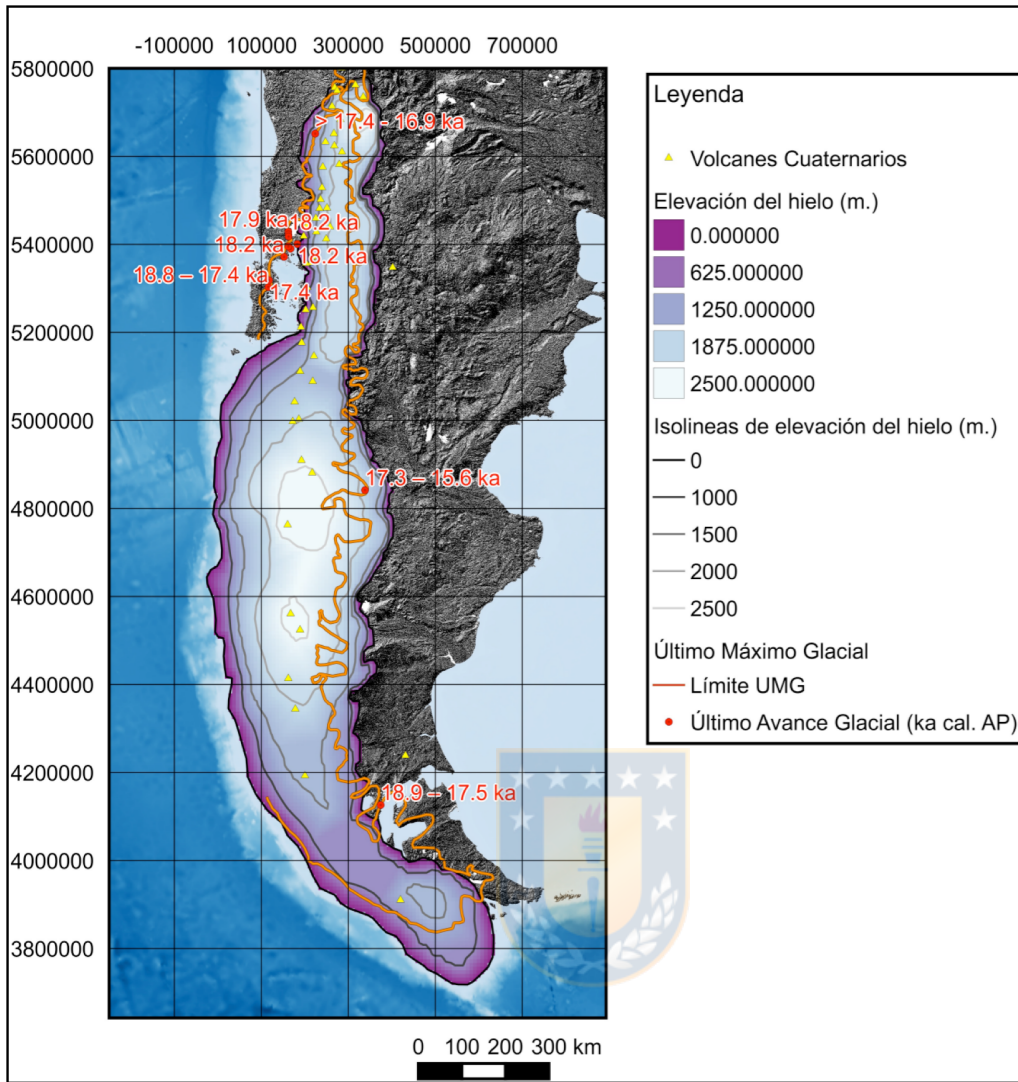


Figura 1.1: Representación del modelo climático y evidencias empíricas del UMG en los Andes del Sur.

Extensión de la masa glaciar, elevación del hielo e isolineas de elevación del hielo (Hulton et al., 2002; Sudgen et al., 2002). Evidencias empíricas del límite del UMG (Caldenius, 1932; Laugerie, 1971; Denton et al., 1999; Singer et al., 2004). Edades ^{14}C ka AP del último avance glacial del UMG (Heusser & Flint, 1977; Mercer, 1983; Denton et al., 1999; McCulloch et al., 2000; Kaplan et al., 2004; Moreno & Clavero, 2006) expresadas en miles de años calendario antes del presente (ka cal AP) según cálculos aproximados de calibración de radiocarbono efectuados con CalPal-Online (<http://www.calpal-online.de/>).

Tabla 1.1: Dataciones ^{14}C del último avance glacial del UMG en los Andes del Sur.

Estas fueron transformadas a miles de años calendario antes del presente (ka cal AP) según cálculos de calibración aproximados de radiocarbono efectuados con CalPal-Online (<http://www.calpal-online.de/>).

Lat.	Long.	Localidad	Datación años ^{14}C	ka cal AP	Observaciones	Referencias
-39.24	-72.20	Ribera Oeste Lago Villarrica	>14200/ 13910±60/ 13990±100/ 13800	>17.4- 16.9 (*16.8- 16.1)	Edad ignimbrita Licán. Edad máxima para las morrenas subyacentes. Edad mínima desglaciación.	Clavero & Moreno (1994); Clayton et al.(1997); Lohmar et al. (2007); *Lohmar (2008); Moreno & Clavero (2006)
-41.22	-73.03	Sitio Puerto Phillipi (cerca de Lago Llanquihue)	14650	17.9	Avance más joven de glaciar pie de monte.	Denton et al. (1999)
-41.28	-73.03	Sitio Fundo Llanquihue	14869	18.2	Avance más joven de glaciar pie de monte.	Denton et al. (1999)
-41.32	-73.03	Sitio Northwest Bluff - Sitio Calle Santa Rosa - Sitio railroad bridge - Sitio Bella vista Bluff	14882/14820/ 14613 – 14550/ 14540	18.2-17.7	Avance más joven de glaciar pie de monte.	Denton et al. (1999)
-41.57	-72.99	Isla Maillen (cerca de Seno de Reloncaví)	15220	18.3	Avance más joven de glaciar pie de monte.	Denton et al. (1999)
-41.48	-72.80	Punta Penas	14879	18.2	Avance más joven de glaciar pie de monte.	Denton et al. (1999)
-41.52	-73.05	Canal Tengo	15040	18.3	Avance más joven de glaciar pie de monte.	Denton et al. (1999)
-41.73	-73.18	Sitio Calbuco (Golfo de Ancud)	14900	18.2	Avance más joven de glaciar pie de monte.	Denton et al. (1999)
-42.33	-73.66	Dalcahue (Este Isla Grande de Chiloé)	15600±560/ 14970±210/ 14805/ 14355±700	18.8-17.4	Avance más joven de glaciar pie de monte. Datación en clastos orgánicos (madera) entre tilitas.	Mercer (1983); Denton et al. (1999)
-42.19	-73.63	Sitio Taiquemó (Este de Isla Grande de Chiloé)	14120±150	17.4	Avance más joven de glaciar pie de monte.	Heusser & Flint (1977)
-46.56	-71.11	Lago General Carrera (Lago Buenos Aires)	14065±345/ 12840±130/ 12880±160	17.3-15.6	Datacion en sedimentos de varves lacustres sobre la morrena más joven.	Kaplan et al. (2004)
-53.00	-70.87	Punta Arenas y Estrecho de Magallanes.	15600 - 14300	18.9 -17.5	Dataciones en polen sugieren un enfriamiento registrado en el aumento de las plantas tipo arbustos y una pérdida de Myriophyllum (algas de agua dulce indicadora de un clima más cálido).	McCulloch et al. (2000)

1.4.3 Desglaciación en los Andes del Sur

Los estudios del registro de la paleovegetación indican que el proceso de desglaciación ocurrió durante un calentamiento en tres etapas (Denton et al., 1999; McCulloch et al., 2000), evidenciado en el reemplazo de la vegetación con afinidad al frío (ej.: arbustos y gramíneas) por una vegetación con afinidad al calor (ej.: Nothofagus y Myriophyllum). La primera etapa de calentamiento que siguió al último avance glaciar del UMG (o última terminación), dando inicio a una transición glacial/interglacial aproximadamente a los 14600 - 14300 ^{14}C años AP (17.9 – 17.5 ka cal AP; Tabla 1.2) fue sincrónica en todas las latitudes. La segunda etapa de calentamiento es registrada a los 13000-12700 ^{14}C años AP (15.9 – 14.6 cal AP; Tabla 1.3), siendo más evidente en los registros de polen en la Región de los Lagos de Chile y no es observada en el Estrecho de Magallanes. La tercera etapa de calentamiento afectó a todas las latitudes, aproximadamente a los 10300 - 9500 ^{14}C años AP (12.2 – 10.7 ka cal AP; Tabla 1.4), pero fue más dominante en el sur.

Los límites glaciares durante la desglaciación en las tres etapas de calentamiento son inferidas a través de datos empíricos del estudio de la paleovegetación (McCulloch et al., 2000) y muestran algunas diferencias con el modelo climático de Hulton et al. (2002).

Según el modelo climático, después de 300 años siguiendo la desglaciación, aún persiste una cubierta glaciar en el trasarco al norte de los 43°S, no evidenciado por la interpretación empírica y al sur de 43°S el modelo exagera el ancho de la masa glaciar en contraste a la interpretación empírica que muestra una cubierta glaciar más angosta y relegada al arco volcánico (Figura 1.2).

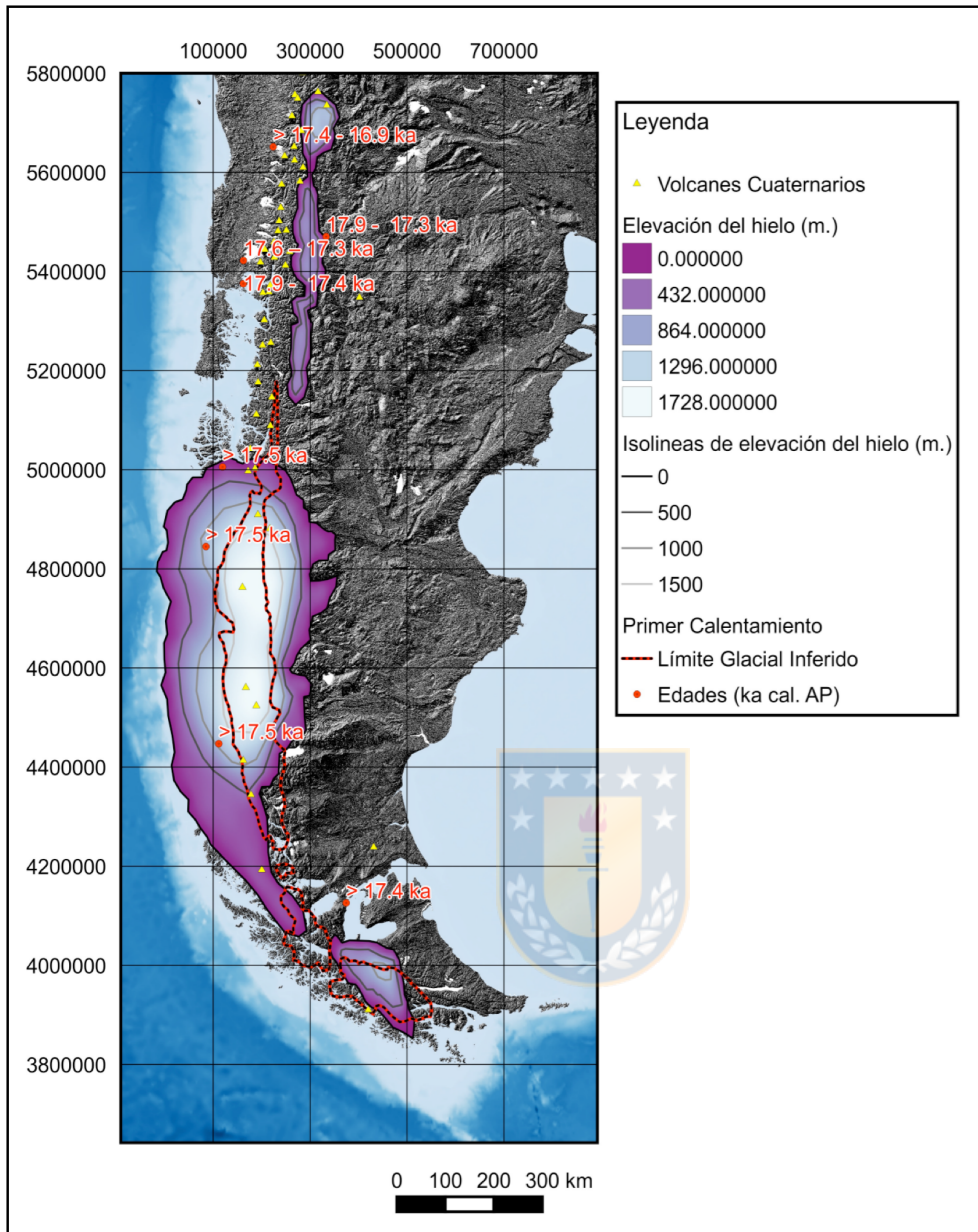


Figura 1.2: Representación del modelo climático 300 años siguiendo la desglaciación y evidencias empíricas del primer calentamiento en los Andes del Sur.

Extensión de la masa glaciar, elevación del hielo e isolineas de elevación del hielo (Hulton et al., 2002). Límite glaciar inferido de evidencias empíricas (McCulloch et al., 2000). Edades ^{14}C ka AP del inicio de la desglaciación (Lumley & Switsur, 1993; Denton et al., 1999; Heusser et al., 1999; McCulloch et al., 2000; Moreno & Clavero, 2006; Tabla 1.2) expresadas en miles de años calendario antes del presente (ka cal AP) según cálculos de calibración de radiocarbono efectuados con CalPal-Online (<http://www.calpal-online.de/>).

Tabla 1.2: Dataciones ^{14}C del inicio de la desglaciación (Primer Calentamiento) en los Andes del Sur.

Estas fueron transformadas a miles de años calendario antes del presente (ka cal AP) según cálculos aproximados de calibración de radiocarbono efectuados con CalPal-Online (<http://www.calpal-online.de/>).

Lat.	Long.	Localidad	Datación años ^{14}C	ka cal AP	Observaciones	Referencias
-39.24	-72.20	Ribera Oeste Villarrica	Lago $>14200/$ $13910\pm60/$ $13990\pm100/$ 13800	$>17.4-$ 16.9 (16.8- 16.1)	Edad ignimbrita Licán. Edad máxima para las morrenas subyacentes. Edad mínima desglaciación.	Clavero & Moreno (1994); Clayton et al. (1997); Lohmar et al.(2007); Lohmar (2008); Moreno & Clavero (2006)
-41.28	-73.03	Sitio Llanquihue	Fundo	$14,470\pm100-$ 14055 ± 155	17.6- 17.3	Fin del UMG. Inicio de desglaciación. Aparecen Nothofagus en un dominio de Gramineas.
-40.90	-70.98	Sitio Puntilla Llanquihue)	Canal de la (Lago	14600-14100	17.9- 17.3	Rápido cambio de la vegetación. Desaparece Parkland y aparece el Evergreen Forest de Nothofagus.
-41.70	-73.06	Sitio Huelmo (Seno de Reloncaví)		14600-14200	17.9- 17.4	Rápido cambio de la vegetación. Desaparece Parkland y aparece el Evergreen Forest de Nothofagus.
-45.00	-73.83	Latitudes centrales		> 14335	> 17.5	El hielo se ubica a 50 km de su actual posición en la Península de Taitao.
-46.42	-74.40	Laguna Stibnite en Península de Taitao. Campos Hielo Norte.		$> 14335\pm145$	> 17.5	Campos de Hielo Patagonico Norte. Datacion de polen. Expansión Bosque de Nothofagus.
-50.00	-74.74	Latitudes centrales		> 14335	> 17.5	El hielo se ubica a 50 km de su actual posición en la Península de Taitao.
-53.00	-70.87	Punta Arenas – Estrecho de Magallanes		> 14260	> 17.4	El hielo demoró 4000 años más en retirarse, en relación a la Región de Los Lagos y las latitudes centrales.

Tabla 1.3: Dataciones ^{14}C de la desglaciación (Segundo Calentamiento) en los Andes del Sur.

Estas fueron transformadas a miles de años calendario antes del presente (ka cal AP) según cálculos aproximados de calibración de radiocarbono efectuados con CalPal-Online (<http://www.calpal-online.de/>).

Lat.	Long.	Localidad	Datación años ^{14}C	ka cal. AP	Observaciones	Referencia
-42.19	-73.63	Sitio Taiquemó (Este de Isla Grande de Chiloé)	13040±98	15.9	Datación de Polen en Morrena. Fin del Subantarctic Parkland. Dominio del Evergreen Forest.	Heusser et al. (1999)
-42.97	-73.70	Chadmo (pocos km al N de Quellón)	13065±320	15.9	Datación clastos orgánicos en turba	Heusser & Flint (1977)
-43.11	-73.76	Puerto Carmen (pocos km al W-SW de Quellón)	13040±210	15.9	Datación clastos orgánicos en turba.	Villagrán (1988)
-43.49	-72.36	Sitio Cuesta Moraga	12310±360	14.6	Datación clastos orgánicos en turba. Desglaciación avanzada (~1000 años ^{14}C después del inicio del segundo calentamiento a los ~13000 ^{14}C años AP el hielo había retrocedido ~200 km hacia el Este)	Heusser (1990)



El segundo calentamiento ocurrió aproximadamente 2000 años calendario después del inicio de la desglaciación (Tabla 1.3; ej.: Heusser et al., 1999) y el modelo climático pronostica que el volumen de hielo es aproximadamente una quinta parte del volumen del UMG (Hulton et al., 2002). Según la tendencia del modelo climático, el volumen de hielo está concentrado en los campos de hielo Patagónicos y poco o nada de hielo persiste en el extremo sur. Esto último no es reflejado en las tendencias de una persistencia del hielo glaciar en el extremo sur, según las interpretaciones empíricas (ej.: McCulloch et al., 2000).

El tercer calentamiento ocurrió aproximadamente unos ~6000 años calendarios después del UMG (Tabla 1.4). Tanto el modelo climático y las interpretaciones empíricas coinciden en la separación en dos partes de los campos de hielo Patagónico (Figura 1.3). En tanto, la tendencia de las interpretaciones empíricas a una permanencia de los hielos en el extremo sur, no es simulada por el modelo climático y este indica una ausencia de glaciares.

Tabla 1.4: Dataciones ^{14}C de la desglaciación (Tercer Calentamiento) en los Andes del Sur.

Estas fueron transformadas a miles de años calendario antes del presente (ka cal AP) según cálculos aproximados de calibración de radiocarbono efectuados con CalPal-Online (<http://www.calpal-online.de/>).

Latitud	Longitud	Localidad	Datación años ^{14}C	ka cal AP	Observaciones	Referencia
-46.42	-74.40	Laguna Stibnite en Penisula de Taitao. Campos Hielo Norte.	10000-9500	11.5-10.7	-	Lumley & Switsur (1993)
-53.00	-70.87	Punta Arenas- Estrecho de Magallanes	10300	12.2	-	McCulloch et al. (2000)

A pesar de algunas discrepancias entre las evidencias empíricas y el modelo climáticos, este último es considerado una buena aproximación de los volúmenes y espesores glaciares (Hulton et al., 2002), por lo tanto es un modelo suficientemente válido para ser aplicado en el experimento de simulación numérica en esta tesis.



Algunos antecedentes de modelación numérica a escala global indican que el alzamiento actual en la Patagonia por efecto del UMG es de ~0.6 mm/año (Peltier, 2004) y a escala regional es 0.3-1.5 mm/año (Ivins & James, 1999). Este último trabajo indica que en la actualidad el alzamiento en la Patagonia es más afectado por la "Pequeña Era del Hielo (LIA)" (~1650-1850AD) con valores de 1-20 mm/años, en similitud a mediciones de gps que indican > 35 mm/años en el centro de los campos de Hielo Sur Patagónicos (Lange et al., 2014). Esto último, muestra que una desglaciación puede tener una significativa influencia en modificar el estado de esfuerzos en la corteza superior al menos dentro de los primeros 200 años de desglaciación. Dado que el principal interés de la presente tesis es modelar el estado de esfuerzos y presiones inducidas por la desglaciación en la corteza superior para investigar su impacto en sistemas volcánicos superficiales, no fue necesario estimar el alzamiento por efecto de la desglaciación con los modelos implementados.

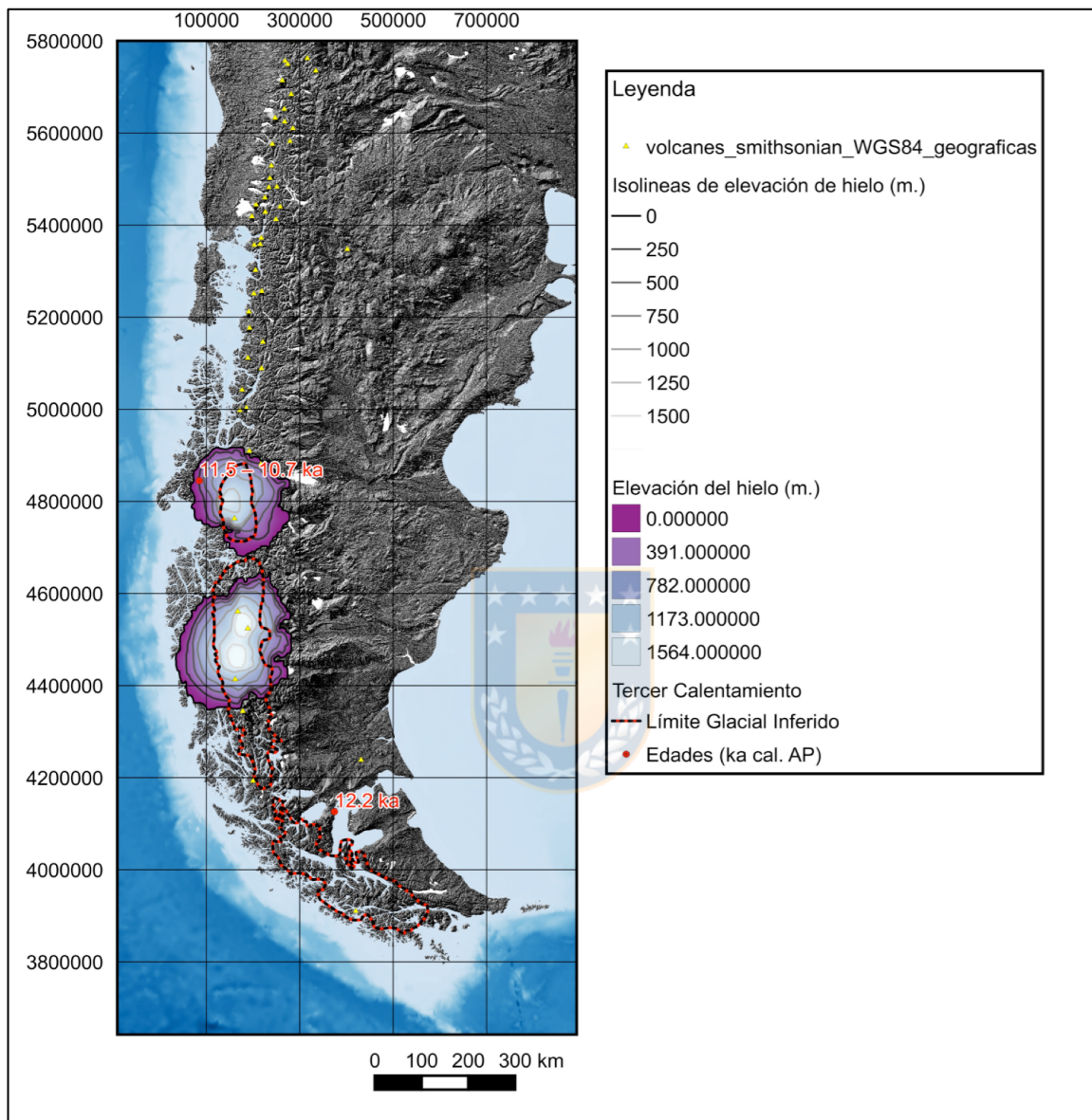


Figura 1.3: Representación del modelo climático 5000 años siguiendo la desglaciación y evidencias empíricas del tercer calentamiento en los Andes del Sur.

Extensión de la masa glaciar, elevación del hielo e isolineas de elevación del hielo (Hulton et al., 2002). Límite glaciar inferido de evidencias empíricas (McCulloch et al., 2000). Edades ^{14}C ka AP del inicio del tercer calentamiento (Lumley & Switsur, 1993; McCulloch et al., 2000; Tabla 1.4) expresadas en miles de años calendario antes del presente (ka cal AP) según cálculos aproximados de calibración de radiocarbono efectuados con CalPal-Online (<http://www.calpal-online.de/>).

Los resultados de esta base de dato permitirán configurar las variaciones espacio-temporales de las cargas superficiales aplicadas en la modelación.

1.4.4 Erupciones explosivas postglaciares en la ZVS de los Andes del Sur

Los análisis de los registros de erupciones mundiales indican que la tasa de erupciones en regiones anteriormente cubiertas por glaciares incrementó por un factor de 2 a 6 globalmente desde 12 a 7 ka (Huybers & Langmuir, 2009). Las estadísticas de las erupciones globales analizadas por Watt et al. (2013) sugieren que entre 13 y 7 ka existió un aumento máximo de la tasa eruptiva por un factor de 2 (o menos) en relación con la actualidad, pero advierten que la variabilidad espacial de los registros eruptivos puede exagerar el aparente aumento postglacial en el volcanismo y evitar la cuantificación precisa del verdadero patrón.

Al sur de los ~41°S en la ZVS (López-Escobar et al., 1995), donde la descarga de hielo fue más grande después del UMG, la frecuencia eruptiva a principios del período postglacial (Watt et al., 2013) fue aproximadamente el doble que la media del período postglacial. Entre las latitudes ~38° y 46°S en la ZVS, el período postglacial temprano también coincide con un pequeño número de grandes erupciones explosivas de los volcanes más activos, consistente con una mayor acumulación de magma durante la glaciación y liberación de magma durante la desglaciación (Watt et al., 2013).

Existe un lapso de 1-2 ka entre la retirada final del hielo y los primeros depósitos de tefras postglaciales registrados en el sur de Chile. El lapso de tiempo que transcurre en Chile puede reflejar una escala de tiempo característico del ascenso del magma en la corteza o también puede reflejar el momento de máxima deformación de la corteza superior tras la retirada del hielo. Estas erupciones podrían ser explicadas por la liberación de magma acumulado y no necesariamente por el aumento de la producción de magma (Watt et al., 2013).

Los trabajos de Watt et al. (2013), Weller et al. (2014), Fontijn et al. (2014) y Rawson et al. (2015) evidencian el continuo progreso en el entendimiento de las historias eruptivas de los volcanes de la ZVS (33° - 46°S) y existe una incompleta lista de estimaciones de volúmenes erupcionados en tiempos postglaciares. A pesar de lo anterior, estos trabajos intentan describir lo mejor posible la historia eruptiva postglacial y permiten una mejor comprensión de la evolución eruptiva del arco volcánico en tiempos postglaciares (Figura 1.4).

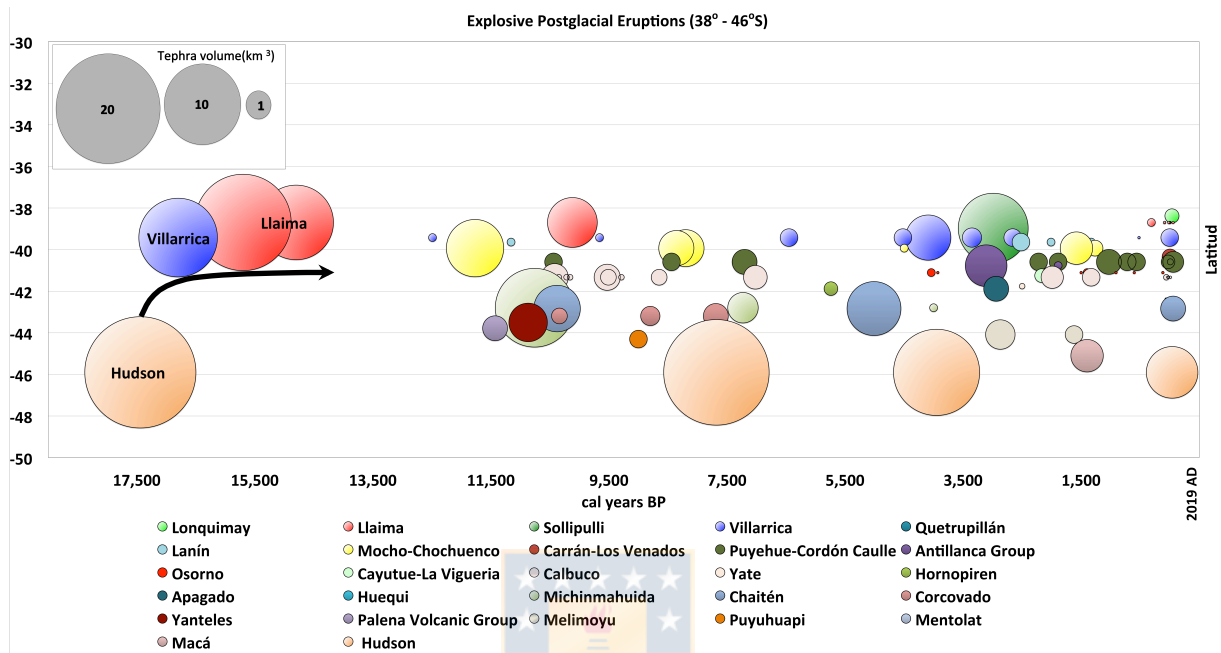


Figura 1.4: Erupciones explosivas postglaciares en ZVS de los Andes del Sur.

Base de datos (Fontijn et al., 2014; Rawson et al., 2015; Watt et al., 2013; Weller et al., 2014). Se consideran solo erupciones con volúmenes $> 0.01 \text{ km}^3$. Se destacan las erupciones postglaciares de los volcanes: Llaima (Ignimbritas Curacautín 1 y 2; 15 y 9 km^3 ; 15.7 y 14.8 ka cal AP; Lohmar, 2008), Villarrica (Ignimbritas Licán, 10 km^3 ; 16.8-16.1 ka cal AP; Lohmar, 2008) y Hudson (tefras H₀; 20 km^3 ; 17.4-17.3 ka cal. AP; Weller et al., 2014). Existe una tendencia temporal aparente (flecha color negro) en la ocurrencia de estas erupciones, relacionadas con una mayor magnitud de la carga inicial en el sur respecto del norte.

De acuerdo con Rawson et. al (2016), las cargas y descargas glaciares permitirían en algunos caso modular la evolución del magmatismo de los reservorios al afectar el campo de esfuerzos de estos, explicando el magmatismo bimodal observado en el volcán Mocho-Chochuenco y probablemente otros volcanes de la ZVS (ej: volcanes: Lonquimay, Gilbert et al., 2014; Puyehue, Singer et al., 2008). Estas observaciones son consistentes con un mecanismo en el cual la descarga afecta el almacenamiento de magma en la escala de tiempo a través de cambios en el régimen de esfuerzos corticales, en lugar de cambios en las tasas de fusión del manto (se considera un flujo de magma quasi-estable dentro de la corteza a escala de decenas de miles de años; Rawson et al., 2016). Aunque este modelo no explicaría

la menor evolución composicional de los productos eruptivos postglaciares andesítico-basálticos a andesíticos de otros volcanes particulares de la ZVS de conducto abierto (ej.: Llaima: Schindlbeck et al., 2014; Villarrica: Lohmar, 2008), donde los magmas pre-erutivos solo alcanzaron a evolucionar a composiciones andestíticas previo a la inyección de un magma basáltico (Clavero & Moreno, 1994; Lohmar, 2008). El modelo conceptual de Rawson et al. (2016) basado en las observaciones del registro eruptivo del volcán Mocho-Choshuenco (Rawson et al., 2015) indica una baja frecuencia eruptiva (f_e = erupciones/ka) durante la glaciación ($f_e=1$; 40-20 ka AP), aumento de la frecuencia eruptiva al inicio del postglacial ($f_e=2$; 18-7 ka AP) y un nuevo aumento a finales del postglacial ($f_e=80$; 5-0 ka AP). Esto es consistente con estudios de la frecuencia eruptiva a nivel global para regiones afectadas por glaciación/desglaciación (ej.: Watt et al., 2013).

Las erupciones explosivas postglaciares de la ZVS (Figura 1.4) permite entender la reacción del arco volcánico a la desglaciación y establecer relaciones espacio-temporales con los resultados de la modelación numérica en la cual se espera observar cambios del campo de esfuerzos y descompresiones afectando reservorios superficiales en la corteza superior. Dentro de las erupciones postglaciares, son destacables los eventos ocurridos en los primeros 2000 años de desglaciación en los volcanes Hudson, Villarrica y Llaima, indicando una probable relación espacio-temporal de la respuesta elástica de la corteza superior y el arco volcánico a la desglaciación. Asumiendo que la desglaciación se inicia relativamente sincrónica, parece existir una relación entre magnitud de la carga inicial y ocurrencia de erupciones, donde las áreas con cargas iniciales mayores son las primeras en responder con erupciones explosivas durante la desglaciación en la ZVS y las áreas volcánicas con menor carga inicial muestran una respuesta más tardía a la descarga glaciar. A continuación se describen brevemente las primeras erupciones explosivas postglaciares de los volcanes Hudson, Villarrica y Llaima:

Erupción postglacial del Hudson: tefras H_0

Los estudios de sedimentos en los lagos postglaciares del sur de los Andes indican la presencia de la mayor erupción de tefras del volcán Hudson, las tefras H_0 de edad 17.44-17.30 ka cal AP (Weller et al., 2014), posterior al inicio de la desglaciación en esta área a los 17.90 ka cal AP (Miranda et al., 2013). En 13 muestras de seis lagos ubicados ~100 km al noreste del volcán Hudson, las tefras tienen un rango de espesor 55-80 cm, conteniendo granos de pómex > 2 cm de diámetro máximo (Weller et al., 2014). El volumen estimado de estas tefras es > 20 km³, siendo la mayor erupción postglaciar

documentada de los volcánicos de los Andes del sur y probablemente responsable de la formación de una caldera de 10 km de ancho en el Hudson (Weller et al., 2014). Esta erupción de gran volumen es consistente con un aumento de la actividad volcánica en la ZVS en el inicio del postglacial en relación al presente (Watt et al., 2013). Las tefras H₀ es un depósito bimodal, conformado por una mayor proporción de densos fragmentos de vidrio oscuro basáltico-traquianandesítico y pómex, con vidrio de 55-59% SiO₂ y con una menor proporción de pómex claras traquidacíticas con vidrio de 66% SiO₂.

En general, el magmatismo bimodal, la concentración de elementos trazas y el decrecimiento de Dy/Yb (Kratzmann et al., 2009, 2010) en cada una de las erupciones postglaciares del volcán Hudson pueden ser explicadas por cristalización fraccionada de anfíbol desde un magma parental basáltico a > 6 km de profundidad (Davidson et al., 2007), seguido de la desaparición de anfíbol debido a un decrecimiento de la presión e incremento de la temperatura, como resultado de descompresión por cristalización cuando los magmas migran hacia la superficie. Además, las erupciones postglaciares del Hudson indican una evolución promedio desde magmas más máficos a menos máficos desde el postglaciar temprano al presente, junto con el decrecimiento de los volúmenes erupcionados (Weller et al., 2014).



Erupción postglacial del Villarrica: Ignimbritas Licán

Las Ignimbritas Licán se disponen directamente sobre depósitos morrénicos, fluvioglaciarios y glacilacustres de la última glaciación o rocas glaciadas del basamento (Clavero & Moreno, 1994), cubren una superficie aproximada de 2000 km², con un espesor máximo de 20 m y un espesor mínimo de 10 m (~20 km al NE de la fuente) y se distribuyen de forma radial en torno al edificio volcánico (Clavero & Moreno, 1994), constituyendo un volumen de ~10 km³ (Lohmar et al., 2012). La datación de ¹⁴C (13.800 – 13.850 años AP; edades calibradas aproximadas: 16.1-16.8 ka cal AP) por Moreno & Clavero (2006) y Lohmar (2008), confirman que las ignimbritas Licán fueron emitidas varios siglos después del evento de aumento de las temperaturas climáticas, el cual se inició a los 14.600 años AP (edad calibrada aproximada: 17.9 ka cal AP) según dataciones ¹⁴C por McCulloch et al. (2000). Esta gran erupción originó una caldera anidada en una mayor preglaciaria de 4,2 x 6,5 km (Clavero & Moreno, 1994).

Su composición es andesita-basáltica con 55-58% SiO₂, donde la cristalización fraccionada de olivino, piroxeno y plagioclasa es el mayor proceso responsable de la evolución del magma que originó este depósito (ej.: Hickey-Vargas et al., 2004). Existen evidencias petrológicas donde la mezcla de magma

fue otro proceso importante involucrado en la formación de las ignimbritas Licán (Lohmar et al., 2007), ejemplo de ello son los núcleos reabsorbidos de clinopiroxeno y ortopiroxeno pobres en Mg y rodeados por un anillo rico en Mg. Entonces, la inyección de un pulso de magma máfico desde un reservorio más profundo y un rápido ascenso y descompresión del magma en la cámara, habría ocasionado esta erupción explosiva (Lohmar et al., 2012). Según Lohmar et al. (2007), la elevada explosividad de la ignimbrita Licán sería atribuida a su alto contenido de gases (origen mantélico o asimilación cortical) y al freatomagmatismo. Además, desconociéndose el mecanismo que relaciona la descarga glaciar con las erupciones explosivas, Lohmar et al. (2012) especulan un posible efecto de la desglaciación en la descompresión del reservorio del volcán Villarrica.

Erupción postglacial del Llaima: Ignimbritas Curacautín

Las ignimbritas Curacautín del volcán Llaima (volumen ~ 24 km³) corresponde a un conjunto de flujos y oleadas piroclásticas con una composición promedio andesita-basáltica (51-58% SiO₂) que muestra el bajo grado de diferenciación de estos productos. En cada unidad, los productos menos diferenciados (51-54% SiO₂; grupo básico) registran una evolución por fraccionamiento convectivo, mientras que la mineralogía y geoquímica de rocas más diferenciadas (56-58% SiO₂; grupo ácido) revelan dos procesos: cristalización fraccionada y mezcla de magmas, en la cual habría participado un componente riodacítico. Además, estas ignimbritas presentan evidencias de freatomagmatismo (Lohmar, 2008).

Las ignimbritas Curacautín se generaron en dos eventos, lo cual concuerda con las distinciones de diferentes unidades (Curacautín 1 y 2) en terreno. Las dataciones de ¹⁴C sugieren que la unidad Curacautín 1 se habría depositado ~13200 años AP y la unidad Curacutín 2 hace ~12600 años AP. Las edades calibradas sugieren que la unidad inferior corresponde a un evento que ocurrió unos 15.7 cal ka AP, mientras que la erupción de los flujos superiores se produjo hace unos 14.8 ka cal AP (Lohmar, 2008). Estas erupciones habrían generado una caldera ~6-8 km de diámetro en el edificio primitivo del volcán Llaima y estaría completamente cubierta por el actual cono volcánico (Naranjo & Moreno, 1991, 2005).

1.4.5 Modelos de flexura de placas delgadas

Utilizando lenguaje de programación Python, se implementan ecuaciones para modelar el cambio de esfuerzos, la descompresión y su evolución espacio-tiempo (“salida”) debido a la deflexión de la corteza superior durante la desglaciación en los Andes del sur. Se utilizaron dos tipos de modelos: a) flexura de un disco elástico simplemente soportado (Ugural, 1981) y b) flexura de una placa de longitud infinita sobre una fundación de Winkler (Watts, 2001). Ambos modelos utilizan una historia de desglaciación simple (“entrada”) derivada del ajuste de curva del modelo de desglaciación de Hulton et al. (2002).

1.5 Conceptos básicos de esfuerzos, elasticidad y flexura de placas delgadas

1.5.1 Esfuerzos, Esfuerzos normales, Presión y deformación

Los *esfuerzos* son fuerzas por unidad de área transmitidas a través de los materiales por campos de fuerzas interatómicos. Los esfuerzos que son transmitidos perpendiculares a una superficie son llamados *esfuerzos normales*. El valor promedio de los esfuerzos normales es la *presión* (Turcotte & Schubert, 2014). Los esfuerzos aplicados sobre un sólido o material elástico resultan en la transmisión de estos en su interior y ocasionan *deformación* (reducción/aumento del volumen por esfuerzos compresivos/tensionales) en sólidos compresibles (Turcotte & Schubert, 2014).



1.5.2 Elasticidad lineal

Los *materiales elásticos* son aquellos que se deforman cuando son sometidos a esfuerzos y regresan a su forma original cuando el esfuerzo es removido, por lo tanto, la deformación elástica es un mecanismo reversible (Turcotte & Schubert, 2014). En general, las rocas sometidas a esfuerzos no muy grandes se comportan como materiales elásticos a relativamente bajas temperaturas y presiones. En adición, la deformación elástica (ϵ) de muchas rocas es linealmente proporcional a los esfuerzos (σ) aplicados, este es el concepto básico de la *elasticidad lineal* (Turcotte & Schubert, 2014). Las ecuaciones de elasticidad lineal son simplificadas en *materiales isótropos*, es decir, si sus propiedades elásticas son independientes de la dirección. La aproximación de material elástico-isótropo aplicada a la litosfera considera que esta no es deformada significativamente a escala de tiempo geológico menor a 10^9 años (Turcotte & Schubert, 2014). Esto es usualmente satisfactorio para la corteza terrestre y el manto superior en la litósfera (Turcotte & Schubert, 2014). Entonces, la elasticidad es el principal mecanismo de deformación aplicable a la litosfera (Turcotte & Schubert, 2014) y asumiremos que los

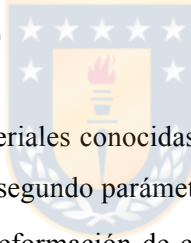
esfuerzos desarrollados en una placa elástica durante su flexura son linealmente proporcionales a sus deformaciones (Watts, 2001).

En un material elástico-lineal, homogéneo e isotropo, los esfuerzo aplicados son linealmente proporcionales a sus deformaciones y sus propiedades mecánicas no tienen una orientación preferida (ej., Watts, 2001). Consideremos un sistema de coordenadas Cartesiano donde los ejes principales de esfuerzos y deformaciones coinciden en tal medio, donde para cualquier vector de esfuerzos existen tres componentes escalares de esfuerzos principales ($\sigma_1, \sigma_2, \sigma_3$) referidos respectivamente a los ejes (x,y,z) y asociados a las deformaciones principales ($\varepsilon_1, \varepsilon_2, \varepsilon_3$). En el caso de un *estado de esfuerzos tridimensional*, las relaciones entre esfuerzos y deformaciones son definidas en las ecuaciones de elasticidad lineal de la *ley de Hook generalizada*, válido para un material isotropo homogéneo (ej., Turcotte & Schubert, 2014; Ugural, 1981; Watts, 2001):

$$\sigma_1 = (\lambda + 2G)\varepsilon_1 + \lambda\varepsilon_2 + \lambda\varepsilon_3 \quad (\text{Ec.1.1})$$

$$\sigma_2 = \lambda\varepsilon_1 + (\lambda + 2G)\varepsilon_2 + \lambda\varepsilon_3 \quad (\text{Ec.1.2})$$

$$\sigma_3 = \lambda\varepsilon_1 + \lambda\varepsilon_2 + (\lambda + 2G)\varepsilon_3 \quad (\text{Ec.1.3})$$



donde λ y G son propiedades de los materiales conocidas como “parámetros de Lamé”. λ es el primer parámetro de Lamé (ej.:Watts, 2001). El segundo parámetro de Lamé o módulo de rigidez o cizalla (G) es la razón entre esfuerzo de cizalla y deformación de cizalla en cizalla simple ($G = \frac{\tau_{ij}}{\gamma_{ij}}$; ej.: Watts, 2001). Las propiedades de los materiales son tales que una componente de deformación principal ε produce un esfuerzo $(\lambda+2G)\varepsilon$ en la misma dirección y esfuerzos $\lambda\varepsilon$ en las direcciones respectivamente perpendiculares (Turcotte & Schubert, 2014).

Reemplazando $G = \frac{E\nu}{2(1+\nu)}$ y $\lambda = \frac{Ev}{(1+\nu)(1-2\nu)}$, las ecuaciones Ec.(1.1-1.3) pueden ser escritas de una forma inversa (ej., Turcotte & Schubert, 2014; Ugural, 1981; Watts, 2001):

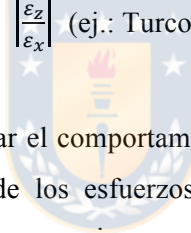
$$\varepsilon_1 = \frac{1}{E}\sigma_1 - \frac{\nu}{E}\sigma_2 - \frac{\nu}{E}\sigma_3 \quad (\text{Ec.1.4})$$

$$\varepsilon_2 = -\frac{\nu}{E}\sigma_1 + \frac{1}{E}\sigma_2 - \frac{\nu}{E}\sigma_3 \quad (\text{Ec.1.5})$$

$$\varepsilon_3 = -\frac{\nu}{E}\sigma_1 - \frac{\nu}{E}\sigma_2 + \frac{1}{E}\sigma_3 \quad (\text{Ec.1.6})$$

donde E y ν son propiedades de los materiales, conocidas como módulo de Young y razón de Poisson, respectivamente. Las ecuaciones Ec.(1.4-1.6) indican que una componente de esfuerzo principal σ produce una deformación $\frac{\sigma}{E}$ en la misma dirección y deformaciones $-\frac{\nu\sigma}{E}$ en las direcciones ortogonales respectivas (Turcotte & Schubert, 2014).

El módulo de Young (E) muestra la relación entre los incrementos de esfuerzos aplicados y los incrementos de deformación longitudinal unitaria producidos ($E = \frac{d\sigma}{d\varepsilon}$), es decir, corresponde a la tangente en cada punto de la curva ε v/s σ , es un valor constante positivo e independiente del esfuerzo aplicado, siempre que este último no sobrepase el límite elástico. Los materiales con mayor E son afectados por una menor deformación, en comparación a los materiales con menor E , en idénticas condiciones de esfuerzos aplicados. La razón de Poisson ν es la relación entre la deformaciones perpendicular y longitudinal a la fuerza aplicada. Por ejemplo, una barra sometida a un esfuerzo de tensión en la dirección x , será afectada por un estiramiento ε_x y acortamientos perpendiculares ε_y y ε_z , donde la razón de Poisson es $\nu = \left| \frac{\varepsilon_y}{\varepsilon_x} \right| = \left| \frac{\varepsilon_z}{\varepsilon_x} \right|$ (ej.: Turcotte & Schubert, 2014; Watts, 2001).



Una de las principales razones de estudiar el comportamiento elástico de la litosfera, es determinar el estado de esfuerzos y la distribución de los esfuerzos en la litosfera, lo cual permite investigar fenómenos naturales como los terremotos y erupciones volcánicas (Turcotte & Schubert, 2014).

El estado de esfuerzo más simple es el *estado de esfuerzo uniaxial* y según la ley de Hooke es (Turcotte & Schubert, 2014):

$$\sigma_1 = E \varepsilon_1 \quad (\text{Ec. 1.7})$$

1.5.3 Estado de esfuerzo plano o biaxial

Un estado de esfuerzo plano o biaxial existe cuando solo una de las componentes principales es cero; esto es $\sigma_3 = 0$, $\sigma_2 \neq 0$ y $\sigma_1 \neq 0$ (Turcotte & Schubert, 2014).

A partir de las ecuaciones Ec.(1.4-1.6) y en estado de esfuerzo plano o biaxial, las deformaciones principales se reducen a (ej., Turcotte & Schubert, 2014; Watts, 2001):

$$\varepsilon_1 = \frac{1}{E} \sigma_1 - \frac{\nu}{E} \sigma_2 \quad (\text{Ec.1.8})$$

$$\varepsilon_2 = -\frac{\nu}{E} \sigma_1 + \frac{1}{E} \sigma_2 \quad (\text{Ec.1.9})$$

$$\varepsilon_3 = -\frac{\nu}{E} \sigma_1 - \frac{\nu}{E} \sigma_2 \quad (\text{Ec.1.10})$$

1.5.4 Flexura de placas delgadas: Comportamiento General

La litosfera puede ser interpretada como una placa delgada y elástica flotando sobre un fluido no viscoso (Turcotte & Schubert, 2014) y la deformación de esta, en varias aplicaciones, puede ser aproximada como un mecanismo de flexura (Turcotte & Schubert, 2014). Ejemplos de ellos incluyen la flexura de la litosfera oceánica en zonas de subducción, flexuras ocasionadas por la carga de cuencas sedimentarias, flexuras por carga de edificios volcánicos, flexuras por cargas glaciares y lagos (Turcotte & Schubert, 2014).

El caso de flexura de placas delgadas (Watts, 2001), es un caso particular de estado de esfuerzo plano y es bidimensional (Turcotte & Schubert, 2014). El esfuerzo principal σ_1 es desarrollado por la flexura en el eje-x (horizontal) y σ_2 es el esfuerzo principal en el eje-y (horizontal) actuando para prevenir la deformación en esa dirección ($\varepsilon_2 = 0$). Debido a la condición bidimensional en flexura de placas delgadas, las relaciones de esfuerzos y deformaciones se reducen a las ecuaciones Ec.(1.8-1.9).

Considerando que no existe deformación de la placa en el eje-y horizontal ($\varepsilon_2 = 0$), la ecuación Ec.(1.9) es simplificada:

$$\sigma_2 = \nu \sigma_1 \quad (\text{Ec.1.11})$$

Reemplazando Ec.(1.11) en Ec.(1.8), se obtienen los esfuerzos desarrollados por la deflexión de una placa delgada (Turcotte & Schubert, 2014; Watts, 2001):

$$\sigma_1 = \frac{E}{(1-\nu^2)} \varepsilon_1 \quad (\text{Ec.1.12})$$

$$\sigma_2 = \frac{E\nu}{(1-\nu^2)} \varepsilon_1 \quad (\text{Ec.1.13})$$

La flexión (w) hacia abajo de un “segmento de placa” desarrolla esfuerzos flexurales σ_1 en la dirección horizontal x . Estos se distribuyen dentro de la placa como esfuerzos de compresión en la mitad superior y esfuerzos de extensión en la mitad inferior, sobre y bajo el plano neutral, respectivamente (Figura 1.5). Los esfuerzos y deformaciones son nulos en el plano neutral (Turcotte y Schubert, 2014).

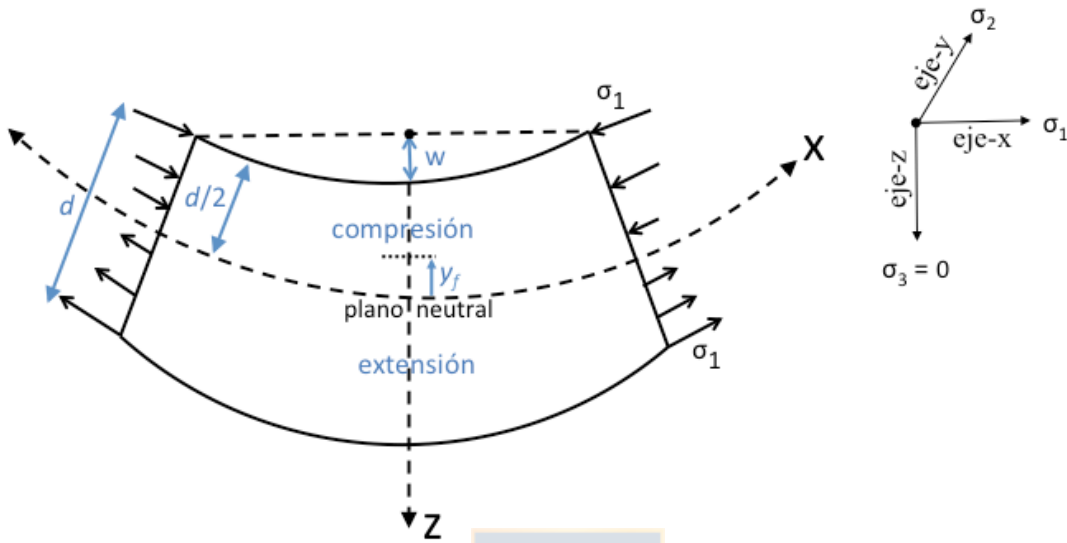


Figura 1.5: Distribución de esfuerzos flexurales en un segmento de placa.

La figura muestra un segmento de placa flexionado hacia abajo. Notar que la curvatura de la placa se representa exagerada, dado que el plano neutral permanece horizontal durante la flexión. w : flexión de la placa; σ_1 : esfuerzo flexural (esfuerzo normal) en el eje-x; d : espesor de la placa; x : plano neutral; z : profundidad en el eje-z vertical; y_f : distancia normal entre el plano neutral y una fibra o plano paralelo al plano xy. Sistema de coordenadas Cartesianas con punto origen centrado en la superficie (ej., Turcotte & Schubert, 2014).

La deformación ϵ_1 en cualquier “fibra” de la placa en la dirección del eje-x, es decir, en cualquier plano paralelo al plano xy es (Watts, 2001):

$$\epsilon_1 = \frac{y_f}{r} \quad (\text{Ec.1.14})$$

donde y_f es la distancia en el eje-z desde el plano neutral hasta una “fibra” de la placa en la dirección del eje-x; y “ r ” es el radio de curvatura de la placa. Considerando que para pequeñas pendientes (Watts, 2001):

$$\frac{1}{r} \approx \frac{d^2w}{dx^2} \quad (\text{Ec.1.15})$$

Reemplazando las Ec.(1.14-1.15) en Ec.(1.12-1.13), los esfuerzos flexurales expresados en función de la flexión de la placa son (Watts, 2001):

$$\sigma_1 = \frac{E}{(1-\nu^2)} \frac{d^2w}{dx^2} y_f = \frac{E}{(1-\nu^2)} \frac{d^2w}{dx^2} \left(\frac{d}{2} - z\right) \quad (\text{Ec.1.16})$$

$$\sigma_2 = \frac{Ev}{(1-\nu^2)} \frac{d^2w}{dx^2} y_f = \frac{Ev}{(1-\nu^2)} \frac{d^2w}{dx^2} \left(\frac{d}{2} - z\right) \quad (\text{Ec.1.17})$$

donde z es la profundidad (positiva vertical hacia abajo), con $z=0$ en la superficie de la placa y $z=d$ en la base de la placa.

La ecuación general de flexión de una placa elástica delgada es una diferencial de cuarto-orden y en coordenadas Cartesianas, con el eje-z vertical y positivo hacia abajo, se escribe (Ugural, 1981):

$$\frac{\partial^4 w}{\partial x^4} + 2 \frac{\partial^4 w}{\partial x^2 \partial y^2} + \frac{\partial^4 w}{\partial y^4} = \frac{p}{D} \quad (\text{Ec.1.18})$$

y escrita en una manera abreviada es (Ugural, 1981):

$$\nabla^4 w = \frac{p}{D} \quad (\text{Ec.1.19})$$



donde $\nabla^4 = \nabla^2 \nabla^2$, ∇^2 es el operador de Laplace, p es una carga-distribuida normal a la superficie de la placa elástica delgada y D es la rigidez flexural de la placa (Turcotte & Schubert, 2014; Watts, 2001):

$$D = \frac{Ed^3}{12(1-\nu^2)} \quad (\text{Ec.1.20})$$

En la Ec.(1.18) los términos $\frac{\partial^4 w}{\partial x^4}$, $2 \frac{\partial^4 w}{\partial x^2 \partial y^2}$ y $\frac{\partial^4 w}{\partial y^4}$ representan la flexión de la placa paralela a los planos xz , xy e yz respectivamente (Ugural, 1981). En general, los textos de geodinámica simplifican el estudio de la flexura de la litosfera debido a cargas superficiales a solo la flexión paralela al plano xz . Luego, la *ecuación general de flexión de una placa elástica delgada* debido a una *carga-distribuida normal* a la superficie de la placa es reducida a (ej., Turcotte & Schubert, 2014; Watts, 2001):

$$\frac{\partial^4 w}{\partial x^4} = \frac{p}{D} \quad (\text{Ec.1.21})$$

**CAPÍTULO II: UPPER CRUSTAL DECOMPRESSION DUE TO DEGLACIATION-
INDUCED FLEXURAL UNBENDING AND ITS ROLE ON POSTGLACIAL VOLCANISM
AT THE SOUTHERN ANDES**

David Mora¹ and Andrés Tassara²

¹ Programa de Doctorado en Ciencias Geológicas, Facultad de Ciencias Químicas, Universidad de Concepción, Barrio Universitario s/n, Concepción, Chile.

² Departamento Ciencias de La Tierra, Facultad de Ciencias Químicas, Universidad de Concepción, Barrio Universitario s/n, Concepción, Chile.

Mora, D., & Tassara, A., 2019. Upper crustal decompression due to deglaciation-induced flexural unbending and its role on postglacial volcanism at the Southern Andes. *Geophys. J. Int.*, 216, 1549-1559, <https://doi.org/10.1093/gji/ggy473>



2.1 Abstract

We implement an analytical model based on flexural deflection of a thin elastic disc to investigate the magnitude of lithospheric decompression caused by deglaciation at upper crustal magmatic reservoirs. Considering a published numerical climate model describing the space-time evolution of deglaciation after the Last Glacial Maximum (LGM) along the Southern Volcanic Zone (SVZ) of the Andes, we demonstrate that changes in pressure at upper crustal levels (< 10 km depth) at the scale of several hundred years are of the order of 10-100 MPa. Total decompression and decompression rate (300-150 kPa/yr) are 1-2 orders of magnitude larger than values previously estimated by other authors who assume that glacial loads are supported by an elastic half space, i.e. of infinite elastic thickness. The large decompression caused by flexural unbending of an elastic plate of finite thickness as assumed here can easily surpass the tensile strength of rocks (5-20 MPa), creating adequate conditions for failure of the reservoir walls, dike propagation inside and outside the reservoir and the eventual collapse of the reservoir accompanying an explosive eruption. We apply our results to the analysis of post-glacial eruptions of SVZ volcanoes, which erupted large volumes (>10 km³) of mafic ignimbrites hundreds to one thousand years after deglaciation onset. We show that this time lag is necessary to achieve a decompression of several tens of megapascals at depths of several kilometers that are consistent with the location of magmatic reservoirs as estimated by independent petrologic, seismic and/or geodetic studies. Moreover the northward increase of this time lag is in agreement with a smaller size of the Andean ice cap in the north than in the south during the LGM. For wet, volatile-rich magmas typical of subduction zones, the effect of large decompression at upper crustal reservoirs caused by flexural unbending of the lithosphere after deglaciation could play a major role in promoting large explosive eruptions through devolatilization of the magma, during past deglaciation events as demonstrated here for the LGM along the SVZ and current accelerated ice retreat caused by climate change over large segments of subduction-related arcs at higher latitudes.

2.2 Introduction

Magmatic reservoirs underneath active volcanoes can be affected by a range of external processes that modify the regional stress field and may trigger an eruption (e.g. Albino et al., 2010; Cañón-Tapia, 2013; Jellinek et al., 2004; Kutterolf et al., 2013; Manga & Brodsky, 2006; Mauk & Johnston, 1973; Pinel et al., 2007; Pinel et al., 2009; Pritchard et al., 2013; Sigmundsson et al., 2013; Sigmundsson et

al., 2010; Violette et al., 2001). Among these processes, melting ice caps on top of volcanoes during deglaciations seems to exert a significant effect on magmatic plumbing systems as suggested by the large number of eruptions globally observed after late Quaternary glaciations (e.g. Brown et al., 2014; Huybers & Langmuir, 2009; MacLennan et al., 2002; McGuire, 2010; Tuffen, 2010; Watt et al., 2013). Post-glacial eruptions were common along large segments of volcanic arcs above high-latitude subduction zones (Cascadia, Alaska-Alutians, Kamchatka-Kuril, Southern Andes, Antarctic Peninsula) that were covered during the Last Glacial Maximum (LGM; approx. 30-15 ky BP) by thick sheets of ice (Fig. 2.1A). Given the accelerated retreat of glaciers caused by recent climate change over the last hundred years, it is fundamental to understand the physical link between deglaciation and eruptions in order to evaluate a potential increase of the number and size of volcanic eruptions in the near future for deglaciating volcanic areas.



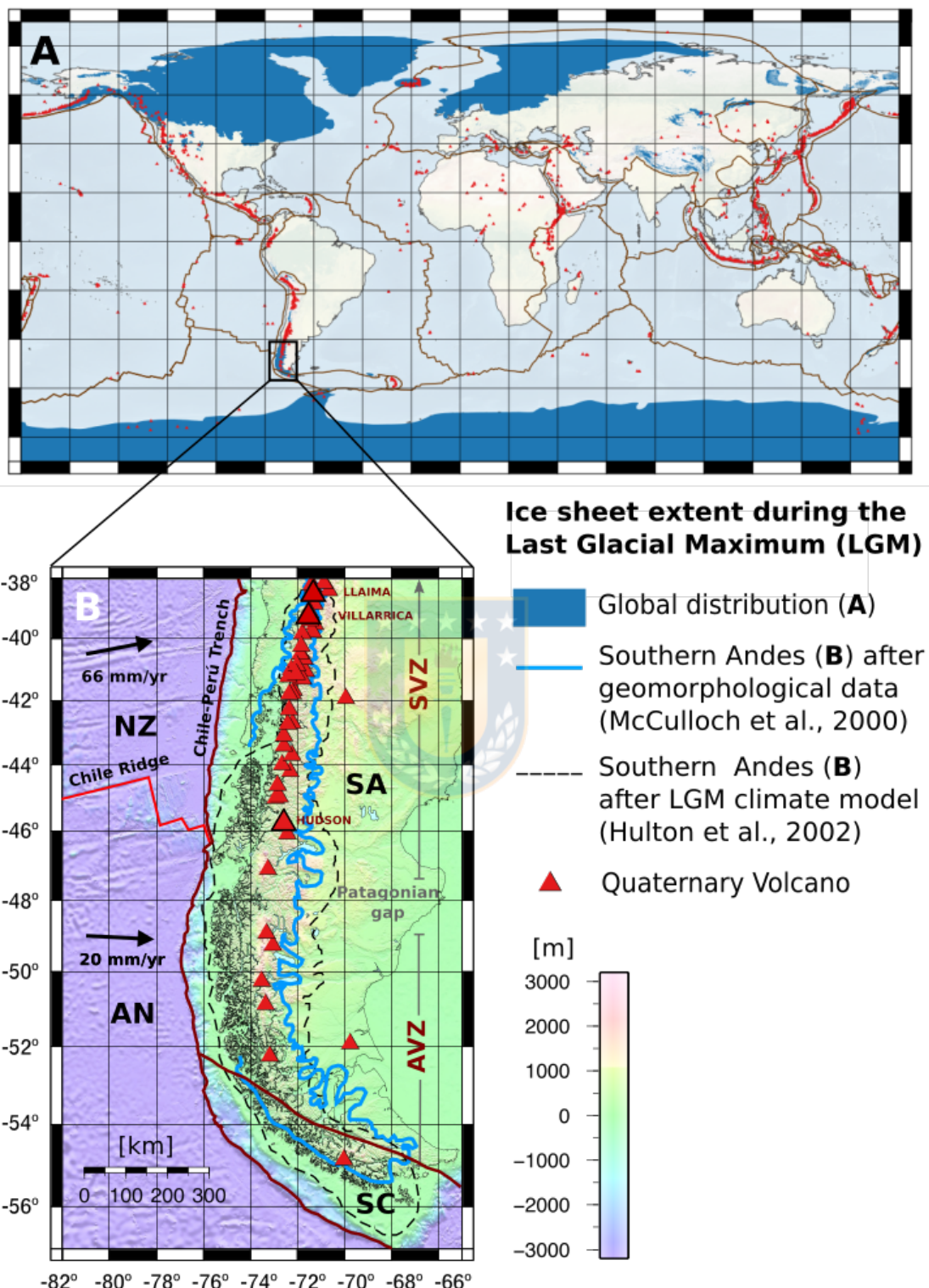


Figure 2.1: Extent of ice cover during the Last Glacial Maximum (LGM) and distribution of Quaternary volcanoes at global scale (A) and for the Southern Andes (B).

For the latter case the figure shows the tectonic plate situation (NZ: Nazca plate, AN: Antarctic plate, SC: Scotia plate, SA: South American plate) with convergence velocity vectors for NZ-SA and AN-SA, the extent of the Southern Volcanic Zone (SVZ) and Austral Volcanic Zone (AVZ) of the Andean cordillera and location of active volcanoes noting those mentioned in the text (Llaima, Villarrica and Hudson).

Most of the models that have been developed to investigate the relationship between deglaciation and volcanism were inspired in Iceland, where both phenomena appear to be clearly connected in space and time (e.g. Eason et al., 2015; Hardarson & Fitton, 1991; Jull & McKenzie, 1996; Maclennan et al., 2002; Pagli & Sigmundsson, 2008; Sigmundsson, 2006; Sigvaldasson et al., 2002). These models were mainly devoted to evaluate the effect that the removal of an axisymmetric ice sheet from a sub-aerial spreading ridge could exert on magma productivity via decompression melting of the sub-lithospheric mantle, accounting for the influence of both a nonhydrostatic stress field and viscous flow (Jull & McKenzie, 1996). Most of the assumptions behind these models are valid for the very particular case of Iceland (subaerial volcanism above a hotspot-ridge interaction). Other models have been developed to analyze deglaciation-induced changes of pressure at upper crustal levels that can influence the formation of dikes feeding volcanic eruptions by reducing the confining lithostatic stress (e.g. Albino et al., 2010; Jellinek et al., 2004; Rawson et al., 2016; Sammis & Julian, 1987). Particularly, Sigmundsson (2006) and Sigmundsson et al. (2010) consider glacial loads as supported by the rigidity of a elastic half-space (i.e. a elastic media of infinite thickness) to investigate the effect of deglaciation on pressure below volcanic systems in Iceland. This model suggests that deglaciation-induced decompression at upper crustal levels can reach values of 1-10 MPa, which are in the range of the tensile strength of rocks (5-20 MPa; Tait et al., 1989; Pinel & Jaupart, 2003). Thus, glacial unloading can modify the failure conditions of magma chambers in a manner that depends critically on ice retreat, the shape and depth of magma chambers as well as the compressibility of the magma (Sigmundsson et al., 2010).

Previous studies have not considered the direct effect that flexural unbending of the lithosphere during glacial unloading could have on stresses around shallow magma reservoirs. Vertical loads imposed by growing glaciers at the Earth surface are primarily supported by the downward deflection of a thin elastic lithosphere (e.g. Turcotte & Schubert, 2014; Walcott, 1970), i.e. a elastic plate of small thickness compared to its lateral dimensions, in contrast to an infinite elastic half-space. At magmatically active regions, this process can trap magmas in upper crustal reservoirs because they are supporting horizontal compression imposed by flexure. The upward elastic rebound of the lithosphere

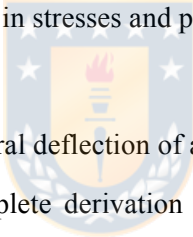
after deglaciation can revert the stress field causing large decompression of the upper crust surrounding the magma chamber. If this decompression is transferred inside the reservoir, it can potentially activates the exsolution of volatiles from the magma, which would strongly increases the stress supported by the crust surrounding the reservoir and could create favorable conditions for an explosive, caldera-forming eruption (e.g. Alidibirov & Dingwell, 1996; Gardner et al., 1999; Mangan & Sisson, 2000). Furthermore, upper crustal decompression can also drive dike propagation from deeper levels and the consequent replenishment of shallow magma reservoirs as a possible trigger of an eruption (Jellinek et al., 2004; Rawson et al., 2016; Rubin, 1995).

The link between deglaciation and post-glacial eruptive activity is nicely illustrated by the case of the Southern Volcanic Zone (SVZ) of the Andes, which has been cited as a key locality to study this relationship at subduction arcs (Fontijn et al., 2014; Rawson et al., 2015; Watt et al., 2013; Weller et al., 2014). The ice cap associated with the LGM was 1.5-2.5 km thick and covered the entire Andean cordillera south of 37°S (Fig. 2.1B). The initial warming step occurred at ~17.500-17.200 calibrated years BP (Kaplan et al., 2004; McCulloch et al., 2000; Watt et al., 2013), it was synchronous along the arc and melted almost all the ice cap northward of 42°S in less than 2000 years (Hulton et al., 2002; McCulloch et al., 2000). Within this same period, large tephra volumes ($\sim 10 \text{ km}^3$) were expulsed by explosive ignimbritic eruptions at Llaima, Villarrica and Hudson volcanoes (e.g. Watt et al., 2013; Weller et al., 2014).

In order to evaluate the influence that flexural unbending induced by deglaciation could have on decompressing the crust around shallow magma chambers, we use an analytical solution of flexure for a thin elastic disk with simply supported edges (Ugural, 1981) to develop a general formulation for temporal changes in pressure below the center of an ice disk during deglaciation. Under the spatio-temporal constraint of southern Andean deglaciation given by the numerical climate model of Hulton et al. (2002), we apply our tool to analyze temporal variations on stresses and pressure at upper crustal levels underneath a glaciated volcanic region. Our results demonstrate that, despite uncertainties on elastic parameters (elastic thickness and Poisson ratio) and actual magnitudes of the ice sheet at the LGM along the Andes, deglaciation produces an upper crustal decompression of the order of tens to hundreds of megapascals at time-scales of hundred of years, high enough to surpass the tensile strength of upper crustal rocks and in general agreement with the time lag between LGM and explosive eruption along the SVZ.

2.3 Analytical approximation and method

The geological situation of a rigid upper crustal layer being deflected by the weight of an ice sheet can be represented by vertically loading a thin elastic plate overlying an inviscid fluid. For an elastic, homogeneous, linear and isotropic body under plane stress, the downward deflection of the loaded plate responds to the balance between the loading force and the flexural rigidity of the plate, which is described by a general 4th order differential equation (Turcotte & Schubert, 2014; Watts, 2001). We take advantage of an analytical solution of this equation developed by Ugural (1981) for the case of a cylindrical thin elastic plate loaded at the upper surface by a homogenously distributed force and with simply supported edges at its base. A version of Ugural's solution was used by Gudmundsson (1999) to analyze the role that postglacial doming (upward deflection) in Fennoscandia could have on upper crustal stresses and further formation of fractures. For this application, Gudmundsson (1999) used direct measurements of Holocene uplift to compute stresses with independency of the unknown load acting at the base of a thin elastic disk. We are interested on a different problem where the downward deflection of the lithosphere is unknown but one can put constraints on the space-temporal evolution of glacial loads in order to estimate changes in stresses and pressure.



2.3.1 Derivation of the equation for flexural deflection of a thin elastic disk loaded at its surface

We present in the appendix (A) a complete derivation of the equations governing this problem as exposed by Ugural (1981) and expanded by us. Here we describe the general context of this approach and the main equation (Eq. 2.1) resulting after this derivation. In plane stress and a cylindrical coordinate system coaxial with the plate and the load as in figure 2.2, pressure P along the vertical axis of symmetry (z -axis) is equal to the radial stress σ_r and is defined as:

$$P(z, t) = \sigma_r(z, t) = \frac{(3+\nu)^3}{4} \rho g h(t) \frac{R(t)^2}{d^3} \left(\frac{d}{2} - z \right) \quad (\text{Eq. 2.1})$$

Here, the geometry of the load is described by a cylindrical ice cap with thickness $h(t)$ and radius $R(t)$ that are allowed to change with time t , ρ is density of ice (900 kg/m³), g acceleration of gravity (9.8 m/s²), d is the thickness of the thin elastic plate (i.e. the elastic thickness) and ν is Poisson's ratio. The boundary condition of simply supported edges of the thin elastic disk is implemented here assuming that this edge coincides with the horizontal limits of the circular ice sheet loading the plate, so the radius R defines the horizontal dimensions of both the load and the elastic disk itself, and decreases

with time as the deglaciation advances. The weight of the cylindrical ice cap is regionally compensated by the downward deflection of the plate, in contrast to a local compensation by the rigidity of an elastic media of infinite thickness as for the half-space approximation. Therefore, the flexural deflection of the plate creates large horizontal stresses above (compressional) and below (tensional) its middle (neutral) plane at $z=d/2$. In our coordinate system, z is zero on the surface and increases positively downward. We use a convention of signs where compressive stresses are positive and tensional stresses are negative.

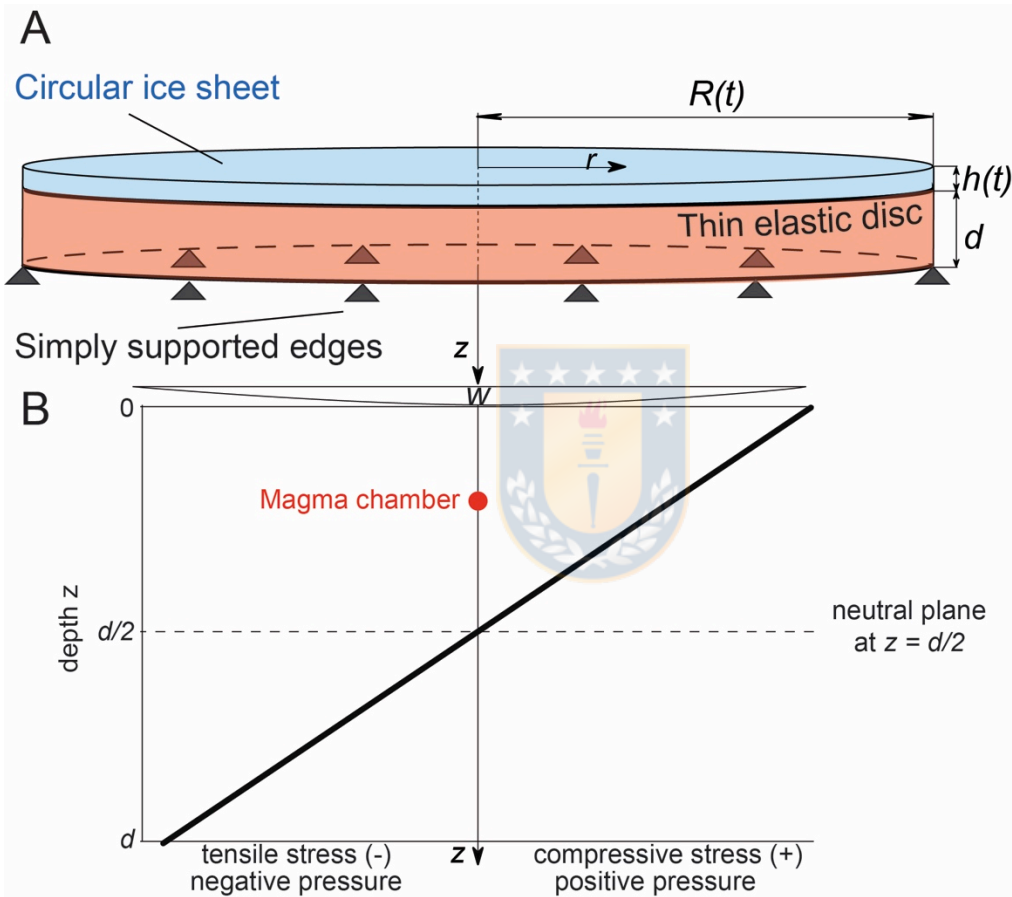


Figure 2.2: Basics of the physical model for flexure of a thin elastic disk loaded by the weight of an ice sheet.

A) A cylindrical coordinate system is used, and the axis-symmetry of the problem means that only the vertical (z) and radial (r) coordinates are relevant. The ice sheet load is defined by the radius $R(t)$ and thickness $h(t)$ of the a cylindrical ice cap that can change with time t . This load generates a downward deflection (w in B) of a thin elastic disk of finite thickness d . The edges of the disk coincide with those of the ice sheet and are supported at it base by simple foundations. B) Vertical stress and pressure profile downward along the z -axis of symmetry underneath the center of the ice sheet and elastic disk. Stresses are compressive/tensile and pressure is

positive/negative respectively above/below the neutral plane of the elastic disk at $z=d/2$. We are interested on temporal changes on pressure that occur in a point representing the position of an upper crustal magma chamber.

2.3.2 Limitations of the model

The thin plate approximation is valid for sufficiently large ice sheets compared with the thickness of the plate, namely for $2R>5d$. For common values of elastic thickness in volcanic arcs (10-20 km; Pérez-Gussinyé et al., 2008; Tassara et al., 2007), our approach could be safely applied as far as the diameter of the ice sheet remains larger than 50-100 km. This is nearly half of the east-west width that Patagonian glaciers reached at the northern extreme of the ice sheet during the LGM (Fig. 2.1).

In our model, the magmatic chamber is idealized as a point located in the upper crust right underneath the center of the ice sheet, above the neutral plane of the elastic disk (Fig. 2.2). We do not consider any particular feature of the chamber (rheology, magma compressibility, volume or shape) that could certainly influence the transmission inside the chamber of stresses from the wall rock affected by pressure changes due to deglaciation-induced flexural decompression. We consider the cylindrical thin elastic plate model with a coaxial radial disk representing the ice cap as a sufficient approximation of the situation underneath a radially glaciated volcano. Our simple model does not consider topographic variations, ignoring also isostatic buoyancy forces as partly supporting surface loads; this can be justified because of the small density contrast that can be expected between upper and middle crust at a continental active margin as the Southern Andes. As in our approach the thin elastic disk overlays an inviscid fluid (i.e. viscosity=0), any viscous response of mid-lower crust and mantle is also neglected by the model, which is more difficult to justify mostly considering that we are interested in the time variation of pressure during deglaciation. The time-scale of the viscous response increases with increasing viscosity and for values of 10^{19} - 10^{20} Pa*s (as expected below the Patagonian Andes; Ivins & James, 1999) can be of the order of several thousand years (Jellinek et al., 2004; Turcotte & Schubert, 2014), i.e. larger than the range of several hundred to some thousand years over which Southern Andean deglaciation took place. We consider our approach as representing the first order elastic (static) response of the system, and let the time evolution be defined by the history of deglaciation, i.e. the form of $h(t)$ and $R(t)$ in equation 2.1.

2.3.3 Comparison against the elastic half-space model

As mentioned before, estimates of pressure changes at upper crustal levels caused by retreating glaciers above volcanic areas have been previously made by considering that glacial loads are supported by the

rigidity of an elastic half-space. Particularly, Sigmundsson (2006) and Sigmundsson et al. (2010) proposed the following expression for the pressure profile below an axis-symmetric and circular ice sheet in cylindrical coordinates:

$$P(z) = \frac{(1+\nu)^2}{3} \rho g h \left(1 - \frac{z}{\sqrt{R^2+z^2}}\right) \quad (\text{Eq. 2.2})$$

Note that equation 2.2 has a similar form compared to equation 2.1, which derives from a similar conceptualization of the problem. The main difference is the role of the ice sheet radius R ; for both models the pressure P is directly proportional to R , but for the thin elastic disk approximation this proportionality is given by R^2 whereas for the elastic half-space is by $(1-1/R)$. This means that for the same dimensions of the ice sheet, the pressure induced at upper crustal levels inside the finite-thickness elastic disk is much larger than in the case of an elastic half-space of infinite thickness. The amount of this depends on the relation between the radius R and elastic thickness d of the plate. With d tending to infinite, i.e. approaching the half-space and violating the thin plate approximation, equation 2.1 shows that pressure at any depth tends to zero. Let us consider a point at depth $z=R/20$. At this shallow depth compared with the horizontal extent of the ice sheet, and considering $\nu=0.5$, pressure computed with equation 2.2 approaches the weight of the ice column, i.e. $P = \rho g h \approx 15$ MPa. At the same depth, equation 2.1 could generate a similar pressure only if the thickness of the elastic disk is similar to the radius of the ice sheet, i.e. violating the thin plate approximation. If this approximation is respected by considering that $5d=R$, then pressure at depth $z=R/20$ is 16 times larger than $\rho g h$, i.e. of the order of 240 MPa. For smaller values of z and d with respect to R this effect is amplified. This exercise illustrates the fundamental difference that supposes distributing the load of a surface load inside an infinite elastic media compared to concentrating the support of this load in a plate of finite thickness, which therefore can develop much larger stresses.

2.3.4 Incorporating the temporal evolution of deglaciation for the Southern Andes

The implementation of our approach requires knowledge about the history of glacial retreat in order to define the form of the temporal variation of the load as expressed in $h(t)$ and $R(t)$. In the case of the Southern Andes, this history can be described by the numerical climate model of Hulton et al. (2002). We define the deglaciation factor $Q(t)$ as the ratio between $V(t)$, the remaining ice volume at time t and the initial ice volume V_0 . For the numerical definition of the volume variation with time, we assume $V(t)=At^{-n}$, with A and n constants that we obtained from curve fit of the glacial history as extracted

directly from figure 3 of Hulton et al., 2002). We impose that the temporal variation of Q as defined by Hulton et al. (2002) for the whole southern Andean glacier can be used to describe the history of deglaciation at any glaciated area within it.

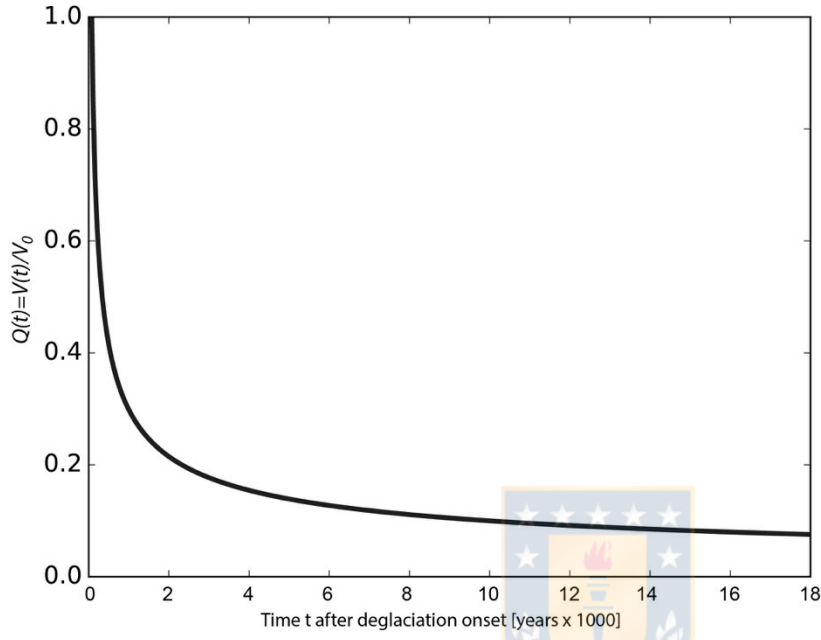


Figure 2.3: Evolution of Deglaciation Factor $Q(t)$.

Defined as the ratio between remaining volume of the ice sheet $V(t)$ at time t after deglaciation onset and the initial glacial volume V_0 , following the numerical climate model of Hulton et al. (2002) for the Patagonian Ice Sheet after the Last Glacial Maximum (LGM)

As shown in Fig. 2.3, the Patagonian deglaciation over the last 18 ka is characterized by this numerical model as an exponentially continuous decrease of ice volume that melted ca. 80% of initial glacial volume during the first 2000 years with a more gradual and slow ice retreat later on.

We further assume that the scaling relation between thickness h_0 and radius R_0 of the cylindrical ice cap at $t=0$ (deglaciation onset) remains constant with time, i.e. $\frac{R_0}{h_0} = \frac{R(t)}{h(t)}$. Considering this along with the definition of $Q(t)$ and the formulae for the volume of a cylinder ($V=h\pi R^2$), it holds that:

$$h(t) = h_0 Q(t)^{\frac{1}{3}} ; \quad R(t) = R_0 Q(t)^{\frac{1}{3}} \quad (\text{Eq. 2.3})$$

Replacing $h(t)$ and $R(t)$ from eq. 2.3 into eq. 2.1, it is possible to fully describe $P(z,t)$ and compute the temporal variation of pressure with depth below a Southern Andean volcano.

2.4 Application to the Southern Andes

We perform a first exercise (Fig. 2.4) to compute $P(z)$ at $t=0$, i.e. right before the beginning of deglaciation. For this, we choose values for $h_0=1500$ m, $R_0=100$ km being consistent with the climate model of Hulton et al. (2002) during the LGM at 42°S in the SVZ.

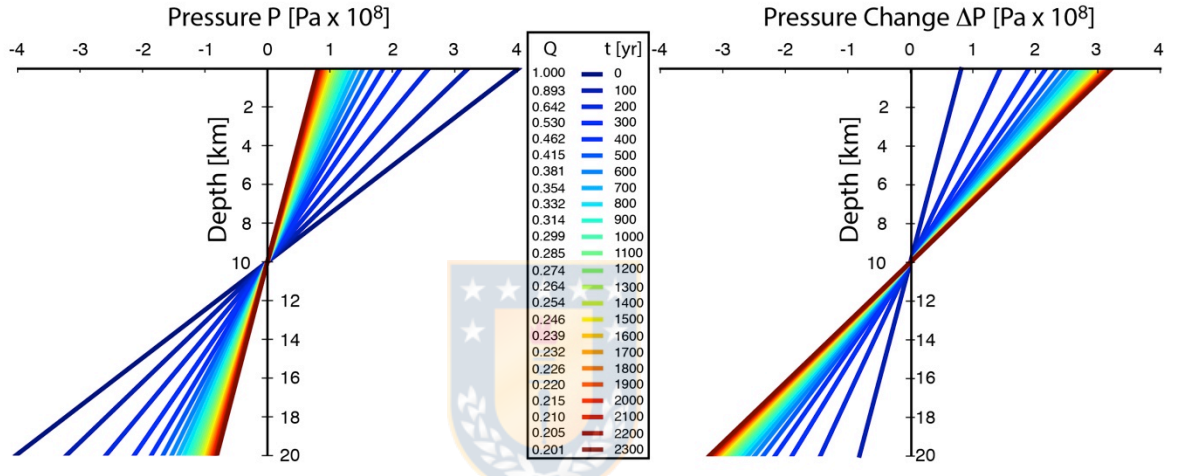


Figure 2.4: Depth profile of pressure P (left) and pressure change ΔP (right).

Computed every 100 years after deglaciation onset ($t=0$, $Q=1$) following the deglaciation history of the Southern Andes described in Fig. 3. For this example the elastic thickness $d=20$ km and dimensions of the initial ice sheet are given by $h_0=1500$ m and $R_0=100$ km .

Elastic parameters are imposed as $\nu=0.25$ (Turcotte & Schubert, 2014) and $d=20$ km (as an average for the Southern Andes after Tassara et al., 2007). Pressure is increasingly positive (compressive) and negative (tensional) respectively above and below the middle neutral plane (at $d/2=10$ km depth in this example) of the thin elastic plate, reaching maximum values of 400 MPa at the surface. Fig. 2.4 also shows how this pressure profile and consequent decompression values (pressure changes) evolve with time after deglaciation onset, with decreasing pressure (increasing pressure change) at a given depth due to the upward unbending of the upper crustal plate for decreasing volumes of the ice cap.

We argue that the gradual depressurization of the upper crust above the neutral plane can be, at least partially, responsible for creating particular physical conditions around shallow magmatic reservoirs that could help preparing a large postglacial eruption. Thus, our general goal is to evaluate under which settings a decompression ΔP in the range of tens of MPa, which is estimated sufficient to enable dike propagation (e.g. Rawson et al., 2015; Sigmundsson et al., 2010) and to trigger ignimbritic eruptions (e.g. Lohmar et al., 2012), can be achieved within a time lag of ca. 500-1000 yrs between the onset of deglaciation and large post-glacial eruption in the SVZ. For this, we compute the depth $Z_{\Delta P}$ at which a given pressure change ΔP is verified at a certain time t after deglaciation onset, for a set of parameters defining the initial glacial cap (h_0 and R_0) and the elastic response of the crust (v and d). Considering ΔP as the change in pressure between the initial stage at deglaciation onset and the stage at time t as defined by equations 2.1 and 2.3, it can be shown that:

$$Z_{\Delta P}(t) = \frac{d}{2} - \frac{4d^3 \Delta P}{3\rho g h_0 (3+v) R_0^2 (1-Q(t))} \quad (\text{Eq. 2.4})$$

For the same dimensions of the glacial cap at deglaciation onset as in fig. 2.4, we show in figure 2.5 an example for a range of ΔP and varying elastic properties. For $\Delta P=30$ MPa and $d=20$ km (as in fig. 2.4), it can be observed that $Z_{30\text{MPa}}=0$ km when $Q(t)=0.93$ (ca. 100 years after deglaciation onset), it rapidly increases to 7-8 km until $Q(t)=0.75$ (160 years after deglaciation onset) and then shows a more gradual increment to near 9 km at present times. This general behavior of $Z_{\Delta P}$ with time is observed for the whole range of elastic thickness d (5-40 km), but the actual form of the curve varies with d . The thinner the plate, the earliest occur ΔP at the surface and the faster is the decrease of $Z_{\Delta P}$ to an asymptotic plateau toward the neutral plane of the plate. For sufficiently large d (40 km in fig. 2.5) this transition does not yet occur into the time lapse between deglaciation onset and the present day. Compared with the large effect of elastic thickness, variations in Poisson's ratio v between the range for crustal materials (0.15-0.33) has a negligible effect on $Z_{\Delta P}$.

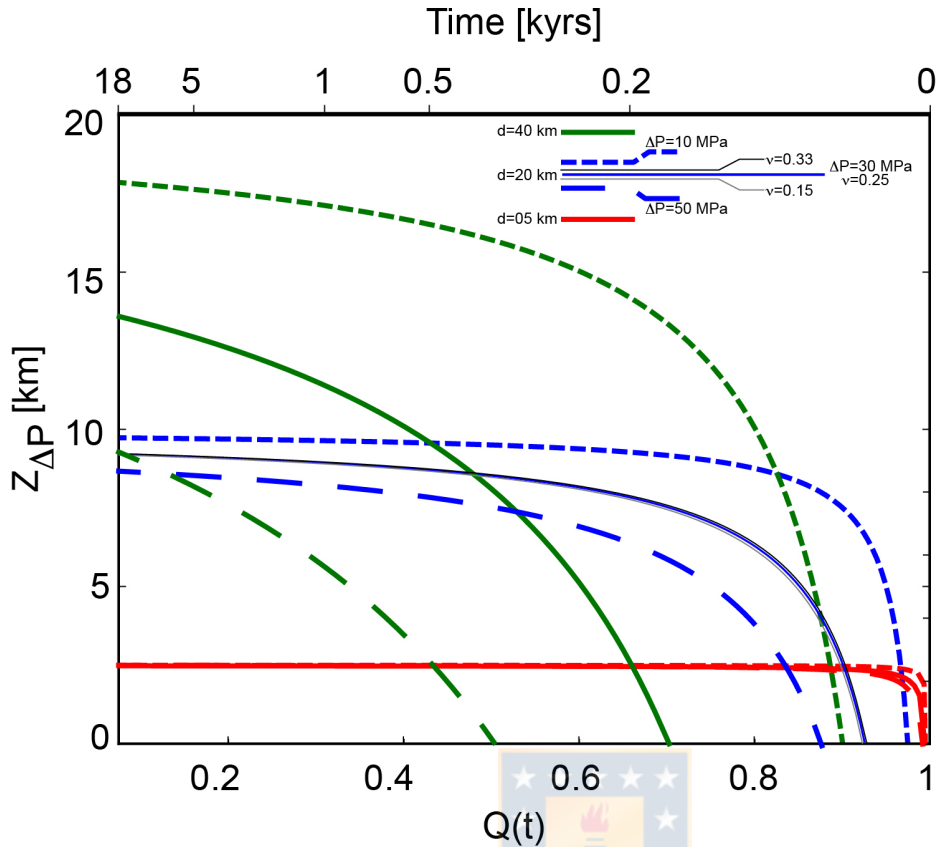


Figure 2.5: Depth $Z_{\Delta P}$ at which a certain decompression ΔP occur as a function of the deglaciation factor $Q(t)$ (or time in thousand of years after deglaciation onset) for a range of ΔP , elastic thickness d and Poisson's ratio ν .

Fig. 2.5 also shows how $Z_{\Delta P}$ varies for different values of ΔP . Relatively small changes in pressure are achieved earlier after deglaciation onset and the transition to the plateau-like behavior toward the neutral plane does occur faster than for large depressurizations. At a given depth it can be seen that depressurization is increasingly large for longer time after deglaciation onset, although the specific time needed to increase ΔP positively scales with d . This is because in our formulation, d controls the way by which temporal variations of the ice load translates into changes of pressure.

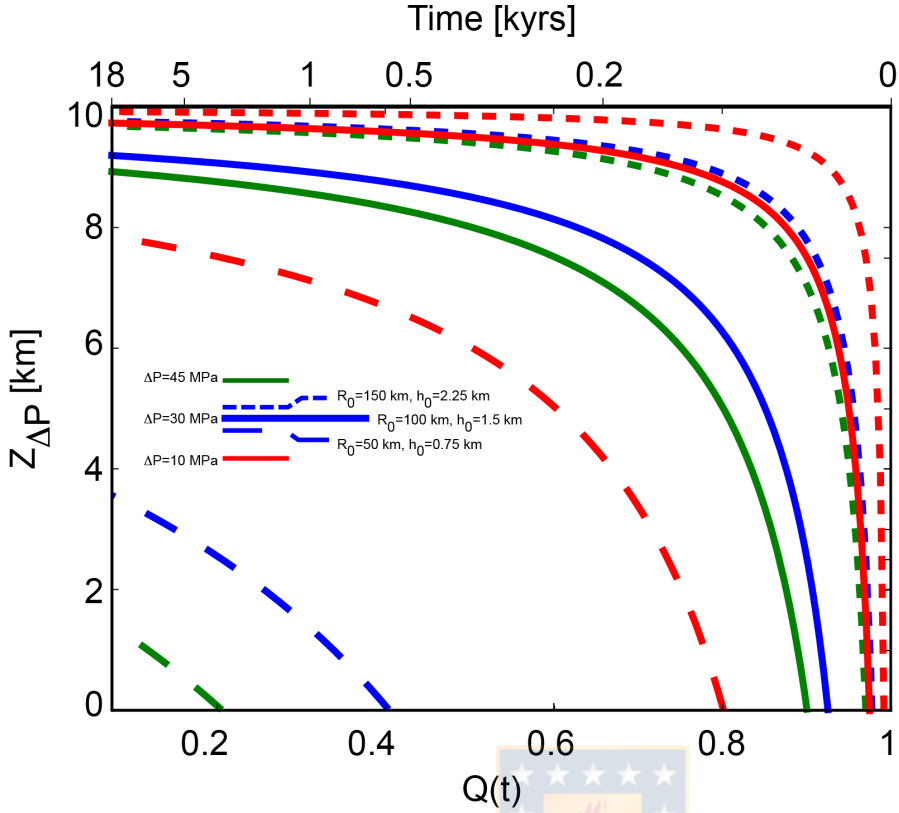


Figure 2.6: Depth $Z_{\Delta P}$ at which a certain decompression ΔP occur as a function of the deglaciation factor $Q(t)=V(t)/V_0$, as is Fig. 2.5 but analyzing the effect of changing geometry of glacier cap thickness and radio at deglaciation onset h_0 and R_0 .

We separately analyzed the effect of the initial size of the glacier in fig. 2.6. Variations in the dimensions of the ice sheet before deglaciation onset as expected along the Southern Andes after the LGM has a large impact on possible upper crustal decompression. For values of h_0 and R_0 half of those assumed for figs. 2.4 and 2.5, a decompression $\Delta P=30$ MPa is achieved at the surface only after ca. 500 years of deglaciation ($Q=0.4$) and $Z_{\Delta P=30MPa}$ shows a gradual increases to a maximum of ca. 4 km when Q approaches zero. A large $\Delta P \geq 50$ MPa is never reached under this condition, whereas $Z_{\Delta P=10MPa}$ intersects the surface after ca. 20 years ($Q=0.97$) and approaches the neutral plane ($z=10$ km) after 100 years ($Q=0.85$). For small glaciers, a relatively small decompression is expected at shallow upper crustal levels. In contrast, a glacier size 50% larger than assumed in figs. 2.4 and 2.5 is associated with a rapid decompression reaching earlier the neutral plane even for large values of ΔP .

2.5 Discussion

2.5.1 Implications of finite versus infinite thickness of the elastic media on deglaciation-induced decompression

Previous studies about the potential role of glacial unloading above a shallow magma chamber have concluded that the effect of deglaciation on possible failure of the reservoir walls is minimal (Andrew & Gudmundsson, 2007; Sigmundsson et al., 2010), and can be decisive only if the magma batch is close to rupture conditions (Sulpizio et al., 2017). This conclusion is based on maximum estimated decompression values of some megapascals after several hundred years of deglaciation (Rawson et al., 2016; Sigmundsson et al., 2010; Sulpizio et al., 2017). These are at the lower range of values for the tensile strength of rocks (e.g. Turcotte & Schubert, 2014) that must be surpassed in order to initiate dike propagation and/or reservoir collapse.

This small deglaciation-induced upper crustal decompression results from assuming that glacial loads are entirely supported by the rigidity of an elastic half-space, i.e. an elastic body of infinite elastic thickness. Considering, as here, an elastic plate of finite thickness in the range of tens of kilometers as expected above subduction zones (Audet & Bürgmann, 2011; Tassara et al., 2007), largely increases the possible value of upper crustal decompression due to the unbending of the elastic plate. Let us consider for example a plate of elastic thickness $d = 20$ km and an ice sheet of intermediate dimensions (as for fig. 2.4 and 2.5), in which a volcanic reservoir lies at 5km depth. Under these conditions, our computations indicate a pressure drop of 30 MPa during the first hundred years and a total of 150 MPa decompression after a thousand years of deglaciation. This implies rates of upper crustal decompression of 300-150 kPa/yr. Thus, our estimates for total decompression and decompression rate are 1-2 orders of magnitude larger than those reported by previous authors (Rawson et al., 2016; Sigmundsson et al., 2010; Sulpizio et al., 2017). Such a large decompression surpasses the tensile strength of rocks surrounding a shallow magma chamber, which would increase the possibility of magma chamber failure.

2.5.2 The case of the Southern Andes for understanding the role of postglacial flexural unbending

A more detailed analysis of the southern Andean case can help to discuss the implications of our results. Let us start noting the simultaneous onset of deglaciation after the LGM along the southern Andes in the range 17.5-17.2 ka BP, as informed by Denton et al. (1999) and McCulloch et al. (2000).

Large ignimbritic eruptions ($>10 \text{ km}^3$ erupted volume) have been dated in 16.50-16.02 ka BP at Llaima (Watt et al., 2013), 16.84 – 16.12 ka BP at Villarrica (Lohmar, 2008; Watt et al., 2013) and 17.44-17.20 ka BP at Hudson (Weller et al., 2014). This implies a time lag between deglaciation onset and eruption of 1000-1180 years for Llaima, 660-1080 years for Villarrica and 0-60 years at Hudson. Into the conceptual framework of our model, this time lag should corresponds to the time it takes for an underlying crustal magmatic reservoir to experience a decompression of several tens of MPa (i.e. similar to the tensile strength of rocks), able to promote destabilization of the system and to trigger an explosive eruption.

In this framework, we note that the apparent northward increase of the time lag could be related to specific gradients of one or several parameters considered in our formulation. For instance, a more rapid decompression-induced volcanic response to deglaciation in the south (Hudson volcano) than in the north (Llaima and Villarrica volcanoes) could be related to either a thinner elastic plate (d), a shallower magmatic reservoir (z) or a larger initial ice sheet (R_0 and h_0). This latter factor likely plays a major role, since the east-west width (and arguable also the thickness) of the Patagonian ice sheet during the LGM (as shown in fig. 2.1) was much larger in the south (300 km at Hudson) than in the north (150 km for Villarrica, 100 km for Llaima). A south-to-north increase of the elastic thickness is not observed in published maps of this parameter that show either a roughly constant value of 10-20 km along the axis of the SVZ (Tassara et al., 2007) or even a larger d in the south near Hudson (ca. 30 km) compared to northern segments of the SVZ (Pérez-Gussinyé et al., 2008). A systematic northward increase in the depth of the main magmatic reservoir underneath these volcanoes is also hard to justify, since estimates based on petrological studies of past and recent erupted products as well as the interpretation of seismic and geodetic data show a large range of values for each volcano, with 2 to 14 km for Hudson (Delgado et al., 2014; Kratzmann et al., 2009), 1.5 to 8 km for Villarrica (Delgado et al., 2017; Lohmar, 2008), and 2 to 12 km for Llaima (Bishop et al., 2017; Bouvet de Maisonneuve et al., 2012; Ruth et al., 2016).

Conversely, we can use our results to provide some constraints on the possible depth range at which the magmatic reservoir below these volcanoes shall be located in order to match each observed time lag. For $d=20 \text{ km}$ and $\Delta P=30 \text{ MPa}$, given the large dimensions of the initial ice cap at Hudson and its very short time lag between deglaciation onset and eruption, fig. 2.6 indicates that the magmatic reservoir could be anywhere between 0 and 9.5 km depth. At the other extreme, a small initial ice sheet

and the specific time lag for Llaima require a shallow magmatic reservoir around 2 km depth, whereas in the intermediate situation of Villarrica the optimal depth range increases to 4-6 km.

2.5.3 Postglacial mafic ignimbrites and the role of upper crustal decompression

A key observation stands in the association of large postglacial eruptions (Llaima, Villarrica and Hudson) with ignimbritic deposits that mostly comprise basaltic to basaltic andesitic compositions (e.g. (Lohmar et al., 2012; Weller et al., 2014). Large mafic ignimbrites are quite rare because water (and other volatiles) has a greater solubility in low-silica magmas compared to acidic melts (e.g. Moore et al., 1998), tending to stay longer in the melt and precluding the creation of overpressure by exsolution of volatiles to a vapor phase. The occurrence of large postglacial mafic ignimbrites in the Southern Andes points to an unusual major exsolution of volatiles in order to allow for enhanced bubble generation and magma fragmentation during explosive eruptions.

For the specific case of Villarrica, we consider the pre-eruptive conditions for the Lican ignimbrite, a basaltic andesitic pyroclastic flow with large amounts of vesicles (up to 53 vol.%) that is mentioned by Lohmar et al. (2012) as evidence of a volatile-saturated melt condition. Based on thermodynamic modeling over mineral-chemical data, these authors estimated that the eruption was accompanied by an increase of ~200°C in melt temperature (from ~900–1000° to ~1100–1150 °C) and a decrease in H₂O content in the melt of ~1.6 wt.% along with a decompression of ~40 MPa (from ~65 to 25 MPa). Their preferred interpretation of these results points to a recharge with hot mafic magma into a shallow reservoir of basaltic andesitic composition and an upward motion of the pre-eruptive melt from 2.5 to 1 km depth after recharge. However, Lohmar et al. (2012) also discuss an alternative interpretation where decompression caused by glacial unloading could be also important in conditioning the eruption. Using the elastic half-space approximation, they estimated 6-10 MPa of deglaciation-induced decompression after removal of 600-1000 m of glacial cap, and calculated 0.4-0.3 wt% decrease in H₂O solubility in the magma using the expression of Moore et al. (1998). Considering decompression values of tens to one hundred MPa as suggested by our results, this would imply a reduction in water solubility of 1-3 wt% below Villarrica. This could be high enough to allow for a devolatization of the melt in the range of values estimated by Lohmar et al. (2012). Our results indicate that such a large exsolution of water from the mafic magma was achieved over a hundred years period before eruption, i.e. a larger time scale than the scale of years to minutes assumed in Villarrica and elsewhere as associated with an eruption triggering caused by a sudden magmatic recharge into the reservoir (Lohmar et al., 2012). However, we argue that the already devolatized nature of the magma in the reservoir with the presence

of an exsolved gas phase was an important condition for allowing an explosive eruption once the recharging magma entered the chamber. In addition, the decompression values estimated by our model can also be responsible for the recharge process itself identified as the main trigger for the Lican ignimbrite at Villarrica, since this decompression is high enough to induce the propagation of dikes from a deep reservoir of hot mafic magma to the shallow chamber from where the pre-eruptive magma was extracted.

2.6 Concluding remarks

More sophisticated numerical models would be necessary to include the potential effect of spatially-varying elastic thickness, isostatic rebound and/or the viscous response of the lower crust and upper mantle in regulating the time evolution of pressure changes and their impact on magmatic plumbing systems. Although these complexities, particularly the role of visco-elastic rheology (e.g. Hampel, 2017; Jellinek et al., 2004), can likely have an impact on the magnitude and temporal evolution of upper crustal decompression caused by deglaciation, we think that our simple elastic model that innovatively use the flexural solution of a thin elastic disk with simply supported edges (Ugural, 1981), is able to capture the first-order behavior of the lithosphere affected by the removal of ice caps. Particularly, our results demonstrate the major contribution of flexural unbending of the elastic upper crust during ice sheets retreat in causing large decompressions (10-100 MPa) of shallow magmatic reservoirs, allowing the propagation of dikes from below to feed the reservoir and/or the degassing of volatile-rich magma, and therefore creating conditions for huge explosive eruptions. We think that such a mechanism likely dominates the interplay between deglaciation and eruptions at subduction zones, where most of the postglacial eruptive activity is related to explosive volcanism of volatile-rich magmas generated by wet melting of the mantle wedge.

At divergent margins like Iceland, magmas created by decompression melting of the mantle are dry and perhaps the role of decompression-induced exsolution of volatiles from the magma is less important in comparison to enhanced melting at the base of the lithosphere and dike propagation (e.g. (Jull & McKenzie, 1996; Sigmundsson et al., 2010). Nevertheless, considering the large segments of volcanic arcs above subduction zones worldwide that were covered by ice sheets during the Holocene, we believe that the mechanism of deglaciation as modeled here is fundamental in explaining the increased rate of volcanic eruptions recorded after the LGM worldwide (e.g. Huybers & Langmuir,

2009; Maclennan et al., 2002; Watt et al., 2013) and to evaluate the effect of climate change on current deglaciation at fast rates along glaciated volcanic arcs at higher latitude subduction zones (Southern Andes, Antarctica, Alaska, Kamchatka, Japan).



**CAPÍTULO III: COMBINING FLEXURAL UNBENDING AND ISOSTATIC ADJUSTMENT
TO UNDERSTAND POSTGLACIAL DECOMPRESSION OF UPPER CRUSTAL
RESERVOIRS AT THE SOUTHERN ANDES**

David Mora¹ and Andrés Tassara²

¹ Programa de Doctorado en Ciencias Geológicas, Facultad de Ciencias Químicas, Universidad de Concepción, Barrio Universitario s/n, Concepción, Chile.

² Departamento Ciencias de La Tierra, Facultad de Ciencias Químicas, Universidad de Concepción, Barrio Universitario s/n, Concepción, Chile.

Trabajo enviado a revista “Journal of Geodynamics”.



3.1 Abstract

We implement a 2D flexural model of thin elastic plate of infinite length to calculate changes on pressure suffered by upper crustal magmatic reservoirs due to glacial unloading. Our model considers isostatic recovering caused by a uniform hydrostatic pressure condition at the base of the model that is regulated by density contrast $\Delta\rho$ between the elastic plate and its inviscid substratum. Upper crustal decompression developed due to the combined effect of flexural unbending and isostatic recovering, depends on the value of physical parameters such as Young's modulus E, $\Delta\rho$, the elastic thickness and the magnitude of the (un)load. We consider deglaciation after the Last Glacial Maximum (LGM) for the Southern Andes where an adequate description of the overall process is available and its relation with large postglacial eruptions seems apparent. We test different values of these parameters and compare these results with those previously obtained by us with a model of thin elastic disc with no isostatic adjustment and no dependence on Young's modulus. For the same elastic thickness and load, both models can develop similar pressure profiles inside the elastic plate when E and $\Delta\rho$ take given values and maintain a certain proportion one to each other. However, the temporal evolution of pressure at a given depth during deglaciation differs between both models with the infinite plate with isostasy developing decompression values 2-3 times larger than the elastic disc at the end of deglaciation. Despite these differences, our results show that decompression values and time-varying rates are 1-3 order of magnitudes larger than commonly assumed when using an elastic half-space and therefore large enough to promote failure of reservoir wall and/or rapid exsolution of volatiles from magma, both contributing to upper crustal magma chamber collapse and triggering of ignimbritic eruptions as those characteristic of the Southern Andes after the LGM.

3.2 Introduction

The changes of stresses and pressures inside the earth's crust due to external forces of certain phenomena of nature can have a great impact on volcanic systems and their eruptive activity (e.g. Mauk & Johnston, 1973; Rikitake & Sato, 1989; Violette et al. 2001 Jellinek et al. 2004; Manga & Brodsky, 2006; Pinel et al. 2007; Pinel et al. 2009; Albino et al. 2010; Sigmundsson et al. 2010; Cañón-Tapia, 2013; Kutterolf et al. 2013; Pritchard et al. 2013; Sigmundsson et al. 2013). It is of great interest to understand the relationship between deglaciations and volcanic activity (e.g. Jull & McKenzie, 1996; Maclennan et al. 2002; Pagli & Sigmundsson, 2008; Huybers & Langmuir, 2009; McGuire, 2010; Tuffen et al., 2010 ; Watt et al., 2013; Brown et al., 2014; Rawson et al., 2016),

because the unloading on the surface of active volcanoes could affect their shallow magmatic reservoirs by changes in stresses and pressures inside it or at the magma chamber walls (e.g., Pinel & Jaupart, 2003; Pinel & Jaupart, 2005).

The impact of glacier unloading on magmatic reservoirs is commonly estimated with analytical models that consider an axis-symmetric disk load on an idealized terrestrial crust as an elastic half-space or infinite elastic thickness (e.g., Sigmundsson et al., 2010; Pinel & Jaupart, 2000; Pinel & Jaupart, 2004). The main parameter is the normal stress to the surface of the earth's crust, directly proportional to the thickness of the glacier load (h), this generates a maximum pressure on the surface (approximately 10 kPa - 10 MPa) and decreases in depth with a quotient that depends on the load radius (R) squared (e.g., Sigmundsson et al., 2010) and is negligible at depths greater than three times R (e.g., Pinel y Jaupart, 2005). In these models, the only rheological parameter included is the Poisson ratio (ν), which changes have a negligible effect.

Recently, Mora & Tassara (2019) implemented an analytical solution of flexure for a thin elastic disc with simply supported edges (Ugural, 1981) to develop a general formulation for temporal changes in stresses and pressure at upper crustal reservoirs below the center of an ice disc with the spatio-temporal constraint of southern Andean deglaciation (e.g., Denton et al., 1999) given by the numerical climate model of Hulton et al. (2002). The formulation of Mora & Tassara (2019), not only includes the rheological parameter ν , but also considers the elastic thickness (d) of the upper crust. In this model the pressure transmitted by the glacier load is greater, amplified by a factor of R^2 and decreasing in depth with a dependent ratio of d^3 . Their results show that, despite of rheological approaches on ν and d (Tassara et al., 2007) and the uncertainties on R at the Last Glacial Maximum (McCulloch et al., 2000; Hulton et al., 2002; Kaplan et al. al., 2004) along the Andes, deglaciation produces an upper crustal decompression of the order of tens to hundreds of megapascals at time-scales of hundreds of years, high enough to surpass the tensile strength of upper crustal rocks (5-20 MPa; Rubin, 1995; Tait et al., 1989; Pinel & Jaupart, 2003) and in general agreement with the time lag between LGM and explosive eruption (e.g., Lohmar, 2008; Lohmar et al., 2012; Watt et al., 2013; Weller et al., 2014; Fontijn et al., 2014; Rawson et al., 2015) along the Southern volcanic zone (SVZ).

In this paper, we evaluate the influence that flexural bending and isostatic recovering induced by glaciation would have on decompressing the crust around shallow magma chambers. We use an analytical solution of flexure for a two-dimensional thin-elastic plate of infinite-length with isostatic

recovering (Watts, 2001) to investigate the temporal changes in pressure below the center of an uniform and rectangular ice load with decreasing thickness and width during deglaciation. Compared to our previous model (Mora & Tassara, 2019), this new formulation additionally includes the Young's modulus (E) of the upper crust and the density contrast ($\Delta\rho$) between the glacial load and the underlying layer.

3.3 Analytical approximation and method

Our preferred interpretation for modeling a glacial load on the earth's crust is to consider the upper crust as a thin elastic plate floating on an inviscid fluid. The glacier load causes a downward deflection of the rigid plate and this load is compensated by buoyant forces at each point of its base, proportional to the vertical displacement of the deflection. The downward deflection of the loaded plate responds to the balance between the loading force, the flexural rigidity of the plate and the upward force (buoyancy of the material displaced) that act on the bent part of the plate. This is described by a general fourth-order differential equation (Watts, 2001; see Appendix B). We are using an analytical solution of this equation developed by Watts (2001) for the case of a two-dimensional thin-elastic plate of infinite-length loaded on its surface by a homogenously distributed force and with isostatic recovering caused by an uniform hydrostatic pressure at the base of the model as a Winkler foundation and that acts with a force that is proportional at every point to the deflection. We are interested in investigating the evolution of the pressure inside the upper crust, over time and in depth, during the glacial unloading. Therefore we do not need to worry about the displacement due to deflection of the plate, which is unknown.

3.3.1 Derivation of the equation for flexural deflection of a two-dimensional thin-elastic plate of infinite-length loaded on its surface

Below, we show the general context of our model and the main equation used in this paper (Eq. 3.1), which is derived from the equations presented in Watts (2001) and explained in detail in Appendix B. During the flexure of a thin plate for an elastic, homogeneous, linear and isotropic body and that is loading on its surface, the stress state is plane stress (vertical normal stress $\sigma_z^i(z, t)$ equal zero) and the stress tensor is represented in two dimensions (Turcotte & Schubert, 2014). Because the displaced material (i.e. mid-lower crust and mantle) could exert an upward load that acts on the base of the bent part of the plate due to the buoyancy of the foundation (Watts, 2001), we analyze this effect by comparing a previous model of flexure for a thin elastic disc with simply supported edges (Mora &

Tassara, 2019) with our flexural model of thin elastic-plate of infinite-length (Figure 3.1) that includes a buoyant underlying layer as a Winkler foundation (Watts, 2001) and assuming that behaves as an inviscid fluid (i.e. a fluid with zero viscosity). Then, pressure $P^i(z,t)$ along the vertical axis of symmetry (z-axis) within a thin-elastic plate is equal to average of horizontals orthogonal normal stresses components and is rewritten by us for a plate of infinite-length in the following equation as:

$$P^i(z,t) = -\frac{E(\rho gh(t))\lambda^2 e^{-\lambda R(t)} \sin(\lambda R(t))}{(1-\nu)(\rho_m - \rho)g} \left(\frac{d}{2} - z\right) \quad (\text{Eq. 3.1})$$

In this model, the geometry of the load is described by a rectangular ice cap with thickness $h(t)$ and width $R(t)$ that are allowed to change with time t , ρ_m is density of lower layer, ρ is density of ice (900 kg/m^3), g acceleration of gravity (9.8 m/s^2), d is the thickness of the thin elastic plate (i.e. the elastic thickness), ν is Poisson's ratio, E is Young's modulus and where $\lambda = \left[\frac{(\rho_m - \rho)g}{4D}\right]^{1/4}$ is a parameter that determines the amplitude and wavelength of the deformation (Watts, 2001) and $D = \frac{Ed^3}{12(1-\nu^2)}$ is the flexural rigidity of the plate (Walcott, 1970; Watts, 2001; Turcotte & Schubert, 2014). The boundary conditions of thin elastic-plate of infinite-length that apply defined by Watts (2001) are the following: a first condition is there isn't deflection w at far edges of the beam ($w \rightarrow 0$ at $x \rightarrow \pm \infty$) and a second condition ensure symmetry in the deflection either sides of where the load is applied ($\frac{dw}{dx} = 0$ at $x = 0$).

The weight of the rectangular ice cap is regionally compensated by the downward deflection of the plate and the flexural deflection of the plate creates large horizontal stresses above (compressional) and below (tensional) its middle (neutral) plane at $z=d/2$. In our coordinate system, z is zero on the surface and increases positively downward. We use a convention of signs where compressive stresses are positive and tensional stresses are negative.

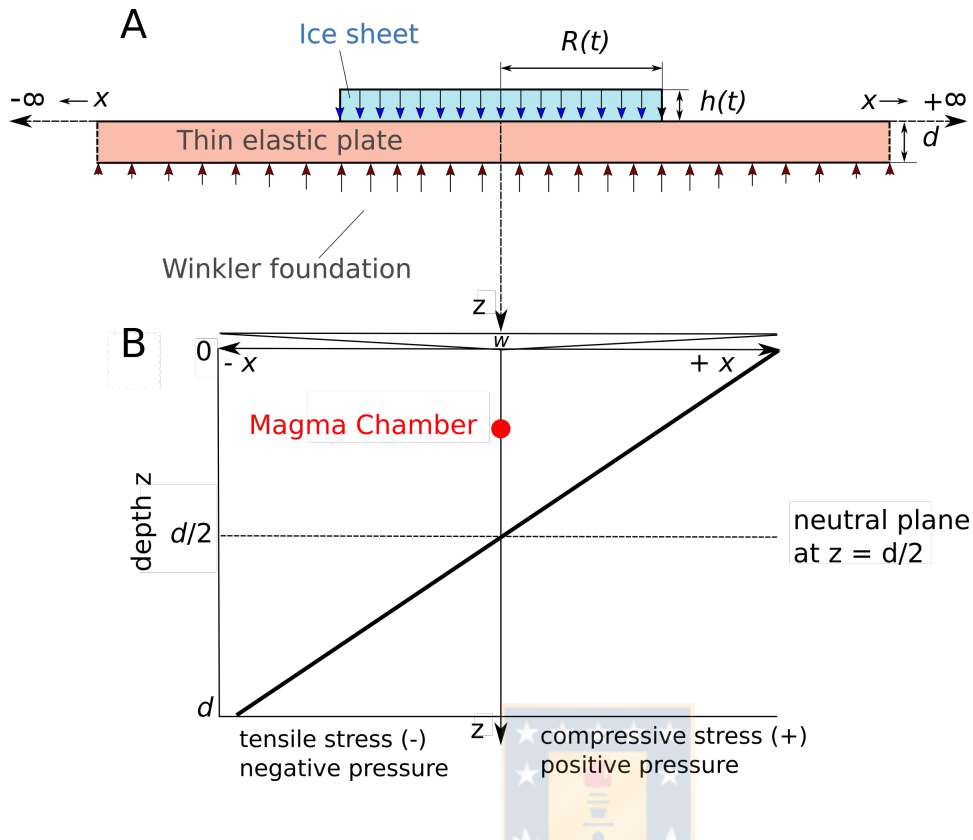


Figure 3.1: Basics of the physical model for flexure of a thin elastic-plate of infinite-length on a Winkler foundation and loaded by the weight of an ice sheet.

A) A cartesian coordinate system is used, and the axis-symmetry of the problem means that only the vertical (z) and horizontal (x) coordinates are relevant. The ice sheet load is defined by the width $R(t)$ and thickness $h(t)$ of the rectangular ice cap that can change with time t . This load generates a downward deflection of a thin elastic-plate of infinite-length and finite thickness d . The deflection is maximum at the center of symmetry of the plate and tends to zero at both edges located at an infinite positive/negative distance x from the center. The plate is supported on a Winkler foundation that exerts a hydrostatic pressure along its base. B) Vertical stress and pressure profile downward along the z -axis of symmetry underneath the center of the ice sheet and the thin elastic plate. Stresses are compressive/tensile and pressure is positive/negative respectively above/below the neutral plane of the thin elastic plate at $z=d/2$. We are interested on temporal changes on pressure that occur in a point representing the position of an upper crustal magma chamber.

3.3.2 Limitations of the model

The present model is a first-order approximation of the elastic response of a plate during deglaciation by deflection of the plate. We consider a thin elastic plate of infinite length, floating on an inviscid

fluid, omitting any possible effect of viscous media (lower-middle crust, asthenospheric mantle and magma inside the reservoir) that could increase the start time by several thousand years of the rebound of the plate after deglaciation (relaxation time of the viscous material, Turcotte & Schubert, 2014), increasing with the increase in viscosity (10^{19} - 10^{20} Pa s in the Southern Andes, Ivins & James, 1999). We used a history of simple deglaciation, varying the width (East-West) and the glacier thickness with our approximation of the history of deglaciation (Mora & Tassara, 2019) in the Southern Andes of the Hulton et al (2002) model. No topographic changes of the glacier surface or the elastic plate are incorporated, which could affect the distribution of pressures inside the plate. We consider an idealized magmatic chamber as a point located in the region superior to the neutral plane of the elastic plate, neglecting any influence on the internal pressures of the reservoir due to the rheological effects of its walls and the magma inside it. The main limitation of the model is related to the physical sense of its results. We expect a decrease in pressure during deglaciation in the region above the neutral plane of the elastic plate, therefore this model is valid only for negative slopes of the tangent line to the curve of decrease in pressure during deglaciation, this is true only when the derivative of the pressure with respect to the time factor is $dP/dQ(t) < 0$ (for more details see section 3.4.3).



3.4 Result

In this paper, we compare the resulting pressures inside the thin elastic plates by the effect of a glacier load on their surfaces. We contrasted a two-dimensional model of thin elastic-plate of infinite-length (with hydrostatic pressure) with our previous model (Mora & Tassara, 2019) of thin-elastic disc uniformly loaded and simply supported (without hydrostatic pressure), in order to know under which rheological conditions the model with hydrostatic pressure approaches the reference model without hydrostatic pressure. Different experiments were carried out where both models are loaded with a glacier of 1500 m in thickness and 100 km in width.

3.4.1 The Young's modulus (E) as a function of the density contrast ($\Delta\rho$)

In a first experiment we investigated the dependence of the Young's modulus (E) as a function of the density contrast ($\Delta\rho$) between the ice sheet and the underlying foundation of thin elastic-plate of infinite-length, considering a constant pressure at a certain depth. We observe a directly proportional $E(\Delta\rho)$ relation (Figure 3.2), where higher values of E require higher values of $\Delta\rho$ to achieve the same

pressure at the same depth. Such a relationship is necessary to find the conditions in which the new model used here approaches our previous model (Mora & Tassara, 2019).

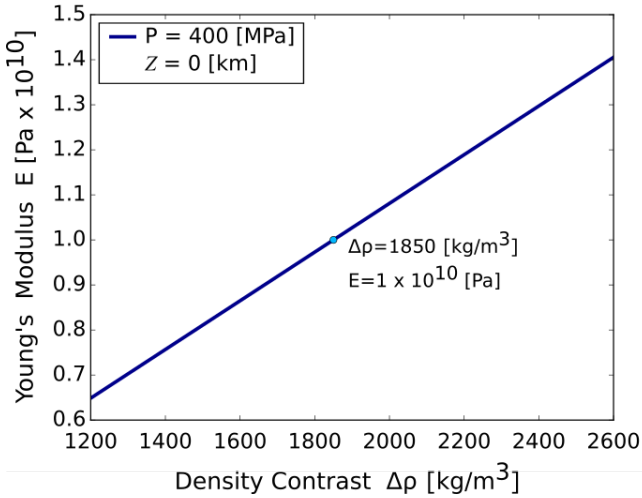


Figure 3.2: Dependence of the Young's modulus (E) as a function of the density contrast ($\Delta\rho$) of thin elastic-plate of infinite-length considering a constant pressure at a certain depth.

We evaluate the conditions in which the thin elastic-plate of infinite-length approximates a model of thin-elastic disc simply supported. The blue line represents the range of values ($\Delta\rho$, E) with a pressure P equal to 400 MPa at a point located on the surface ($Z = 0$ km), equivalent to the pressure just below the center of a glacier (width $R_0 = 100$ km and thickness $h_0 = 1500$ m) on a thin-elastic disc simply supported. Note that the light blue point relates a density contrast $\Delta\rho = 1850$ kg/m³ with a Young's modulus $E = 1 \times 10^{10}$ Pa.

3.4.2 Model sensitivity to Young's modulus (E) and the density contrasts ($\Delta\rho$)

To investigate the sensitivity of the model with hydrostatic pressure, a range of densities of 1200 - 2600 kg/m³ was tested, representing the density contrast between a foundation or underlying layer (crust or mantle) and glacial ice, along with testing a range of Young's modulus of 1 - 7 × 10¹⁰ Pa of the thin elastic plate. The results indicate a low sensitivity of the model for moderate to high values of Young's modulus (3 - 7 × 10¹⁰ Pa) of the thin elastic plate and a high sensitivity to density contrasts. We found that a thin plate with a low Young's modulus (1 × 10¹⁰ Pa) shows a good fit with a moderate density contrast (1850 kg/m³, Figure 3.3B), despite not satisfying the restrictions of the model. For a very-low (1200 kg/m³) or very-high density contrast (2600 kg/m³) and within the wide range of Young's modulus evaluated, the calculated pressures tend to be out of adjustment with the reference

model (Figures 3.3A- 3.3C). As will be seen below, using an E as low as 1×10^{10} Pa for a glacier of initial width (R_0) of 100 km and a moderate density contrast ($\Delta\rho$) of 1850 kg/m^3 , causes a pressure curve during the deglaciation that does not have a negative slope throughout its travel, which is expected in the region on the neutral plane of a thin elastic plate during the decompression and deflection of this. For the model to be valid with the above conditions, it is then required to use a smaller $\Delta\rho$ (1200 kg/m^3) or to use a minimum Young's modulus (E_{\min}) of 2×10^{10} Pa for $\Delta\rho$ range $1850\text{-}2600 \text{ kg/m}^3$.

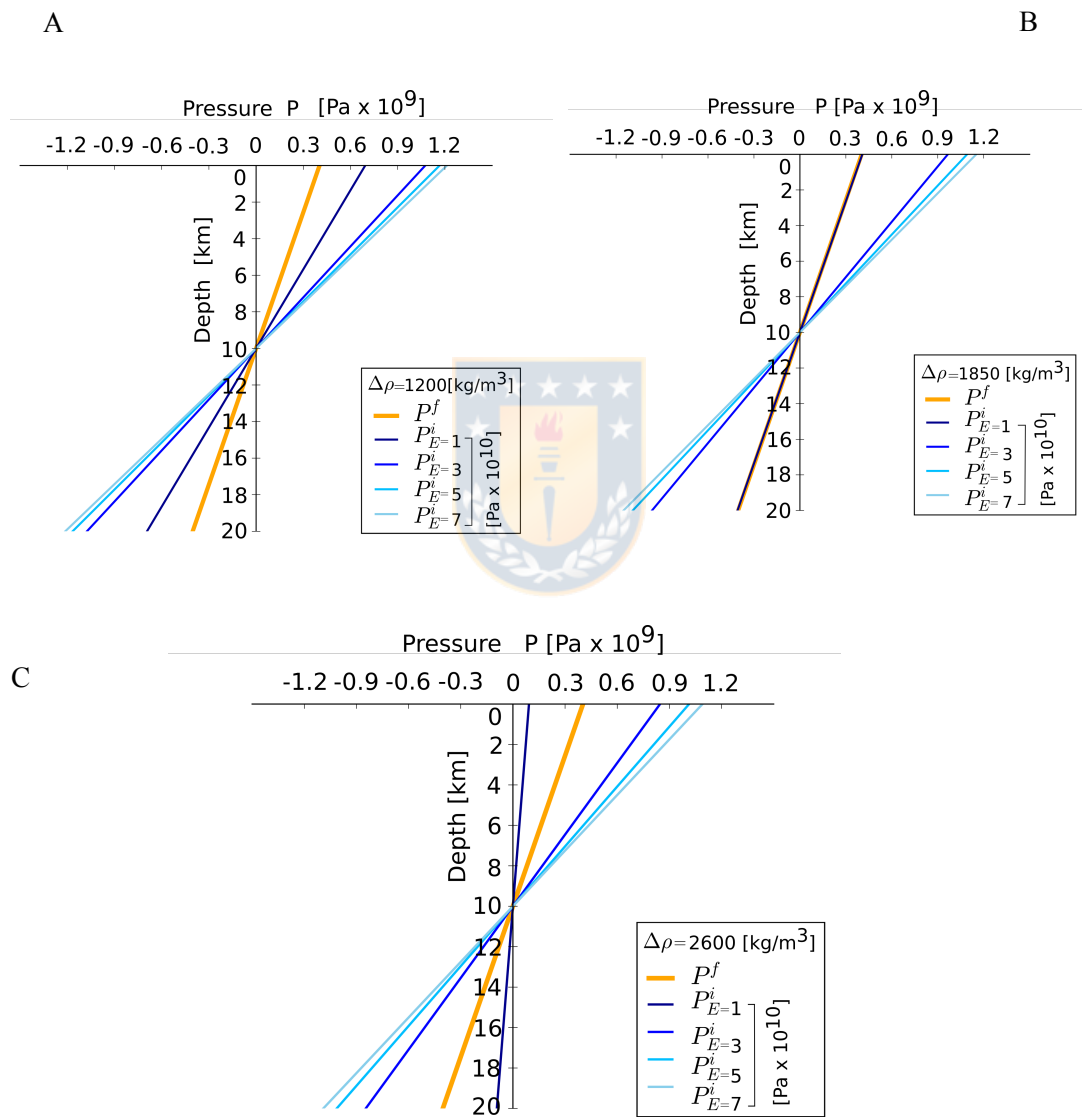


Figure 3.3: Comparisons of pressures (A, B and C) calculated with the models of thin-elastic disc simply supported (orange line; Mora & Tassara, 2019) and a thin elastic-plate of infinite-length (blue lines).

Both models of thin plates are loaded uniformly on their surfaces with a glacier of 1500 m in thickness (h_0) and 100 km in width (R_0). In both models, we used a Poisson ratio (ν) equal to 0.25; 20 km elastic thickness (d) and evaluated different density contrast values ($\Delta\rho$: 1200 - 2600 kg/m³) and Young's modulus (E: 1-7 x 10¹⁰ Pa) in the thin elastic-plate of infinite-length.

3.4.3 Decrease in pressure (P) and model restrictions

The model of thin elastic plate of infinite length is valid only for negative slopes of the tangent line to the curve of decrease in pressure during deglaciation, that is, only when $dP/dQ(t) < 0$. The pressure depends on several parameters (E, R_0 , $\Delta\rho$, and d) that can be restricted by analyzing the curves of the pressure decrease during deglaciation so that the validity criterion of the presented model is met. In the following experiment (Figure 3.4), setting some parameters ($d = 20$ km, $\nu = 0.25$, $\Delta\rho = 1850$ kg/m³, $R_0 = 100$ km, $Z = 5$ km) and varying E (1-7 x 10¹⁰ Pa), it is possible to observe that the model is only valid for $E \geq 20 \times 10^{10}$ Pa. In the same way we show (Table 3.1) that there is a minimum Young's modulus (E_{\min}) for the model to be valid according to different combinations of R_0 (50,100 and 150 km), $\Delta\rho$ (1200,1850 and 2600 kg/m³) and d (10, 20 and 40 km).



Table 3.1: Range of validity parameters of the thin elastic plate model of infinite length for glaciers with initial width 50, 100 and 150 km; satisfying the constraint of the model $dP/dQ(t) < 0$.

$E_{\min} \times 10^{10}$ [Pa]	R_0 [km]	$\Delta\rho$ [kg/m ³]	d [km]
5; 8; 11	150	1200; 1850; 2600	20
12	100	1850	10
1; 2	100	1200; 1850-2600	20
1	100	1850	40
1	<50	1200-2600	20

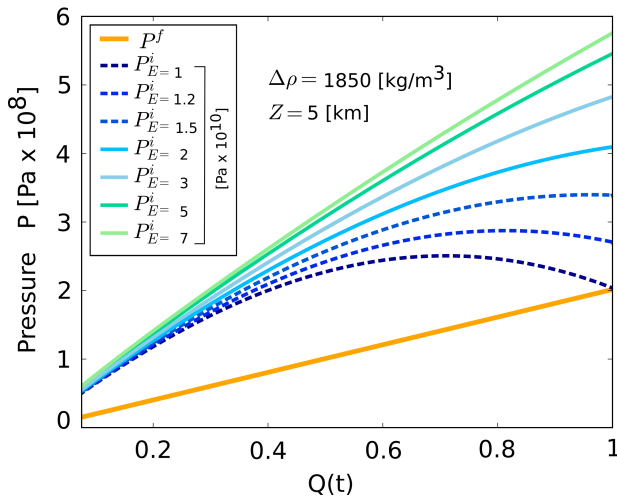


Figure 3.4: Decrease in pressure during deglaciation in the Southern Andes.

The pressures are calculated at a constant depth $Z = 5$ km, with constant parameters ($d = 20$ km, $v = 0.25$ and $\Delta\rho = 1850 \text{ kg/m}^3$). The thin elastic plate model of infinite length is valid for $dP/dQ(t) < 0$. In this example, the model is valid for $E_{\min} \geq 2 \times 10^{10} \text{ Pa}$ (blue-light to green lines). The dotted blue lines indicate the cases in which the model is not valid ($E < 2 \times 10^{10} \text{ Pa}$). Note that the thin elastic disc model (orange line) generates lower pressure values than the thin elastic plate model of infinite length.



3.4.4 Increase in pressure change (ΔP) during deglaciation in the Southern Andes

In the following experiment, the increase in pressure change (ΔP) during deglaciation of both models at a constant depth of 5 km is compared. The model of thin elastic-plate of infinite-length shows a non-linear behavior in the increase of the pressure change in time during deglaciation in plates with Young's modulus of low to moderate values ($2-3 \times 10^{10} \text{ Pa}$), in relation to the linear behavior of the thin-elastic disc simply supported (Figure 3.5). In contrast, a thin elastic-plate of infinite-length with high values of Young's modulus ($5-7 \times 10^{10} \text{ Pa}$) tends to have a linear behavior of these changes over time. The total decompression and estimated decompression rates, with the thin elastic plate model of infinite length, for the first hundred and a thousand years after the deglaciation onset are 200-450 MPa and 2000-450 kPa/yr, respectively.

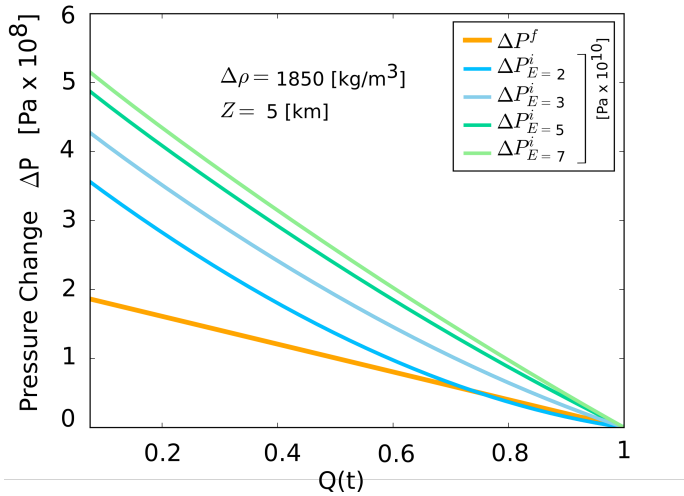


Figure 3.5: Increase in pressure change during deglaciation in the Southern Andes.

Comparison at a depth of 5 km of the thin elastic plate models of infinite extension (blue-green lines) in a wide range of values of Young's modulus ($2-7 \times 10^{10} \text{ Pa}$) with constant density contrast (1850 kg/m^3) and the model of thin elastic disc simply supported (orange line). In both models, $d = 20 \text{ km}$ and $v = 0.25$ are constant; and they are loaded with an initial glacier of 1500 m in thickness and 100 km in width. The start of deglaciation is represented by a time factor $Q = 1$, where $Q = 0$ is the present time.

3.4.5 Depth of decompression $Z\Delta P$ as a function of the deglaciation factor $Q(t)$ in the Southern Andes

In the models of thin elastic plate of infinite length, the Young's modulus is a control factor in the start time of certain decompression magnitudes at a certain depth. The plates with smaller Young's modulus (Figure 3.6A) reach certain decompression values at later instants compared to plates with larger Young's modulus (Figure 3.6B). With larger values of the Young's modulus, the elastic thin plate of infinite extension tends to a more linear graph (Figure 3.5) at a certain depth, implying a greater similarity with a model of thin elastic disc simply supported during deglaciation (Figure 3.6).

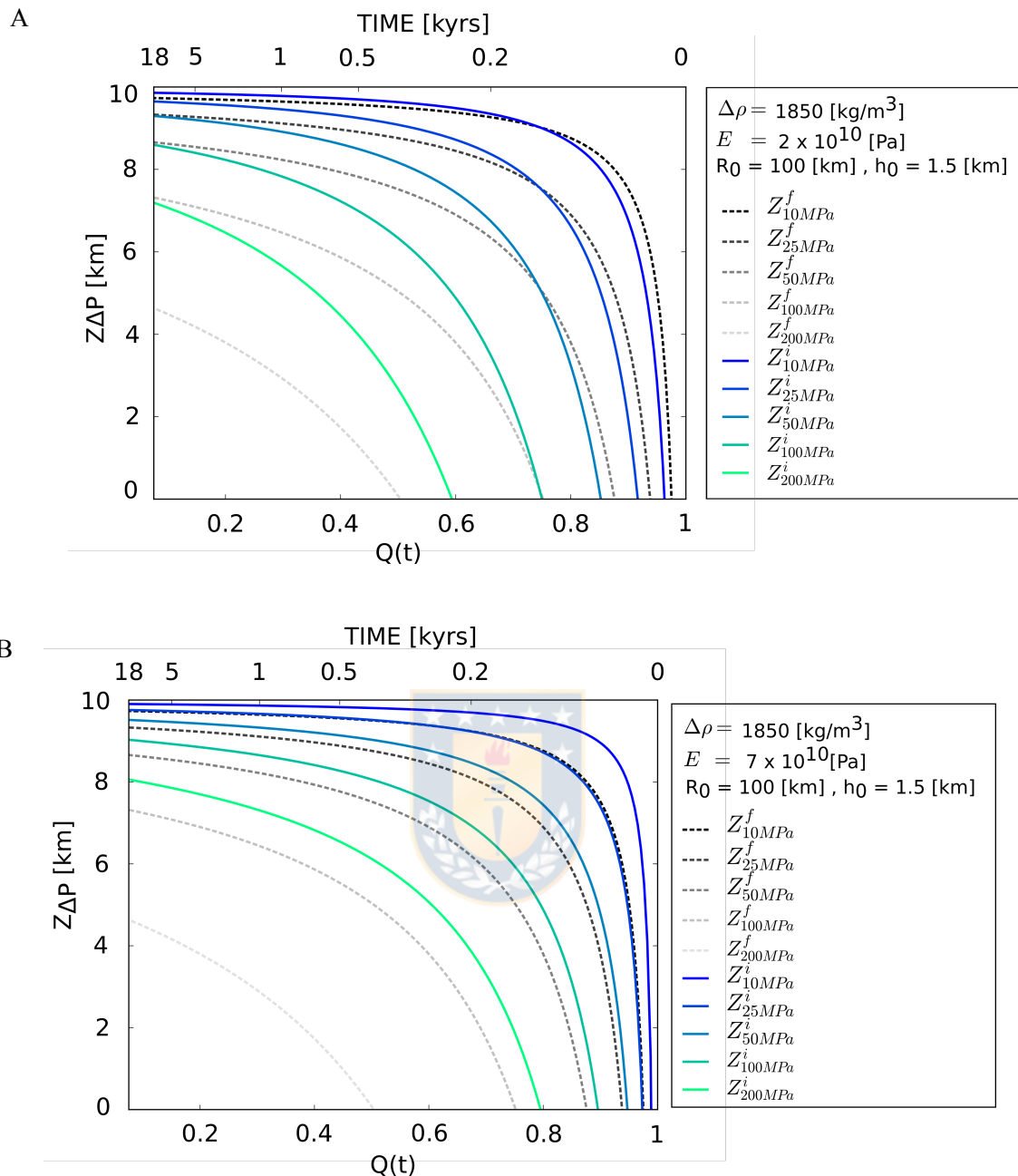


Figure 3.6: Depth of decompression as a function of the deglaciation factor in the Southern Andes. (A: E= 2×10^{10} Pa; B: E= 7×10^{10} Pa).

Comparison between the thin elastic plate model of infinite extension and the model of thin elastic disc simply supported. Both models are loaded initially with a glacier of 1500 m in thickness and 100 km in width, evaluating decompressions in a wide range (10-200 MPa) to certain depth. A) A thin plate of infinite extension is evaluated with a low value of Young's modulus (2×10^{10} Pa). There is a tendency to delay the occurrence of decompressions at certain depths with a smaller Young's modulus. B) A thin plate of infinite extension with high value of Young's modulus (7×10^{10} Pa) is evaluated. Decompressions occur earlier at certain depths with a

greater Young's modulus. A density contrast of 1850 kg/m^3 is considered in both cases of thin elastic plate of infinite extension.

Another parameter that causes a delay in the occurrence of decompressions at certain depths, demonstrated previously with a model of thin elastic disc (Mora & Tassara, 2019), is a glacier of smaller initial dimensions (Figure 3.7) in a thin plate model elastic of infinite length with identical characteristics (E , d , $\Delta\rho$ and v), in relation to a model initially loaded with a larger glacier (Figure 3.6B).

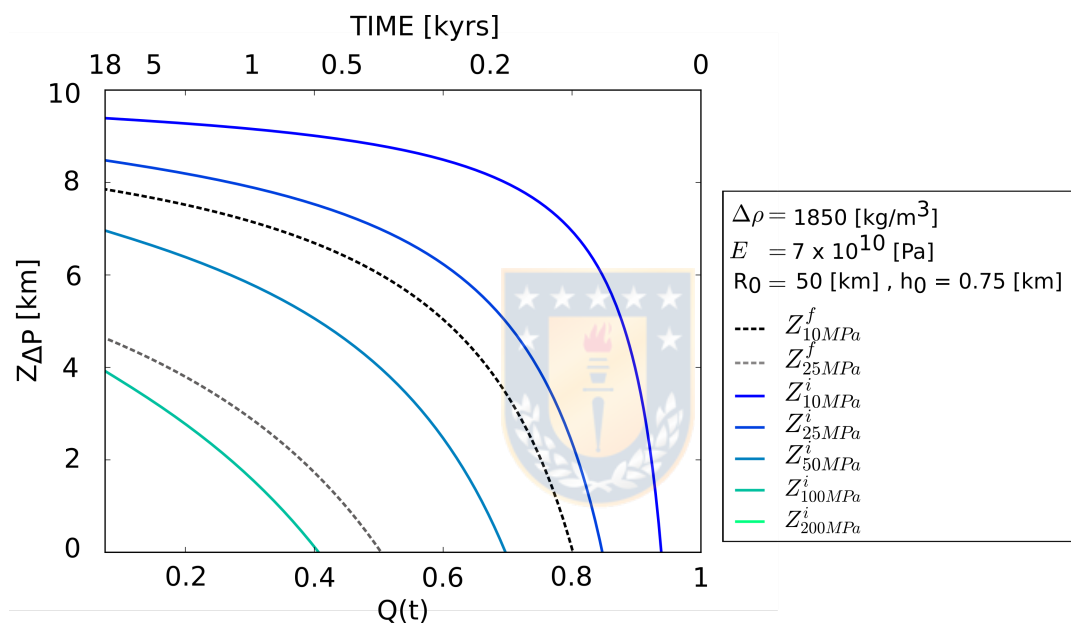


Figure 3.7: Glacier with smaller R_0 and h_0 (respect figure 3.6B).

In both models, a glacier of smaller initial dimensions causes changes in pressure at certain depths to occur later than for glaciers of larger initial dimensions.

Other ways to delay the occurrence of decompressions at certain depths during deglaciation is to increase the density contrast between the glacial ice and the foundation of the elastic plate (Figure 3.8) or increase the elastic thickness (Figure 3.9).

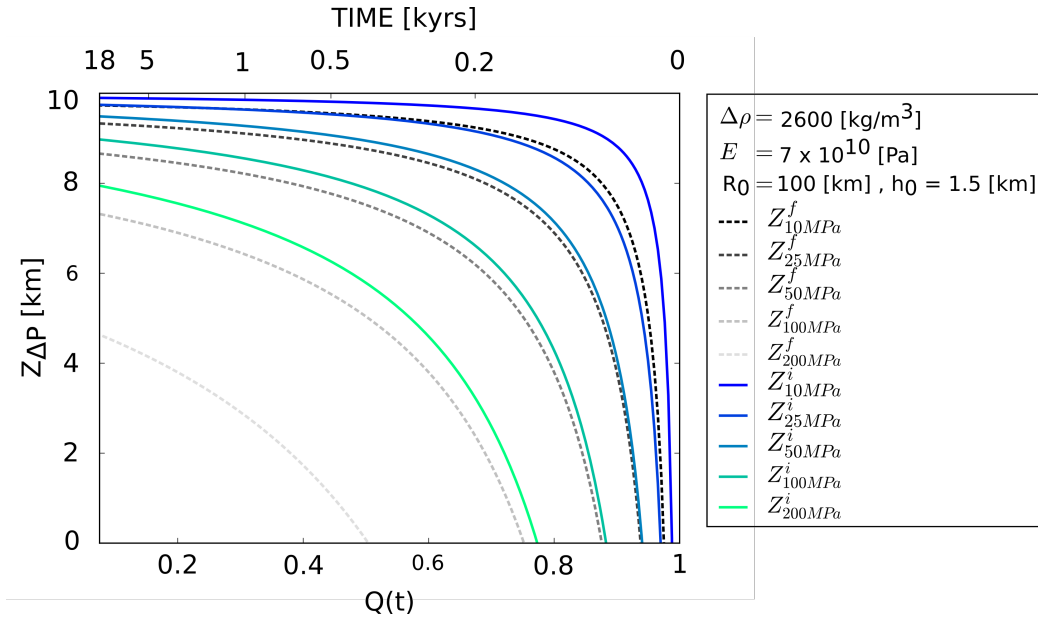


Figure 3.8: Effect of a higher density contrast (respect figure 3.6B)

A higher density contrast causes certain pressure changes to occur later at certain depths.

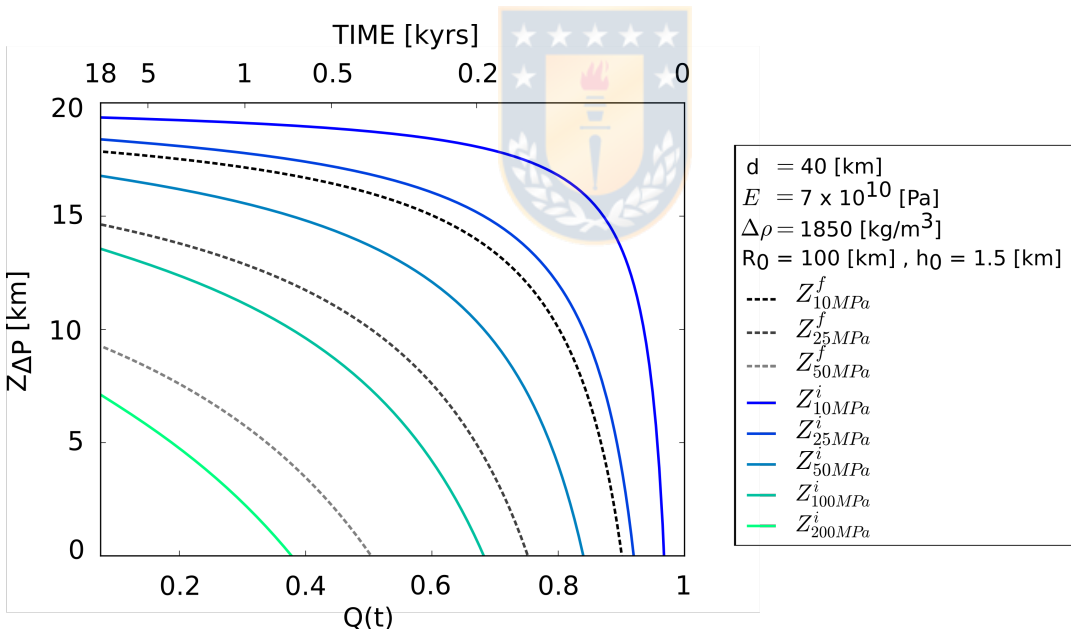


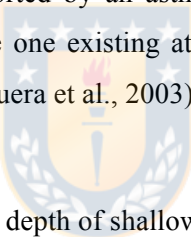
Figure 3.9: Effect of a greater elastic thickness (respect Figure 3.6B).

A greater elastic thickness causes certain pressure changes to occur later at certain depths.

3.5 Discussion

3.5.1 Rheological implications

From the comparison between flexure models, thin elastic disc simply supported (Mora & Tassara, 2019) and infinite-length elastic-plate, implemented to investigate the impact of deglaciation in shallow volcanic systems in the Southern Andes during the LGM, it is possible to make some rheological approximations of the deflected plate and the underlying layer. Both models approximate in a pressure profile as a function of depth (Figure 3.3B) and in pressure changes as a function of the deglaciation factor (Figure 3.5) for a moderate density contrast (1850 kg/m^3), consistent with an underlying layer of granitic rocks of the middle crust and a wide range of Young modules ($2-7 \times 10^{10} \text{ Pa}$) consistent with igneous and sedimentary rocks of the upper crust (Turcotte & Schubert, 2014). The depth of decompression as a function of the deglaciation factor shows a marked dependence with the Young's modulus, where both models approximate with a wide range of E ($2-7 \times 10^{10} \text{ Pa}$, Figure 3.6). With the previous rheological conditions, both models are consistent with the flexure of an upper crust supported by a middle crust, in agreement with the volcanic-sedimentary and granitic rocks existing in the Southern Andes. The approximation of both models for a high density contrast (2600 kg/m^3) would indicate a lithosphere thinned and supported by an asthenospheric mantle, applicable to areas with asthenospheric flow or windows like the one existing at 45° - 46°S product of the subduction of the dorsal Chile (e.g. Russo et al., 2010; Folguera et al., 2003).



3.5.2 Implications in the estimation of the depth of shallow magmatic chambers

Young's modulus also shows a control in the depth at which certain decompressions occur in a certain period of time. With low Young's modulus ($2 \times 10^{10} \text{ Pa}$; Figure 3.6A), a certain decompression (e.g. 100 MPa) occurs in a certain period of time (e.g. about 1 kyr) at a lower depth (e.g. about 8 km) compared to the greatest depth of occurrence (e.g. about 9 km) when the Young's modulus is larger ($7 \times 10^{10} \text{ Pa}$, Figure 3.6B). This could have an implication when we want to establish relationships between the magnitudes of the decompressions and the depth of location of a magmatic chamber, as in the case of the Southern Andes where the explosive postglacial eruptions related to decompressions of the order of tens of MPa (e.g. Eruption of the Lican ignimbrite, Villarrica volcano; Lohmar et al., 2012) have occurred between the first hundreds of years and a thousand years after the last glacial maximum in volcanoes with shallow magmatic chambers (<10 km in depth).

3.6 Conclusions

The deflection of thin elastic plates is a first order mechanism in the decompression of magmatic chambers located in the upper crust (<10 km in depth). The model of thin elastic plate of infinite length incorporates parameters that allow an approximation of the rheological characteristics of the elastic plate and its foundation or underlying layer. Both models compared (thin elastic disc and elastic plate of infinite length) allow to investigate the evolution of decompression and estimate its depth (could be related to the depth of the magmatic reservoir) and time of occurrence. Assuming some constant parameters (d , v , $\Delta\rho$ and E) in thin elastic plate models of infinite length, we verify that like in thin elastic disc model, certain decompressions occur earlier (and deeper) for initial loads of larger glaciers and occur later (and at lower depths) for lower initial glacial loads. Other parameters that cause the later occurrence and in lower depth of certain decompressions are smaller E or greater $\Delta\rho$. The effect of the elastic thickness d is to cause decompressions later and deeper for higher values of this. We consider that the use of these models allows us to investigate in first order the changes in the state of stresses and pressures generated by the loading and unloading of glaciers both in the past and in the present. We show that both models are valid and can be applied to estimate the decompression of reservoirs in the upper crust as a result of past deglaciations or the current retreat of the glacial masses that affect Quaternary volcanoes in the Southern Andes and in other areas of high-latitudes.



CAPÍTULO IV: SÍNTESIS Y DISCUSIÓN

De acuerdo con lo discutido en los capítulos 2 y 3, el mecanismo de deflexión de la litosfera elástica debido a la descarga glaciar sobre áreas volcánicas es un proceso de primer-orden que induce la descompresión de cámaras magmáticas poco profundas, conduce al estado de esfuerzos de la corteza superior y de las paredes de cámaras magmáticas poco profundas a sobrepasar el límite de resistencia a la tensión de las rocas y permitir la inyección de diques dentro y fuera de un reservorio magmático. Por lo tanto, las desglaciaciones contribuyen a regular la liberación de magma almacenado en la corteza superior y promueven la ocurrencia de erupciones explosivas postglaciares.

En el capítulo 2, utilizando un modelo de disco delgado elástico con bordes simplemente soportados, se demuestra que el mecanismo de deflexión de placas delgadas elásticas y escencialmente considerar un espesor finito para modelar la corteza superior sometidas a cargas superficiales, conduce a descompresiones de decenas a centenas de megapascales que permiten sobrepasar el límite de resistencia a la tensión de las rocas (5-20 MPa; Pinel & Jaupart, 2003) y tasas de descompresión de centenas de kilopascales/año (ej., 300-150 kPa/año). Esto supera en 1-2 ordenes de magnitud a los estimado por previos autores con modelos de cargas superficiales sobre un semiespacio elástico, con lo cual solo es posible estimar valores en un rango desde kilopascales hasta algunos megapascales (ej., kPa-10 MPa).

Otro tema importante tratado en el capítulo 2 es el rol de la deflexión de la corteza superior en las erupciones postglaciares explosivas en los Andes del Sur. Las erupciones postglaciares parecen tener un aparente tiempo de retardo, entre el inicio de la desglaciación y la ocurrencia de las erupciones, que aumenta desde el sur en el volcán Hudson (0-60 años) hasta el norte en los volcanes Villarrica (660-1080 años) y Llaima (1000-1180 años). Una descompresión más temprana inducida por la desglaciación, aplicando un modelo de deflexión de disco elástico delgado, podría ser controlado por tres parámetros independientes: un menor espesor elástico (d), una menor profundidad (z) del reservorio o un glaciar inicial de mayor tamaño (R_0 y h_0). Durante el UMG en los Andes del Sur, el mayor tamaño glaciar inicial en el sur respecto del norte (ej., McCulloch et al., 2000) sería en primera instancia responsable de la aparente relación espacio-temporal de las erupciones postglaciares, debido a que d tiene valores aproximadamente constantes (20 km; Tassara et al., 2007) y la profundidad de ubicación de los reservorios superficiales es poco acotada por los estudios existentes, indicando amplios rangos de 2-14 km en el Hudson (Kratzmann et al., 2009; Delgado et al., 2014), 1.5-8 km en el

Villarrica (Lohmar et al., 2008, 2012; Delgado et al., 2017), y 2-12 km en el Llaima (Bouvet De Maisonneuve et al., 2012; Ruth et al., 2016; Bishop et al., 2018). Por otro lado, nuestros resultados permiten estimar rangos de profundidades de los reservorios asociados a un determinado cambio de descompresión, por ejemplo si consideramos $d=20$ km y $\Delta P= 30$ MPa, las profundidades estimadas de los reservorios son 0-9.5 km en el Hudson, 4-6 km en el Villarrica y 2 km en el Llaima.

El alto contenido de gases en los magma pre-eruptivos son una condición importante para que ocurran las erupciones explosivas (ej., vesículas > 53 % en vol. en la Ignimbrita Licán, volcán Villarrica; Lohmar et al., 2012). Las elevadas tasas de descompresión (300-150 kPa/año) estimadas por la deflexión de un disco delgado elástico y los tiempos de retardo en la ocurrencia de las erupciones en los Andes del Sur, sugieren que las desglaciaciones podrían favorecer la exsolución de gases del magma pre-eruptivo por cientos de años en el reservorio y también, la propagación de diques y recarga de magma debido a que la enorme descompresión total (> 10-100 MPa) supera el límite de resistencia a la tensión de las rocas.

En el capítulo 3, utilizamos un modelo de deflexión de una placa elástica delgada de longitud infinita. Se estima que dentro de los primeros cien y mil años iniciada la desglaciación en los Andes del Sur, la descompresión total (200-450 MPa) y las tasas de descompresión (2000-450 kPa/año) son superiores a las estimadas con el modelo de disco elástico delgado y por lo tanto, también podrían ser suficientes para provocar la exsolución de gases del magma pre-eruptivo y promover la inyección de diques en la corteza superior. Sin embargo, es recomendable evaluar modelos termodinámicos en futuros trabajos para obtener resultados concretos del aumento de exsolución de gases con las tasas de descompresión obtenidas con ambos modelos. El segundo modelo incluye nuevos parámetros, el módulo de Young y el contraste de densidad, permitiendo caracterizar el medio elástico y la fundación bajo la corteza superior. De acuerdo con nuestras estimaciones utilizando un glaciar con dimensiones iniciales $R_0=100$ km y $h_0=1500$ m, un espesor elástico $d=20$ km y $v=0.25$, es posible determinar un $E_{min}= 2 \times 10^{10}$ Pa en la corteza superior y un rango de $\Delta p= 1850-2600$ kg/m³ indicando la corteza podría estar flotando sobre una corteza media o el manto astenosférico. El efecto de E es aumentar o disminuir los tiempos de retardo de la ocurrencia de una determinada descompresión (podría estar asociada al cambio de presión necesario para inducir una erupción explosiva) para valores bajos o altos del módulo de Young, respectivamente. Los valores de Δp bajos (altos), se asocian a una disminución (aumento) de los tiempos de retardo de la ocurrencia de determinadas descompresiones.

El trabajo en esta tesis destaca el importante efecto de la descarga glaciar como principal y única “entrada” de variación de carga superficial en los modelos de flexión de placas elásticas delgadas presentados. En este sentido se debe mencionar que existen otros dos procesos que también contribuyen con la carga/descarga sobre la superficie de la corteza terrestre durante períodos de glaciación/desglaciación. El primer proceso adicional es la redistribución de cargas en la superficie terrestre debido a la modificación del relieve por erosión glaciar y formación de depósitos glaciares, lo cual es evidenciado por la creación de cuencas glacilacustres y depósitos morrénicos (ej., McCulloch et al., 2000). Las rocas tienen una densidad hasta 3 veces la densidad del hielo y las tasas de erosión glaciar en ciclos de glaciación/desglaciación son ~1-10 mm/año, pudiendo ocasionar tasas de descompresión ~0.1-0.4 kPa/año (Sternai et al., 2016). En este caso, Sternai et al. (2016) consideran en su aproximación la presión (p) liberada por el peso de la columna de roca erosionada ($p=\rho_r gh_r$; ρ_r : densidad de la roca, g : aceleración de gravedad, h_r : espesor columna de roca), lo cual genera magnitudes de presiones inferiores a las que podríamos estimar con modelos de flexura. A pesar de esto, la descompresión de la corteza superior debido a la liberación de cargas superficiales durante una desglaciación podría ser amplificada por la erosión glaciar en adición a la descarga de hielo. Por otro lado, durante la etapa glaciar, los extensos terrenos podrían ser protegidos más que erosionados (ej., Gjermundsen et al., 2015; Thomson et al., 2010). El segundo proceso adicional es la redistribución de cargas superficiales del agua de deshielo: su acumulación genera lagos proglaciares. Es destacable que muchos de los lagos formados en cuencas de erosión glaciar existían en el momento que ocurrieron las erupciones explosivas postglaciares en la ZVS, evidenciado por la depositación de los productos piroclásticos dentro de estos lagos, tal como el caso de las tefras H_0 del volcán Hudson (ej., Weller et al., 2014). Los lagos proglaciares podrían aumentar los esfuerzos compresivos horizontales y cargar lateralmente los reservorios superficiales, los cuales presentan un estado inestables debido a la descompresión ocasionada por la desglaciación, contribuyendo probablemente a la generación de una erupción explosiva.

CAPÍTULO V: CONCLUSIONES

En áreas volcánicas activas, la retirada de los glaciares durante una desglaciación, conducen a la liberación de enormes cargas y ocasionan la deflexión de la corteza superior. La deflexión de la corteza superior (placa elástica de espesor finito) es un mecanismo de primer orden en la descompresión y fracturamiento de reservorios magmáticos superficiales durante una desglaciación. Este mecanismo crea en cientos de años un estado pre-eruptivo propicio para una erupción volcánica explosiva, dado que la descompresión conduce al reservorio superficial a un estado inestable ocasionado por el fracturamiento de las paredes de la cámara magmática y posiblemente podría aumentar la exsolución de gases dentro del reservorio. En adición, la descompresión total y las tasas de descompresión del magma pre-eruptivo podrían aumentar por la liberación de cargas debido a la erosión glaciar durante la desglaciación.

En el caso de los Andes del Sur, la respuesta del arco volcánico a la desglaciación es reflejada en el retardo desde el sur en el volcán Hudson (aprox. 100 años) hasta el norte en los volcanes Villarrica (aprox. 660-1080 años) y Llaima (aprox. 1000-1180 años) de la ocurrencia de las erupciones explosivas (según edades radiocarbono calibradas en depósitos piroclásticos) en cientos a mil años posteriores al inicio relativamente sincrónico de la desglaciación (17.5-17.2 ka BP; Denton et al., 1999; McCulloch et al., 2000) sobre todo el arco volcánico. Este retardo es consistente con el mayor tamaño inicial de las cargas glaciares en el sur respecto al norte durante el UMG, induciendo una mayor o menor descompresión total y ocasionando que una determinada descompresión total sea alcanzada más temprano o más tarde, respectivamente. Los rangos de descompresión total y las tasas de descompresión a los cien y mil años posteriores al inicio de la desglaciación, estimadas con un modelo de disco elástico delgado con bordes simplemente soportados y un modelo de placa elástica delgada de longitud infinita son 30-150 MPa y 300-150 kPa/año, 200-450 MPa y 2000-450 kPa/año, respectivamente. Estos valores superan 1-3 veces las estimadas por previos autores con un modelo de semiespacio elástico (ej., Sigmundsson et al., 2010), demostrando el enorme impacto del mecanismo de deflexión de la corteza superior en la descompresión de reservorios superficiales durante una desglaciación.

Utilizando un modelo de deflexión de una placa elástica delgada de longitud infinita sobre una fundación de Winkler, nuestros resultados indican que los valores de E altos (bajos) y $\Delta\rho$ bajos (altos), se asocian a una disminución (aumento) de los tiempos de retardo de la ocurrencia de determinadas

descompresiones (ΔP). Estas, posiblemente están relacionadas a condiciones pre-eruptivas de erupciones volcánicas explosivas postglaciares.

Otros parámetros de control en el tiempo de retardo de ocurrencia de ΔP , común en ambos modelos investigados, son el espesor elástico (d) y la profundidad (z) de ubicación del reservorio. Un valor d bajo (alto) y un valor de z bajo (alto) conducen a una disminución (aumento) del tiempo de retardo. En los Andes del Sur d es aproximadamente constante (10-20 km; Tassara et al., 2007), por lo tanto no está relacionado al aumento sur-norte de los tiempos de retardo de las erupciones postglaciares en la ZVS. Por otro lado, las estimaciones de z existentes sugieren amplios rangos de 2-14 km en el Hudson (Kratzmann et al., 2009; Delgado et al., 2014), 1.5-8km en el Villarrica (Lohmar et al., 2008, 2012; Delgado et al., 2017), y 2-12 km en el Llaima (Bouvet De Maisonneuve et al., 2012; Ruth et al., 2016; Bishop et al., 2018), no siendo posible su uso para establecer una relación con el retardo de las erupciones postglaciares en la ZVS.

Considerando que la litosfera no es deformada significativamente a escala de tiempo geológico menor a 10^9 años, es válida nuestra simplificación de elasticidad lineal. Ambos modelos de flexura de placa elástica delgada pueden ser complementarios. Desde el punto de vista de los resultados, es posible obtener un rango de la descompresión ocasionada por una determinada historia de desglaciación sobre reservorios magmáticos superficiales, para idénticos valores de la dimensión de la carga glaciar, razón de Poisson, espesor elástico de la corteza superior y profundidad de ocurrencia de la descompresión. En adición, el modelo de flexura de una placa elástica de longitud infinita (sobre una fundación de Winkler) permite considerar las fuerzas de boyantes asociadas al contraste de densidades entre el sustrato bajo la placa deflectada y la masa glaciar sobre esta. Utilizar un contraste de densidad bajo permite modelar una corteza superior sobre una corteza media-inferior y un contraste de densidad alto, implica un sustrato de manto astenosférico. Entonces, en determinados casos la aproximación de los resultados de ambos modelos permite acotar las características elásticas de la placa deflectada y definir el sustrato bajo esta.

Dado que existen otros procesos que redistribuyen las cargas superficiales durante una desglaciación, futuros trabajos podrían incluir otras “entradas” de cargas superficiales como la redistribución de cargas por erosión glaciar y formación de lagos proglaciares.

ANEXOS

ANEXO 1: Derivation of the equation for flexure of a cylindrical thin elastic plate under uniform load (Appendix A)

Here we present a detailed derivation of the equations developed by Ugural (1981) for axisymmetrical deflection of a uniformly loaded thin, elastic, circular plate with simply supported edges.

The most general form of the equation governing the vertical deflection w suffered by a thin elastic plate of flexural rigidity D under the action of a distributed vertical load p is given by:

$$\nabla^4 w = \frac{p}{D} \quad (\text{Eq. A1})$$

The flexural rigidity is defined as $D = \frac{Ed^3}{12(1-\nu^2)}$, with E the Young's modulus, ν the Poisson's ratio and d the elastic thickness of the plate. The load p is given in our problem by the weight of an ice sheet and is defined by $p = \rho gh$, with ρ ice density, g acceleration of gravity and h the thickness of the ice sheet.

Equation A1 is a four-order differential equation where $\nabla^4 = \nabla^2 \nabla^2$, with ∇^2 being the Laplace operator. Given the thin plate approximation and the cylindrical axis-symmetric geometry of our problem, this can be expressed in polar coordinates, for which the Laplace operator can be written as:

$$\nabla^2 = \frac{\partial^2}{\partial r^2} + \frac{1}{r} \frac{\partial}{\partial r} + \frac{1}{r^2} \frac{\partial^2}{\partial \theta^2} \quad (\text{Eq. A2})$$

where r is the radial distance to the axis of cylindrical symmetry and θ is the polar angle. Therefore, Eq. A1 can be then written in polar coordinates as:

$$\nabla^4 w = \left(\frac{\partial^2}{\partial r^2} + \frac{1}{r} \frac{\partial}{\partial r} + \frac{1}{r^2} \frac{\partial^2}{\partial \theta^2} \right) \left(\frac{\partial^2 w}{\partial r^2} + \frac{1}{r} \frac{\partial w}{\partial r} + \frac{1}{r^2} \frac{\partial^2 w}{\partial \theta^2} \right) = \frac{p}{D} \quad (\text{Eq. A3})$$

Assuming a plate loaded and supported symmetrically with respect to the axis of the polar system, the boundary conditions are independent of the angle θ and the deflection w depends only upon the radial

position r . The situation described is the axis-symmetrical bending of the plate. The differential equation of the surface deflection (Eq. A3) is reduced to an ordinary differential equation:

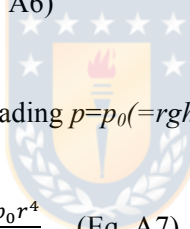
$$\nabla^4 w = \left(\frac{d^2}{dr^2} + \frac{1}{r} \frac{d}{dr} \right) \left(\frac{d^2 w}{dr^2} + \frac{1}{r} \frac{dw}{dr} \right) = \frac{p}{D} \quad (\text{Eq. A4})$$

Then, introducing the identity $\nabla^2 w = \frac{d^2 w}{dr^2} + \frac{1}{r} \frac{dw}{dr} = \frac{1}{r} \frac{d}{dr} \left(r \frac{dw}{dr} \right)$, Eq. A4 appears in the form:

$$\frac{1}{r} \frac{d}{dr} \left\{ r \frac{d}{dr} \left[\frac{1}{r} \frac{d}{dr} \left(r \frac{dw}{dr} \right) \right] \right\} = \frac{p}{D} \quad (\text{Eq. A5})$$

The deflection w is obtained by successive integrations:

$$w = \int \frac{1}{r} \int r \int \frac{1}{r} \int \frac{rp}{D} dr dr dr dr \quad (\text{Eq. A6})$$



If the plate is under a uniform constant loading $p=p_0 (=rgh)$, the general solution of Eq. A6 is:

$$w = c_1 \ln r + c_2 r^2 \ln r + c_3 r^2 + c_4 + \frac{p_0 r^4}{64D} \quad (\text{Eq. A7})$$

where the c 's are constants of integration.

By the other hand, the equations for radial (σ_r) and tangential (σ_t) stress generated by the axisymmetrical deflection w of a thin elastic plate in polar coordinates (Gudmundsson, 1999; Ugural, 1981) are:

$$\sigma_r = - \frac{Ez'}{1-\nu^2} \left(\frac{d^2 w}{dr^2} + \frac{\nu}{r} \frac{dw}{dr} \right) \quad (\text{Eq. A8})$$

$$\sigma_t = - \frac{Ez'}{1-\nu^2} \left(\frac{1}{r} \frac{dw}{dr} + \nu \frac{d^2 w}{dr^2} \right) \quad (\text{Eq. A9})$$

where $z' = \left(\frac{d}{2} - z\right)$ is the normal distance to the mid neutral plane of the plate, and z is the depth (in our coordinate system, z is zero on the surface and increases positively downward).

The terms involving logarithms in Eq. A7 yield an infinite displacement at $r=0$ for all values of c_1 and c_2 except zero. As displacement must be finite at $r=0$, it follows that $c_1 = c_2 = 0$. The other two constants of integration must be derived assuming adequate boundary conditions. Ugural (1981) suggests to consider that the edges of the cylindrical plate at $r=R$ are simply supported under the plate, which translate in the following boundary conditions there:

$$w = 0$$

$$\left(\frac{\partial^2 w}{\partial r^2} + \frac{\nu}{r} \frac{\partial w}{\partial r}\right) = 0 \text{ (the radial moment } M_r \text{ is zero for any angle } \theta\text{)}$$

The above, yield the following respective expressions for the integration constants:

$$c_3 R^2 + c_4 + \frac{p_0 R^4}{64D} = 0 \quad c_3 = -\frac{p_0 R^2}{32D} \frac{3+\nu}{1+\nu}$$



from which $c_4 = \frac{p_0 R^4}{64D} \frac{5+\nu}{1+\nu}$

With $p_0 = \rho g h$, the plate deflection from Eq. A7 is then:

$$w = \frac{\rho g h R^4}{64D} \left(\frac{r^4}{R^4} - 2 \frac{3+\nu}{1+\nu} \frac{r^2}{R^2} + \frac{5+\nu}{1+\nu} \right) \quad (\text{Eq. A10})$$

The maximum deflection, which occurs at $r=0$, is thus:

$$w_{max} = \frac{\rho g h R^4}{64D} \left(\frac{5+\nu}{1+\nu} \right) \quad (\text{Eq. A11})$$

From Eq. (A10), we have obtained the first and second derivatives of w :

$$\frac{dw}{dr} = \frac{\rho g h r}{16D} \left(r^2 - R^2 \frac{r(3+\nu)}{1+\nu} \right) \quad (\text{Eq. A12})$$

$$\frac{d^2w}{dr^2} = \frac{\rho gh}{16D} \left(3r^2 - R^2 \frac{3+\nu}{1+\nu} \right) \quad (\text{Eq. A13})$$

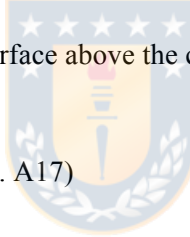
Then, replacing Eqs. (A12) and (A13) in Eqs. (A8) and (A9), the flexural stresses are:

$$\sigma_r = \frac{3\rho gh z'}{4d^3} (3 + \nu)(R^2 - r^2) \quad (\text{Eq. A14})$$

$$\sigma_t = \frac{3\rho gh z'}{4d^3} [(3 + \nu)R^2 - (1 + 3\nu)r^2] \quad (\text{Eq. A15})$$

The stresses under the center of the plate ($r=0$) are:

$$\sigma_r = \sigma_t = R^2(3 + \nu) \frac{3\rho gh z'}{4d^3} \quad (\text{Eq. A16})$$



The maximum stress takes place at the surface above the center of the plate ($r=0, z' = d/2$):

$$\sigma_{r,max} = \sigma_{t,max} = \frac{3(3+\nu)\rho gh}{8} \left(\frac{R}{d} \right)^2 \quad (\text{Eq. A17})$$

We are interested on evaluating pressure P below the center of the plate, which is given by:

$$P = \frac{1}{2}(\sigma_r + \sigma_t) = \sigma_r = \sigma_t = R^2(3 + \nu) \frac{3\rho gh}{4d^3} \left(\frac{d}{2} - z \right) \quad (\text{Eq. A18})$$

ANEXO 2: Flexure and flexural stresses developed in thin elastic-plate of infinite-length on a Winkler foundation and with uniform load on its surface (Appendix B)

Consider a material (e.g. glacial ice) that exerts a load on the surface of a thin elastic plate, deflecting, infills and completely fill the deflected part. The downward acting force (p) is given by: $p = \rho w g$ (ρ : glacial ice density; w : height; g : gravity acceleration). A foundation that acts with a force (f), due to buoyancy of the material displaced, and that is proportional at every point to the deflection is known as a Winkler foundation (Hetényi, 1979). This upward force is given by $f = \rho_m w g$ (ρ_m : foundation density). So, the general equation for the deflection of a thin elastic plate overlying an inviscid substratum is defined by a homogeneous fourth-order differential equation (eq.3.18; Watts, 2001):

$$D \frac{d^4 w}{dx^4} + (f - p) = 0 \quad (\text{Eq.B1})$$

$$D \frac{d^4 w}{dx^4} + (\rho_m - \rho)wg = 0 \quad (\text{Eq.B2})$$



where D is defined as the flexural rigidity of the plate (Watts, 2001; Turcotte & Schubert, 2014) and given by:

$$D = \frac{Ed^3}{12(1-\nu^2)} \quad (\text{Eq.B3})$$

The total flexure w by rectangular distributed or uniform axis-symmetric load on the surface of the plate of infinite length is (eq.3.32; Watts, 2001):

$$w = \frac{p}{2(\rho_m - \rho)g} (2 - e^{-\lambda b} \cos \lambda b - e^{-\lambda a} \cos \lambda a) \quad (\text{Eq.B4})$$

where a and b represent the distance from c (central point, directly beneath the load) to the left and right edge of the load respectively, λ is a parameter that determines the amplitude and wavelength of the deformation (Watts, 2001) and given by:

$$\lambda = \left[\frac{(\rho_m - \rho)g}{4D} \right]^{1/4} \quad (\text{Eq.B5})$$

We can rewrite the total flexure as:

$$w = \frac{p}{2(\rho_m - \rho)g} (2 - e^{-\lambda(R-x)} \cos \lambda(R-x) - e^{-\lambda(R+x)} \cos \lambda(R+x)) \quad (\text{Eq.B6})$$

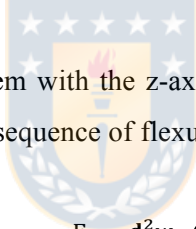
where R is de width of the axis-symmetric load and x the Cartesian coordinate on the x-axis.

The radius of curvature for small slopes approximates to $\frac{d^2w}{dx^2}$ (eq.3.11; Watts 2001):

$$1) \frac{d^2w}{dx^2} = -\frac{p\lambda^2}{(\rho_m - \rho)g} (e^{-\lambda(R-x)} \sin \lambda(R-x) + e^{-\lambda(R+x)} \sin \lambda(R+x)) \quad (\text{Eq.B7})$$

For a point directly beneath the center of the load (x=0):

$$2) \frac{d^2w}{dx^2} = -\frac{p\lambda^2}{(\rho_m - \rho)g} (e^{-\lambda R} \sin \lambda R + e^{-\lambda R} \sin \lambda R) = -\frac{2p\lambda^2}{(\rho_m - \rho)g} (e^{-\lambda R} \sin \lambda R) \quad (\text{Eq.B8})$$



Considering a Cartesian coordinate system with the z-axis positive vertically downward, the flexural stresses that develop in the plate as a consequence of flexure or bending (Watts, 2001; eq.3.27) is:

$$3) \sigma_x = \frac{E}{(1-\nu^2)} \frac{d^2w}{dx^2} y_f \quad \sigma_x = \frac{E}{(1-\nu^2)} \frac{d^2w}{dx^2} \left(\frac{d}{2} - z\right) \quad (\text{Eq.B9})$$

$$4) \sigma_y = \frac{Ev}{(1-\nu^2)} \frac{d^2w}{dx^2} y_f \quad \sigma_y = \frac{Ev}{(1-\nu^2)} \frac{d^2w}{dx^2} \left(\frac{d}{2} - z\right) \quad (\text{Eq.B10})$$

where E is the Young's modulus, v is the Poisson ratio and y_f is the vertical distance on the z-axis and measured from the neutral plane to a point inside of the plate.

From Eq. B8-B10, the flexural stresses directly beneath the center of distributed load therefore it is:

$$5) \sigma_x = -\frac{2Ep\lambda^2 e^{-\lambda R} \sin \lambda R}{(1-\nu^2)(\rho_m - \rho)g} \left(\frac{d}{2} - z\right) \quad (\text{Eq.B11})$$

$$\sigma_x^i(z, t) = -\frac{2E(\rho gh(t))\lambda^2 e^{-\lambda R(t)} \sin(\lambda R(t))}{(1-\nu^2)(\rho_m - \rho)g} \left(\frac{d}{2} - z\right) \quad (\text{Eq.B12})$$

$$6) \quad \sigma_y = -\frac{2Ev\rho\lambda^2 e^{-\lambda R} \sin \lambda R}{(1-\nu^2)(\rho_m - \rho)g} \left(\frac{d}{2} - z\right) \quad (\text{Eq.B13})$$

$$\sigma_y^i(z, t) = -\frac{2Ev(\rho gh(t))\lambda^2 e^{-\lambda R(t)} \sin(\lambda R(t))}{(1-\nu^2)(\rho_m - \rho)g} \left(\frac{d}{2} - z\right) \quad (\text{Eq.B14})$$

Then, the pressure (P^i) inside the plate and directly beneath the center of the load developed by us is:

$$7) \quad P^i(z, t) = \frac{1}{2} \left(\sigma_x^i(z, t) + \sigma_y^i(z, t) \right) \quad (\text{Eq.B15})$$

$$P^i(z, t) = \frac{1}{2} \left(\sigma_x^i(z, t) + \nu \sigma_x^i(z, t) \right) \quad (\text{Eq.B16})$$

$$P^i(z, t) = \frac{\sigma_x^i(z, t)}{2} (1 + \nu) \quad (\text{Eq.B17})$$



$$P^i(z, t) = \frac{E}{2(1-\nu)} \frac{d^2 w}{dx^2} \left(\frac{d}{2} - z\right) \quad (\text{Eq.B18})$$

$$P^i(z, t) = -\frac{Ep(t)\lambda^2 e^{-\lambda R(t)} \sin(\lambda R(t))}{(1-\nu)(\rho_m - \rho)g} \left(\frac{d}{2} - z\right) \quad (\text{Eq.B19})$$

$$P^i(z, t) = -\frac{E(\rho gh(t))\lambda^2 e^{-\lambda R(t)} \sin(\lambda R(t))}{(1-\nu)(\rho_m - \rho)g} \left(\frac{d}{2} - z\right) \quad (\text{Eq.B20})$$

REFERENCIAS

- Albino, F., Pinel, V., & Sigmundsson, F. (2010). Influence of surface load variations on eruption likelihood: application to two Icelandic subglacial volcanoes, Grímsvötn and Katla. *Geophys. J. Int.*, 181, 1510–1524.
- Alidibirov, M., & Dingwell, D. B. (1996). Magma fragmentation by rapid decompression. *Nature*, 380, 146–148. <http://doi.org/10.1038/380146a0>
- Andersen, B., Denton, G., & Lowell, T. (1999). Glacial geomorphologic maps of Llanquihue Drift in the area of the Southern Lake District Chile. *Geografiska Annaler*, 81 A, 155–166.
- Andrew, R. E. B., & Gudmundsson, A. (2007). Distribution, structure, and formation of Holocene lava shields in Iceland. *J. Volcanol. Geotherm. Res.*, 168, 137–154.
- Audet, P., & Bürgmann, R. (2011). Dominant role of tectonic inheritance in supercontinent cycles. *Nature Geoscience*, 4, 184–187.
- Bishop, J. W., Lees, J. M., Biryol, C. B., Mikesell, T. D., & Franco, L. (2017). Examining the Interior of Llaima Volcano with Receiver Functions. *J. Volcanol. Geotherm. Res.*, 352, 1–9.
- Boex, J., Fogwill, C., Harrison, S., Glasser, N. F., Hein, A., Schnabel, C., & Xu, S. (2013). Rapid thinning of the late Pleistocene Patagonian Ice Sheet followed migration of the Southern Westerlies. *Scientific Reports*, 3, 2118. <http://doi.org/10.1038/srep02118>.
- Brown, S. K., Crosweller, H. S., Sparks, R. S. J., Cottrell, E., Deligne, N. I., Guerrero, N. O., Hobbs, L., Kiyosugi, K., Loughlin, S. C., Siebert, L., & Takarada, S. (2014). Characterisation of the Quaternary eruption record: Analysis of the Large Magnitude Explosive Volcanic Eruptions (LaMEVE) database. *J. Appl. Volcanol.*, 3(5), 1–22. <http://doi.org/10.1186/2191-5040-3-5>
- Caldenius, C. (1932). Las Glaciaciones Cuaternarias en la Patagonia y Tierra del Fuego. *Geografiska Annaler*, 14, 1–164.
- Cañón-Tapia, E. (2013). Volcanic eruption triggers: A hierarchical classification. *Earth Sci. Rev.*, 129, 100–119.

Clapperton, C. M., & Clapperton, C. (1993). *Quaternary Geology and Geomorphology of South America*. Elsevier. Retrieved from <https://books.google.cl/books?id=xbYTAQAAIAAJ>

Clapperton, C. M., Sugden, D. E., Kauffman, D., & McCulloch, R. D. (1995). The last glaciation in central Magellan Strait, southernmost Chile. *Quat. Research*, 44, 133–148.

Clapperton, C. (1994). The quaternary glaciation of Chile: a review. *Revista Chilena de Historia Natural*, 67, 369–383.

Clark, P. U., Dyke, A. S., Shakun, J. D., Carlson, A. E., Clark, J., Wohlfarth, B., Mitrovica, J. X., Hostetler, S. W., & McCabe, A. M. (2009). The Last Glacial Maximum. *Science*, 325, 710–714.

Clavero, J., & Moreno, H. (1994). Ignimbritas Licán y Pucón: Evidencias de erupciones explosivas andesítico-basálticas postglaciales del volcán Villarrica, Andes del Sur, 39°25'S. *Actas del VII Congreso Geológico Chileno, Concepción*, 1, 250–254.

Clayton, J., Clapperton, C., & Antinao, J. (1997). Las glaciaciones Pleistocenas en la cuenca del lago Villarrica, Andes del Sur. *Actas del VIII Congreso Geológico Chileno, Antofagasta*, 1, 307–311.

Davidson, J., Turner, S., Handley, H., Macpherson, C., & Dosseto, A. (2007). Amphibole “sponge” in arc crust?. *Geology*, 35(9), 787–790.

de Maisonneuve, C., A., D. M., Bachmann, O., & Burgisser, A. (2012). Insights into shallow magma storage and crystallization at Volcan Llaima (Andean Southern Volcanic Zone, Chile). *J. Volcanol. Geotherm. Res.*, 211, 76–91.

Delgado, F., Pritchard, M. E., Ebmeier, S., González, P., & Lara, L. (2017). Recent unrest (2002-2015) imaged by space geodesy at the highest risk Chilean volcanoes: Villarrica, Llaima, and Calbuco (Southern Andes). *J. Volcanol. Geotherm. Res.*, 344, 270–288.

Delgado, F., Pritchard, M., Lohman, R., & Naranjo, J. A. (2014). The 2011 Hudson volcano eruption (Southern Andes, Chile): pre-eruptive inflation and hotspots observed with InSAR and thermal imagery. *Bull. Volcanol.*, 76(5), 815.

Denton, G. H., Anderson, R. F., Toggweiler, J. R., Edwards, R. L., Schaefer, J. M., & Putnam, A. E. (2010). The last glacial termination. *Science*, 328, 1652–1656.

- Denton, G. H., Heusser, C. J., Lowell, T. V., Moreno, P. I., Andersen, B. G., Heusser, L. E., Schluchter, C., Marchant, D. R. (1999). Interhemispheric linkage of paleoclimate during the last glaciation. *Geografiska Annaler*, 81 A, 107–153.
- Eason, D. E., Sinton, J. M., Grönvold, K., & Kurz, M. D. (2015). Effects of deglaciation on the petrology and eruptive history of the Western Volcanic Zone, Iceland. *Bull. Volcanol.*, 77(6), 47.
- Fogwill, C., Turney, C., Hutchinson, D., Taschetto, A., & England, M. (2015). Obliquity Control On Southern Hemisphere Climate During The Last Glacial. *Scientific Reports*, 5(11673), 1–10.
- Folguera, A., Ramos, V. A., & Vieiro, J. (2003). Tectónica neógena en el extremo sur de la Cordillera Patagónica Septentrional. Cuenca de los lagos la Plata y Fontana (45°S). *Revista de la Asociación Geológica Argentina*, 58(2), 201–208.
- Fontijn, K., Lachowycz, S., Rawson, H., Pyle, D., Mather, T., Naranjo, J., & Moreno-Roa, H. (2014). Late Quaternary tephrostratigraphy of southern Chile and Argentina. *Quat. Sci. Rev.*, 89, 70–84.
- Gardner, J. E., Hilton, M., & Carroll, M. R. (1999). Experimental constraints on degassing of magma: isothermal bubble growth during continuous decompression from high pressure. *Earth Planet. Sci. Lett.*, 168, 201–218.
- Gilbert, D., Freundt, A., Kutterolf, S., & Burkert, C. (2014). Post-glacial time series of explosive eruptions and associated changes in the magma plumbing system of Lonquimay volcano, south central Chile. *International J. Earth Sci.*, 103, 2043–2062.
- Gjermundsen, E. F., Briner, J. P., Akçar, N., Foros, J., Kubik, P. W., Salvigsen, O., & Hormes, A. (2015). Minimal erosion of Arctic alpine topography during late Quaternary glaciation. *Nat. Geosci.*, 8(10), 789–792.
- Glasser, N. F., Jansson, K. N., Harrison, S., & Kleman, J. (2008). The glacial geomorphology and Pleistocene history of South America between 38°S and 56°S. *Quat. Sci. Rev.*, 27, 365–390.
- Gudmundsson, A. (1999). Postglacial crustal doming, stresses and fracture formation with application to Norway. *Tectonophysics*, 307, 407–419.

Gudmundsson, A. (2012). Strengths and strain energies of volcanic edifices: implications for eruptions, collapse calderas, and landslides. *Nat. Hazards Earth Syst. Sci.*, 12, 2241–2258.

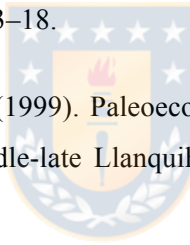
Gudmundsson, A. (2006). How local stress control magma-chamber ruptures, dyke injections, and eruptions in composite volcanoes. *Earth Sci. Rev.*, 79, 1–36.

Hampel, A. (2017). Response of faults to climate induced changes of ice sheets, glaciers and lakes. *Geology Today*, 33(1), 12–18.

Hardarson, B. S., & Fitton, J. G. (1991). Increased mantle melting beneath Snaefellsjökull volcano during Late Pleistocene deglaciation. *Nature*, 353(6339), 62.

Heusser C., F. R. (1977). Quaternary glaciations and environments of northern Isla Chiloé, Chile. *Geology*, 5, 305–308.

Heusser, C. (1990). Chilotan piedmont glacier in the southern andes during the last glacial maximum. *Revista Geológica de Chile*, 17(1), 3–18.



Heusser, C., Heusser, L., & Lowell, T. (1999). Paleoecology of the southern Chilean Lake District - Isla Grande de Chiloe during middle-late Llanquihue glaciation and deglaciation. *Geografiska Annaler*, 81 A, 231–284.

Hickey-Vargas, R., López-Escobar, L., Moreno, H., Clavero, J., Lara, L., & Sun, M. (2004). Magmatic evolution of the Villarrica Volcano. In Villarrica Volcano (39.5°S), Southern Andes, Chile (L. Lara & J. Clavero; editors). *Servicio Nacional de Geología y Minería, Boletín* 61, 39–45.

Hollin, J., & Schilling, D. (1981). Late Wisconsin-Weichselian Mountain Glaciers and Small Ice Caps. In The Last Great Ice Sheets (G. Denton & T. J. Hughes; editors). New York: John Wiley & Sons, 179–198.

Hooper, A., Ofeigsson, B., Sigmundsson, F., Lund, B., Einarsson, P., Geirsson, H., & Sturkell, E. (2011). Increased capture of magma in the crust promoted by ice-cap retreat in Iceland. *Nature Geosci.*, 4(11), 783–786. Retrieved from <http://dx.doi.org/10.1038/ngeo1269>

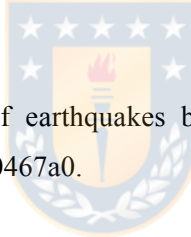
Hubbard, A., Hein, A., Kaplan, M., Hulton, N., & Glasser, N. (2005). A modeling reconstruction of the last glacial maximum ice sheet and its deglaciation in the vicinity of the northern Patagonian icefield, South America. *Geografiska Annaler*, 87 A, 375–391.

Hulton, N., Purves, R., McCulloch, R., Sugnde, D., & Bentley, M. (2002). The Last Glacial Maximum and deglaciation in southern South America. *Quat. Sci. Rev.*, 21, 233–241.

Huybers, P., & Langmuir, C. (2009). Feedback between deglaciation, volcanism, and atmospheric CO₂. *Earth Planet. Sci. Lett.*, 286, 479–491.

Ivins, E. R., & James, T. S. (1999). Simple models for late Holocene and present-day Patagonian glacier fluctuations and predictions of a geodetically detectable isostatic response. *Geophys. J. Int.*, 138(3), 601–624.

Jellinek, A. M., Manga, M., & Saar, M. O. (2004). Did melting glaciers cause volcanic eruptions in eastern California? Probing the mechanics of dike formation. *J. Geophys. Res.*, 109(B09206), 1–10.



Johnston, A. C. (1987). Suppression of earthquakes by large continental icesheets. *Nature*, 330, 467–469. <http://doi.org/10.1038/330467a0>.

Jull, M., & McKenzie, D. (1996). Effect of deglaciation on mantle melting beneath Iceland. *J. Geophys. Res.*, 101(B10), 21815–21828. <http://doi.org/10.1029/96JB01308>

Kaplan, M. R., Ackert, R. P., Singer, B. S., Douglass, D. C., & Kurz, M. D. (2004). Cosmogenic Nuclide Chronology of Millennial-Scale Glacial Advances During O-isotope Stage 2 in Patagonia. *Geol. Soc. Amer. Bull.*, 116, 308–321.

Kratzmann, D. J., Carey, S., Scasso, R. A., & Naranjo, J. A. (2009). Compositional variations and magma mixing in the 1991 eruptions of Hudson volcano, Chile. *Bull. Volcanol.*, 71(4), 419–439.

Kratzmann, D. J., Carey, S., Scasso, R. A., & Naranjo, J. A. (2010). Role of cryptic amphibole crystallization in magma differentiation at Hudson volcano, Southern Volcanic Zone, Chile. *Contrib. Mineral. Petrol.*, 159, 237–264.

Kutterolf, S., Jegen, M., Mitrovica, J., Kwasnitschka, T., Freundt, A., & Huybers, P. (2013). A detection of Milankovitch frequencies in global volcanic activity. *Geology*, 41(2), 227–230.

Lange, H., Casassa, G., Ivins, E. R., Schröder, L., Fritsche, M., Richter, A. J., Groh, A., & Dietrich, R. (2014). Observed crustal uplift near the Southern Patagonian Icefield constrains improved viscoelastic Earth models. *Geophys. Res. Lett.*, 41(Issue 3), 1–8. <http://doi.org/10.1002/2013GL058419>

Laugénie, C. (1982). *La Region Des Lacs, Chili Meridional. Recherches Sur L'évolution Geomorphologique D'un Piémont Glaciaire Quaternaire Andin*. These De Doctorant D'etat Presentee Devant L'Universite De Bordeaux III.

Laugénie, C. (1971). Elementos de la Cronología Glaciar de los Andes Chilenos Meridionales. *Cuadernos Geográficos del Sur*, 1, 7–20.

Lohmar, S. (2008). *Petrología de las ignimbritas Licán y Pucón (Volcán Villarrica) y Curacuatín (Volcán Llaima) en los Andes del Sur de Chile*. Universidad de Chile, en cotutela con la Universidad Blaise Pascal-Clermont-Ferrand II.

Lohmar, S., Parada, M., Gutiérrez, F., Robin, C., & Gerbe, M. (2012). Mineralogical and numerical approaches to establish the pre-eruptive conditions of the mafic Licán Ignimbrite, Villarrica Volcano (Chilean Southern Andes). *J. Volcanol. Geotherm. Res.*, 235–236, 55–69.

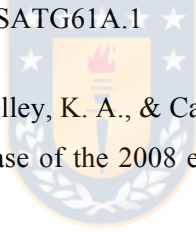
Lohmar, S., Robin, C., Gourgaud, A., Clavero, J., Parada, M. A., Moreno, H., & Ersoy, O. (2007). Evidence of magma-water interaction during the 13.800 years BP explosive cycle of the Licán Ignimbrite, Villarrica volcano (southern Chile). *Revista Geológica de Chile*, 34(2), 233–247.

López-Escobar, L., Cembrano, J., & Moreno, H. (1995). Geochemistry and tectonics of the Chilean Southern Andes basaltic Quaternary volcanism (37–46°S). *Revista Geológica de Chile*, 22(2), 219–234.

Lowell, T. V, Heusser, C. J., Andersen, B. G., Moreno, P. I., Hauser, A., Heusser, L. E., Schlüchter, C., Marchant, D. R., & Denton, G. H. (1995). Interhemispheric correlation of Late Pleistocene glacial events. *Science*, 269, 1541–1549.

- Lumley, S. H., & Switsur, R. (1993). Late Quaternary chronology of the Taitao Peninsula, southern Chile. *J. Quat. Sci.*, 8, 161–165.
- MacLennan, J., Jull, M., McKenzie, D., Slater, L., & Grönvold, K. (2002). The link between volcanism and deglaciation in Iceland. *Geochem. Geophys. Geosyst.*, 3(11), 1–25.
- Manga, M., & Brodsky, E. (2006). Seismic Triggering of Eruptions in the Far Field: Volcanoes and Geysers. *Annu. Rev. Earth Planet. Sci.*, 24, 263–291.
- Mangan, M., & Sisson, T. (2000). Delayed, disequilibrium degassing in rhyolite magma: Decompression experiments and implications for explosive volcanism. *Earth Planet. Sci. Lett.*, 183(3–4), 441–455. [http://doi.org/10.1016/S0012-821X\(00\)00299-5](http://doi.org/10.1016/S0012-821X(00)00299-5)
- Mauk, F. J., & Johnston, M. J. S. (1973). On the Triggering of Volcanic Eruptions by Earth Tides. *J. Geophys. Res.*, 78(17), 3356–3362.
- McCulloch, R. D., & Bentley, M. J. (1998). Late glacial ice advances in the Strait of Magellan, southern Chile. *Quat. Sci. Rev.*, 17, 775–787.
- McCulloch, R. D., Bentley, M. J., Purves, R. S., Hulton, N. R. J., Sugden, D. E., & Clapperton, C. M. (2000). Climatic inferences from glacial and palaeoecological evidence at the last glacial termination, southern South America. *J. Quat. Sci.*, 15(4), 409–417.
- McGuire, B. (2010). Potential for a hazardous geospheric response to projected future climate changes. *Phil. Trans. R. Soc. A*, 368, 2317–2345. <http://doi.org/10.1098/rsta.2010.0080>
- Mercer, J. (1983). Cenozoic Glaciation in the Southern Hemisphere. *Annu. Rev. Earth Planet. Sci.*, 11, 99–132.
- Miranda, C. G., Moreno, P. I., Vilanova, I., & Villa-Martinez, R. P. (2013). Glacial fluctuations in the Coyhaique-Balmaceda sector of central Patagonia (45–46°S) during the last glacial termination. *Boll. Geofis. Teor. Appl.*, 54(Supplement 2), 268–271.
- Moore, G., Vennemann, T., & Carmichael, I. S. E. (1998). An empirical model for the solubility of H₂O in magmas to 3 kilobars. *American Mineralogist*, 1–2, 36–42.

- Mora, D., & Tassara, A. (2019). Upper crustal decompression due to deglaciation-induced flexural unbending and its role on postglacial volcanism at the Southern Andes. *Geophys. J. Int.*, 216, 1549–1559, <https://doi.org/10.1093/gji/ggy473>
- Moreno, H., & Clavero, J. (2006). Geología del área del Volcán Villarrica, Carta Geológica de Chile, Serie Geología Básica, Escala 1:50.000.
- Pagli, C., & Sigmundsson, F. (2008). Will present day glacier retreat increase volcanic activity? Stress induced by recent glacier retreat and its effect on magmatism at the Vatnajökull ice cap, Iceland. *Geophysical Research Letters*, 35(9), L09304. <http://doi.org/10.1029/2008GL033510>
- Peltier, W. (2004). Global glacial isostasy and the surface of the ice-age earth: the ice-5g (vm2) model and grace. *Annu. Rev. Earth Planet. Sci.*, 32, 111–149.
- Pérez-Gussinyé, M., Lowry, A. R., Phipps Morgan, J., & Tassara, A. (2008). Effective elastic thickness variations along the Andean margin and their relationship to subduction geometry. *Geochem. Geophys. Geosyst.*, 9(Q02003). <http://doi.org/10.1029/2007GC001786>
- Pinel, V., Sigmundsson, F., Sturkell, E., Geirsson, H., Einarsson, P., Gudmundsson, M. & Högnadóttir, T. (2007). Discriminating volcano deformation due to magma movements and variable surface loads: application to Katla subglacial volcano, Iceland. *Geophys. J. Int.*, 169, 325–338.
- Pinel, V., Albino, F., Sigmundsson, F., Sturkell, E., Geirsson, H., Einarsson, P., & Gudmundsson, M. T. (2009). Consequences of local surface load variations for volcano monitoring: Application to Katla subglacial volcano, Iceland. In *The VOLUME Project, Volcanoes: Understanding subsurface mass movement* (pp. 25–39). Jaycee. Retrieved from www.volume-project.net
- Pinel, V., & Jaupart, C. (2003). Magma chamber behavior beneath a volcanic edifice. *J. Geophys. Res.*, 108(B2), ECV 4 1-17. <http://doi.org/10.1029/2002JB001751>
- Pritchard, M. E., Jay, J. A., Aron, F., Henderson, S. T., & Lara, L. E. (2013). Subsidence at southern Andes volcanoes induced by the 2010 Maule, Chile earthquake. *Nature Geoscience*, 6, 632–636. <http://doi.org/10.1038/ngeo1855>

- Rabassa, J., Coronato, A. M., & Salemme, M. (2005). Chronology of the Late Cenozoic Patagonian glaciations and their correlation with biostratigraphic units of the Pampean region (Argentina). *J. South Am. Earth Sci.*, 20, 81–103.
- Rawson, H., Naranjo, J., Smith, V., Fontijn, K., Pyle, D., Mather, T., & Moreno, H. (2015). The frequency and magnitude of post-glacial explosive eruptions at Volcán Mocho-Choshuenco, southern Chile. *J. Volcanol. Geotherm. Res.*, 299, 103–129.
- Rawson, H., Pyle, D., Mather, T., Smith, V., Fontijn, K., Lachowycz, S., & Naranjo, J. (2016). The magmatic and eruptive response of arc volcanoes to deglaciation: Insights from southern Chile. *Geology*, 44(4). <http://doi.org/10.1130/G37504.1>
- Rubin, A. M. (1995). Propagation of magma-filled cracks. *Annu. Rev. Earth Planet. Sci.*, 23, 287–336. <http://doi.org/10.1146/annurev.ea.23.050195.001443>
- Russo, R. M., VanDecar, J. C., Comte, D., Mocanu, V. I., Gallego, A., & Murdie, R. E. (2010). *GSA Today*, 20(9), 4–10, doi: 10.1130/GSATG61A.1
- 
- Ruth, D. C., Cottrell, E., Cortés, J. A., Kelley, K. A., & Calder, E. S. (2016). From passive degassing to violent strombolian eruption: the case of the 2008 eruption of Llaima volcano, Chile. *J. Petrol.*, 57(9), 1833–1864.
- Sammis, C. G., & Julian, B. R. (1987). Fracture instabilities accompanying dike intrusion. *J. Geophys. Res.*, 92, 2597–2605.
- Schindlbeck, J. C., Freundt, A., & Kutterolf, S. (2014). Major changes in the post-glacial evolution of magmatic compositions and pre-eruptive conditions of Llaima Volcano, Andean Southern Volcanic Zone, Chile. *Bull. Volcanol.*, 76, 830–851. <http://doi.org/10.1007/s00445-014-0830-x>
- Schmidt, P., Lund, B., Hieronymus, C., MacLennan, J., Árnadóttir, T., & Pagli, C. (2013). Effects of present day deglaciation in Iceland on mantle melt production rates. *J. Geophys. Res.: Solid Earth*, 118, 3366–3379. <http://doi.org/10.1002/jgrb.50273>.
- Sigmundsson, F. (2006). *Iceland Geodynamics Crustal Deformation and Divergent Plate Tectonics*. New York: Springer.

Sigmundsson, F., Albino, F., Schmidt, P., Lund, B., Pinel, V., Hooper, A., & Pagli, C. (2013). Multiple Effects of Ice Load Changes and Associated Stress Change on Magmatic Systems. In B. McGuire & M. Maslin (Eds.), *Climate Forcing of Geological Hazards*. Chichester, UK.: John Wiley & Sons Ltd. <http://doi.org/10.1002/9781118482698.ch5>

Sigmundsson, F., Pinel, V., Lund, B., Albino, F., Pagli, C., Geirsson, H., & Sturkell, E. (2010). Climate effects on volcanism: influence on magmatic systems of loading and unloading from ice mass variations, with examples from Iceland. *Philosophical Transactions of the Royal Society A: Mathematical, Physical and Engineering Sciences*, 368(1919), 2519 LP-2534. Retrieved from <http://rsta.royalsocietypublishing.org/content/368/1919/2519.abstract>

Sigvaldasson, G. E., Annertz, K., & Nielsson, M. (1992). Effect of glacier loading/delowering on volcanism: Postglacial volcanic production rate of the Dyngjufjöll area, central Iceland. *Bull. Volcanol.*, 54, 385–392.

Singer, B. S., Jicha, B. R., Harper, M. A., Naranjo, J. A., Lara, L. E., & Moreno-Roa, H. (2008). Eruptive history, geochronology, and magmatic evolution of the Puyehue-Cordón Caulle volcanic complex, Chile. *Geol. Soc. Amer. Bull.*, 120, 599–618. <http://doi.org/10.1130/B26276.1>

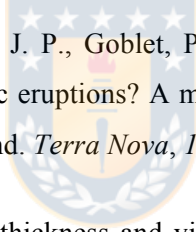
Singer, B., Ackert, R., & Guillou, H. (2004). $^{40}\text{Ar}/^{39}\text{Ar}$ and K--Ar Chronology of Pleistocene Glaciations in Patagonia. *Geol. Soc. Amer. Bull.*, 116, 434–450.

Sternai, P., Caricchi, L., Castelltort, S., & Champagnac, J. D. (2016). Deglaciation and glacial erosion: A joint control on magma productivity by continental unloading. *Geophysical Research Letters*, 43(4), 1632–1641. <http://doi.org/10.1002/2015GL067285>

Sugden, D., Hulton, N., & Purves, R. (2002). Modelling the inception of the Patagonian icesheet. *Quat. International*, 95–96, 55–64.

Sulpizio, R., Costa, A., & Wadge, G. (Eds.). (2017). *Stress Field Control of Eruption Dynamics. Front. Earth Sci.* Lausanne: Frontiers Media. <http://doi.org/10.3389/978-2-88945-277-4>

Tait, S., Jaupart, C., & Vergniolle, S. (1989). Pressure, gas and eruption periodicity of a shallow, crystallising magma chamber. *Earth Planet. Sci. Lett.*, 92, 107–123. [http://doi.org/10.1016/0012-821X\(89\)90025-3](http://doi.org/10.1016/0012-821X(89)90025-3)

- Tassara, A., Swain, C., Hackney, R., & Kirby, J. (2007). Elastic thickness structure of South America estimated using wavelets and satellite-derived gravity data. *Earth Planet. Sci. Lett.*, 253, 17–36.
- Thomson, S. N., Brandon, M. T., Tomkin, J. H., Reiners, P. W., Vásquez, C., & Wilson, N. J. (2010). Glaciation as a destructive and constructive control on mountain building. *Nature*, 467(7313), 313–317.
- Tuffen, H. (2010). How will melting of ice affect volcanic hazards in the twenty-first century? *Phil. Trans. R. Soc. A*, 368, 2535–2558. <http://doi.org/10.1098/rsta.2010.0063>
- Turcotte, D., & Schubert, G. (2014). *Geodynamics* (third). Cambridge: Cambridge University Press.
- Ugural, A. C. (1981). *Stresses in Plates and Shells*. New York: McGraw-Hill.
- Villagrán, C. (1988). Late Quaternary vegetation of southern Isla Grande de Chiloé, Chile. *Quat. Research*, 29, 294–306.
- Violette, S., de Marsily, G., Carbonnel, J. P., Goblet, P., Ledoux, E., Tijani, S. M., & Vouille, G. (2001). Can rainfall trigger volcanic eruptions? A mechanical stress model of an active volcano: Piton de la Fournaise, Reunion Island. *Terra Nova*, 13, 18–24.
- Walcott, R. I. (1970). Flexural rigidity, thickness and viscosity of the lithosphere. *J. Geophys. Res.*, 75(20), 3941–3954.
- Watt, S., Pyle, D., & Mather, T. (2013). The volcanic response to deglaciation: Evidence from glaciated arcs and a reassessment of global eruption records. *Earth Sci. Rev.*, 122, 77–102.
- Watts, A. B. (2001). *Isostasy and Flexure of the Lithosphere*. Cambridge University Press.
- Weller, D., Miranda, C., Moreno, P., Villa-Martínez, R., & Stern, C. (2014). The large late-glacial Ho eruption of the Hudson volcano, southern Chile. *Bull. Volcanol.*, 76(831), 1–18. <http://doi.org/10.1007/s00445-014-0831-9>